AD-A127 590 INTERFACE CHARACTER OF ALUMINUM-GRAPHITE METAL MATRIX COMPOSITES(U) TEXAS UNIV AT AUSTIN MATERIALS SCIENCE AND ENGINEERING H L MARCUS 27 JAN 83 UTMSE-83-1 1/2

UNCLASSIFIED N00014-78-C-0094 F/G 11/4 NL

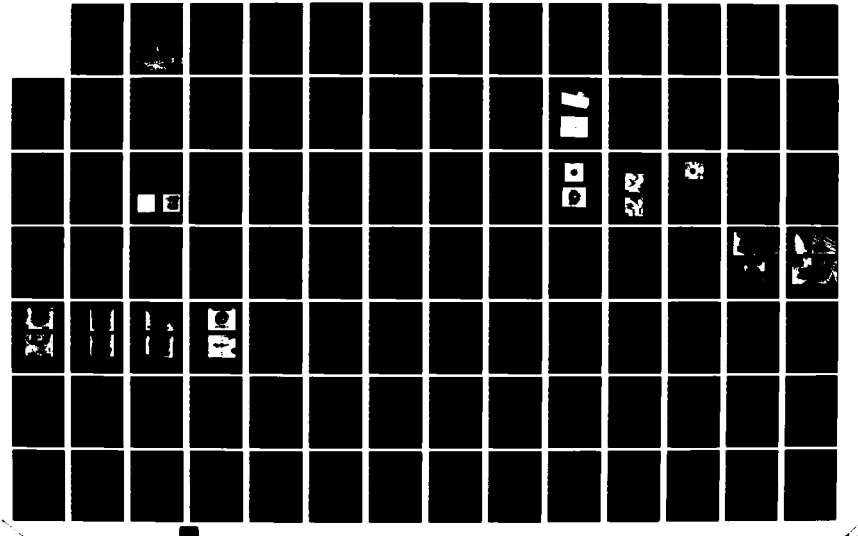

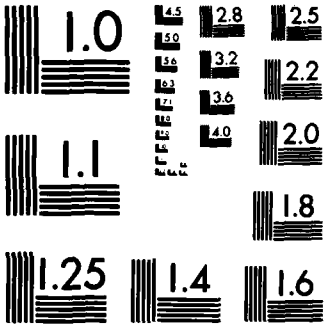

MICROCOPY RESOLUTION TEST CHART
NATIONAL BUREAU OF STANDARDS-1963-A

Materials Science and Engineering

The University of Texas at Austin

INTERFACE CHARACTER OF ALUMINUM-GRAPHITE METAL MATRIX COMPOSITES

UTMSE-83-1
Final Technical Report
January 27, 1983

Office of Naval Research
Contract N00014-78-C-0094

PRINCIPAL INVESTIGATOR: HARRIS L. MARCUS

Mechanical Engineering/Materials Science and Engineering

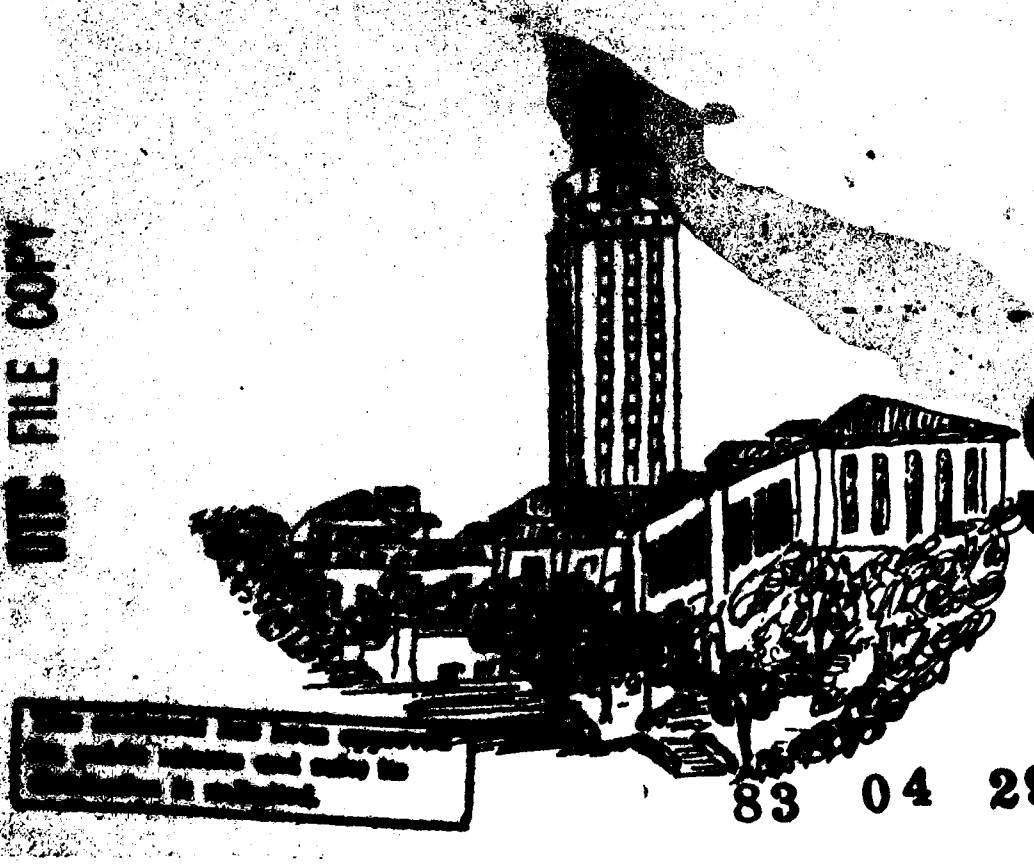

83 04 29 018

SECURITY CLASSIFICATION OF THIS PAGE (When Data Entered)

REPORT DOCUMENTATION PAGE	READ INSTRUCTIONS BEFORE COMPLETING FORM
1. REPORT NUMBER: UTMSE-83-1	2. GOVT ACCESSION NO.: AD-A127590
	3. RECIPIENT'S CATALOG NUMBER:
4. TITLE (and Subtitle): Interface Character of Aluminum-Graphite Metal Matrix Composites	5. TYPE OF REPORT & PERIOD COVERED: Final Technical Report Dec 1 1977 - Nov 30 1982
	6. PERFORMING ORG. REPORT NUMBER: UTMSE-83-1
7. AUTHOR(s): H.L. Marcus	8. CONTRACT OR GRANT NUMBER(s): N00014-78-C-0094
9. PERFORMING ORGANIZATION NAME AND ADDRESS: The University of Texas, Mechanical Engineering/Materials Science, TAY 167, Austin, TX 78712	10. PROGRAM ELEMENT, PROJECT, TASK AREA & WORK UNIT NUMBERS:
11. CONTROLLING OFFICE NAME AND ADDRESS: Office of Naval Research, Metallurgy and Ceramics Program, Arlington, VA 22217	12. REPORT DATE: January 27, 1983
	13. NUMBER OF PAGES:
14. MONITORING AGENCY NAME & ADDRESS (if different from Controlling Office): Dr. B.A. MacDonald, Metallurgy Division, Office of Naval Research, Code 471, Department of the Navy, Arlington, VA 22217	15. SECURITY CLASS. (of this report): Unclassified
	15a. DECLASSIFICATION/DOWNGRADING SCHEDULE:

16. DISTRIBUTION STATEMENT (of this Report)

Approved for public release; Distribution unlimited.

17. DISTRIBUTION STATEMENT (of the abstract entered in Block 20, if different from Report)

18. SUPPLEMENTARY NOTES

19. KEY WORDS (Continue on reverse side if necessary and identify by block number)

Metal Matrix Composites, Aluminum/Graphite Composites, Auger Electron Spectroscopy, Residual Stresses, Interface Characteristics, Electron Loss Spectroscopy, Transverse Strength, Transmission Electron Spectroscopy, Carbon Diffusion, Scanning Auger Microscopy, I/V Switching, Aluminum Carbide, Aluminum/Silicon Carbide Discontinuous Fibers

20. ABSTRACT (Continue on reverse side if necessary and identify by block number)

The results of the research on aluminum/graphite interfaces described in this final report can be summarized in terms of the experimental approaches used to probe the metal matrix interfaces. The materials studied included the commercial Al/graphite composites; layered model systems on single crystal and polycrystalline graphite substrates as well as glassy carbon substrates; and discontinuous fiber SiC/Al composites. The I/V characterization of the interface demonstrated that the oxide within the interface plays a major role in the interface strength. If the interface was in a low conductivity state, peel test (cont)

DD FORM 1 JAN 73 1473 EDITION OF 1 NOV 65 IS OBSOLETE

20. continued

fractures occurred at the interface, weaving through the oxide. When the interface was switched into an electrically conductive state peel test fractures occurred within the single crystal graphite substrate. The interface strength was directly correlatable with its conductivity state in the Al-γ-Al_2O_3-(0001) graphite model system. The commercial material measurements were indecisive.

TEM of the commercial materials and the model laminates showed the presence of γ-Al_2O_3, $MgAl_2O_3$ and TiB_2 in the as-prepared samples. No aluminum carbide was found. The presence of the oxide seemed to be required to get some transverse strength. When samples were aged within the solid state region, Al_4C_3 and Al_4C_4O were found. Their growth was strongly dependent on the heat treat environment, the temperature, and the crystallography of the graphite relative to the interface. Basal plane orientation of the graphite prevented any carbide formation unless an external hydrocarbon containing environment was present during the heat treatment. When carbides were formed the transverse strength increased but the longitudinal strength was dramatically reduced.

AES was used to characterize the fracture surface chemistry. Inert ion sputtering profiles confirmed the presence of the oxide adjacent to the graphite, the TiB_2 displaced toward the matrix. AES after heat treatment of the commercial composites showed the carbon diffused through the oxide to form the carbide. This was not consistently observed in the model systems.

A series of AES related experiments were performed relative to oxide formation, diffusion in an oxide, preferential sputtering and artifacts on carbide peak analysis due to electron and ion beam damage.

X-ray measurements of the residual stress of the commercial composites shows tensile stresses some of which were greater than the yield strength of the aluminum matrix. Liquid nitrogen quenching greatly reduced the stresses with minimal influence on the transverse fracture strength. The results support the conclusion that the residual stresses do not control the transverse strength.

The fracture study of discontinuous fiber SiC/aluminum composites showed indications of a strong interface. AES measurements show the fracture path was remote from the interface. TEM showed the presence of β-Al_4SiC_4 at some interfaces, but a lack of phases at other interfaces.

TABLE OF CONTENTS

Table of Contents Continued

I. Introduction

The research results in this final report represent the overall results associated with the study aimed at determining the nature of the interface between the aluminum matrix and the graphite fibers in the aluminum graphite metal matrix composites (MMC). A limited effort on the aluminum/silicon carbide discontinuous fiber composites is also reported. This report extends and consolidates the efforts previously reported.[1-3] The major emphasis will be on summarizing the results during the contract period with some emphasis on the results from the past year. The results reported here are from experiments and analyses performed by SweDen Tsai, Duane Finello, James Lo, Li-Jiuan Fu, Horacio Mendez and Dr. Michael Schmerling. The Al/Graphite MMC wire and plate materials used in the studies came from the Aerospace Corporation and the aluminum/silicon carbide discontinuous fiber composites from the Silag Division of Exxon (Arco). The model laminate systems were produced in our laboratories.

II. Experimental Approaches and Results

During the course of this research the main emphasis in the interface studies of the aluminum graphite metal matrix composites has been focused on five areas. These are: 1) Studying the interface by determining the characteristic I/V curves measured across the interface and relating this to the fracture path; 2) Scanning Auger Microscopy (SAM) of the fracture path to determine the chemistry of the fracture path; 3) Transmission electron microscopy (TEM) of the phases present at the interface of model and commercial composites;

4) Kinetics of Al_4C_3 formation as a function of graphite form and interface phases; and 5) X-ray determination of residual stresses in the composite. Limited SAM and TEM studies were done on the aluminum/silicon carbide discontinuous fiber composites. The results will be summarized in the following sections. The details of the results are presented in the appropriate appendices, most of which are preprints or reprints of results published during the course of this contract.

A. Current Voltage (I/V) and AES Characterization of the Interface

The initial interface studies on the aluminum-graphite composites had shown that an oxide existed at the interface[4] that seemed to influence the transverse strength of the composite. A more detailed discussion on the oxide will be made in the sections on SAM and TEM of the composites. To simulate the interface, a model system was constructed in which aluminum oxide and aluminum metal layers were successively deposited on a planar graphite single crystal.

In order to determine the fracture behavior of the interface regions of the model system, peel tests were conducted. These tests were made on samples with different oxide thicknesses. The results of the peel test indicate that the oxide sandwiched between the aluminum and graphite has an important influence on the interface bonding strength. That is, when the oxide is thin, 5-10 nm, the interface is more cohesive than it is for the thicker oxide, 15-20 nm.

Electrical characteristics of the interface were also investigated by measuring the voltage-current, I/V, response across the interface as shown in detail in Appendix A.

It was observed that the interface exhibits a switching behavior with a thick oxide, about 20.0 nm. The sample switched from a low conductive state to a high conductive state at a threshold voltage of about 2.0 v. The samples with thin oxide showed little or no switching, but were in the high conductive state.

In an effort to understand the relation between switching and the cohesiveness of the interface, peel tests were conducted on the thicker oxide samples in the low and high conductive states as well as in the low state after relaxing back from the high conductive state. This test revealed that the fracture path changed from within the oxide interface between the graphite and the aluminum metal to within the graphite crystal by switching from a low conductive state to a high conductive state and back to the interface on relaxing back to the low conductive state. The results clearly demonstrate that the conductivity of the interface is involved in the mechanical strength of the interface. The details of the experiments are given in Appendix A.

In an attempt to see if the I/V characterization could be extended to the actual composite, the current versus voltage characteristics were studied in two composite systems: VSB-32/6061 and VSB-32/oxide/6061 Gr/Al composite wire. The results of these experiments suggest that a fixed high conductive state is present since no obvious switching was observed. However, as pointed out in Appendix B, improvements of the experimental techniques are necessary to eliminate short-circuit current paths which may cause the high conductance state. Such improvements may show that the

commercial Al/Gr composites can be switched from low to high conducting state. The characteristics of the switching could possibly then be used to evaluate the strength of the interface.

B. AES Studies of the Aluminum-Graphite Interface

To study the influence of the oxide layer on the fracture process of the Gr/Al composites, detailed AES analysis of the fracture interfaces was performed. Along the interfacial fracture surface, fiber sites can be readily distinguished from matrix sites where the fiber has been pulled away. A representative Auger spectrum taken from a typical fiber site of a PAN precursor Gr/Al composite fractured in situ is shown in Fig. 1.

Recently, the lower cost high modulus pitch precursor Gr/Al composites have almost completely replaced the PAN type Gr/Al in commercial applications. To test the general validity of the relationship between transverse strength and fiber-to-oxide adherency, AES in situ fracture analysis of VSB-32/6061 and VSB-32/oxide/6061 pitch type Gr/Al composites was performed. Analogous results were obtained (see Figs. 2 and 3) and correlated with the mechanical tests. The material of lower transverse strength (VSB-32/6061) exhibited considerably less fiber-to-oxide adherency than did the material of higher transverse strength (VSB-32/oxide/6061) due to different processing steps taken during manufacture. The VSB-32/oxide/6061 material was distinguished by more extensive oxide film coverage prevalent over most of the newly created fiber surface area resulting from transverse fracture.

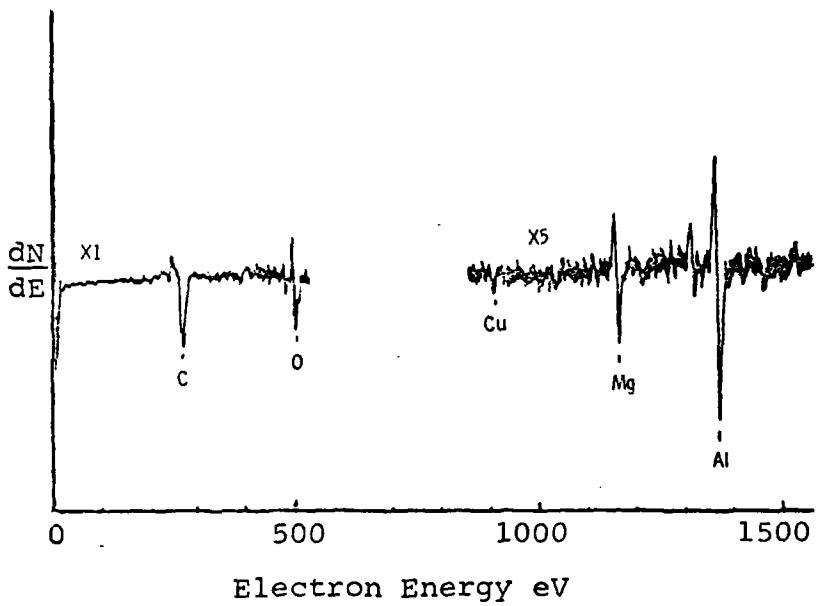

Fig. 1. High spatial resolution Auger spectrum for fiber surface of PAN type Gr/Al composite fractured in situ.

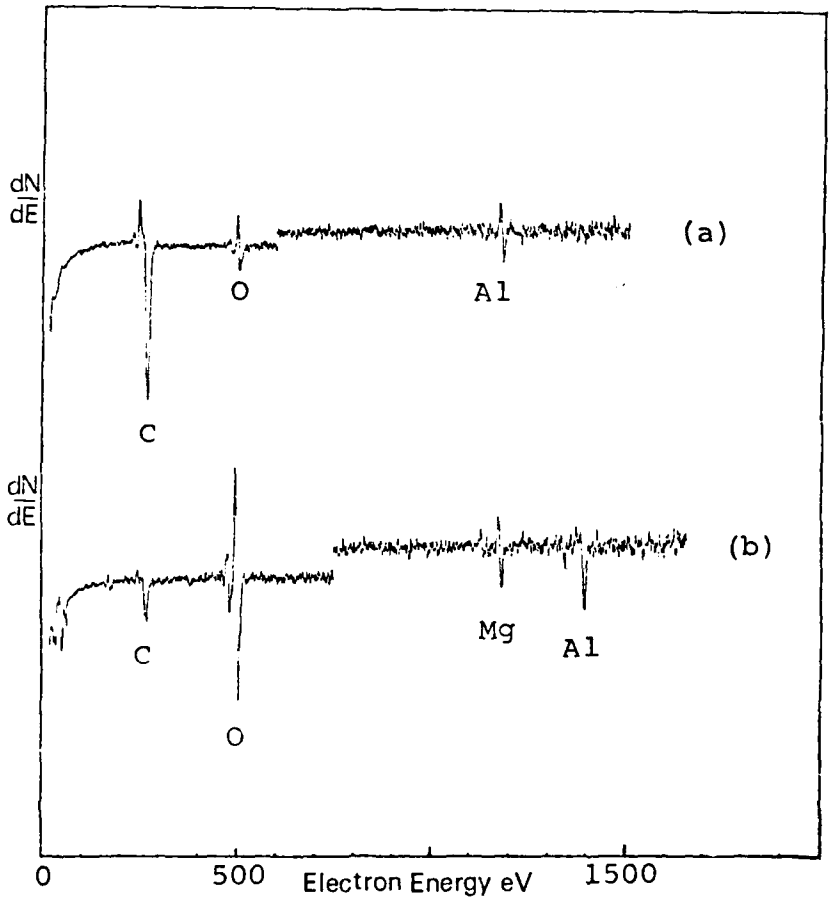

Fig. 2. High spatial resolution Auger spectra for fiber surfaces of (a) VSB-32/6061 and (b) VSB-32/oxide/ 6061 pitch type Gr/Al composites fractured in situ.

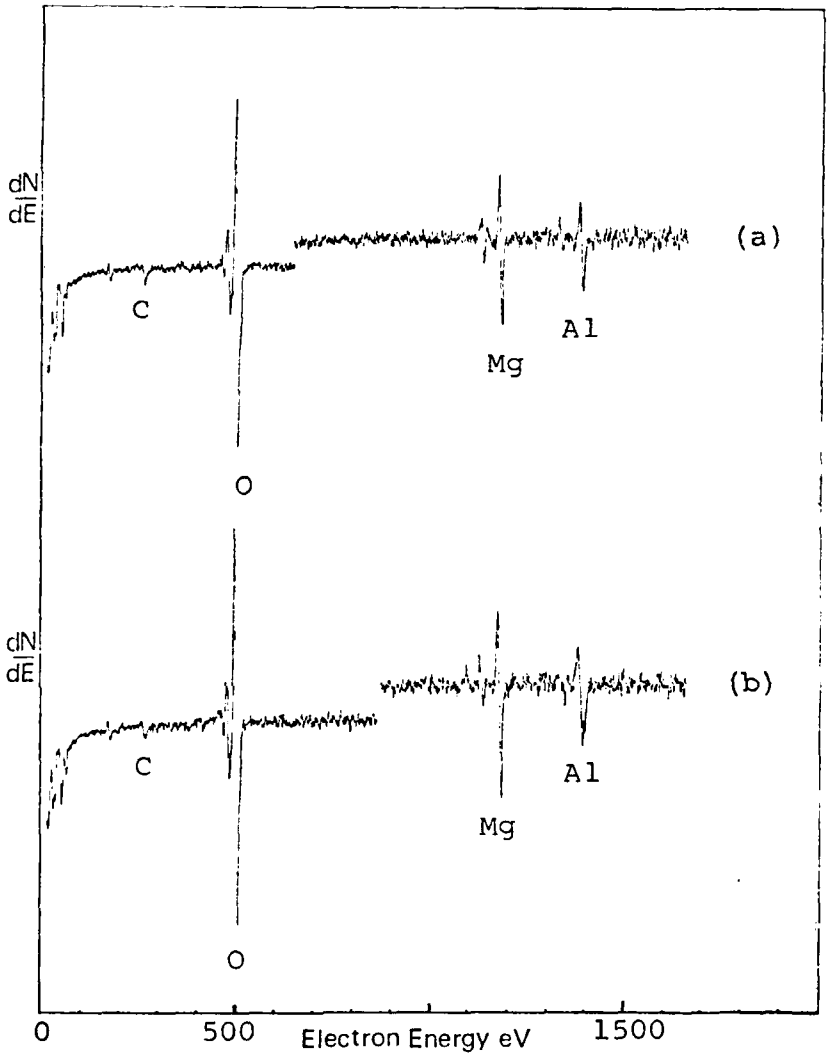

Fig. 3. High spatial resolution Auger spectra for matrix surfaces of (a) VSB-32/6061 and (b) VSB-32/oxide/6061 pitch type Gr/Al composites fractured in situ.

The interfacial oxide thickness within Gr/Al composite material plays a role in the fracture process. Although it is somewhat questionable where the oxide ends and the displaced TiB_2 wetting layer begins, it is possible to compare scaled high spatial resolution AES sputtering profiles (see Figs. 4 and 5). The VSB-32/oxide/6061 material has the greater interfacial oxide thickness. The VSB-32/6061 material has approximately a five nanometer interfacial oxide thickness, while that of the VSB-32/oxide/6061 material is approximately three times as thick. It should be understood that these are mixed oxides which are characteristically of greater conductivity than the pure γ-Al_2O_3 present in the basic substrate/adsorbate thin layer composites to be discussed later.

Additional AES results associated with the TEM studies, the aluminum carbide formation and the model systems are described in detail in the appropriate appendices.

C. TEM of the Aluminum-Graphite Interface

To determine the phases present at the interface, TEM was performed on the composites. This included both the commercial and the model systems. Both electrochemical thinning and ion thinning techniques were used to prepare samples. The electrochemical thinning techniques are described in detail in Appendices C and D. The ion thinning technique was used toward the end of the research with limited experimental results. The Al-graphite composite was cut carefully in the longitudinal direction by a diamond wheel blade and the ion-beam thinning technique was used. In each ion

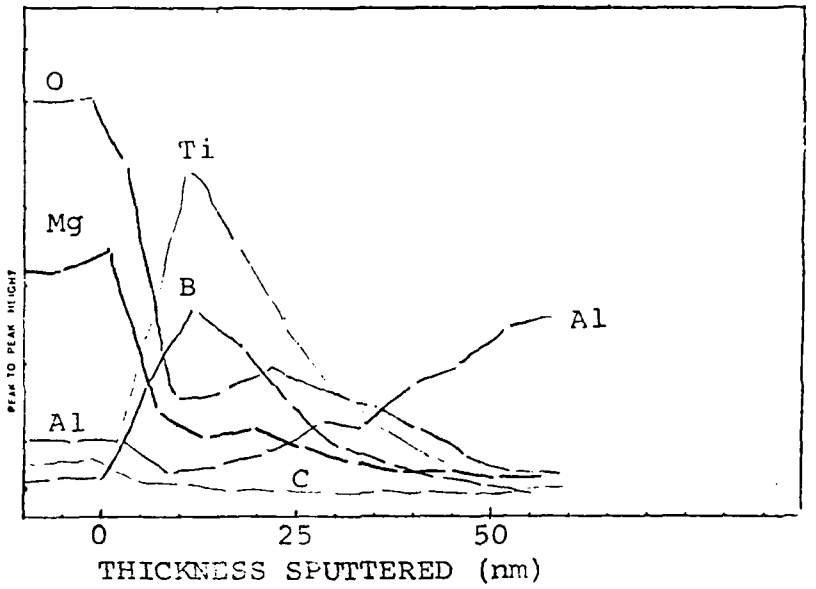

Fig. 4. High spatial resolution AES sputtering profile into matrix surface of VSB-32/6061 composite fractured in situ, showing details of the complex interface chemistry.

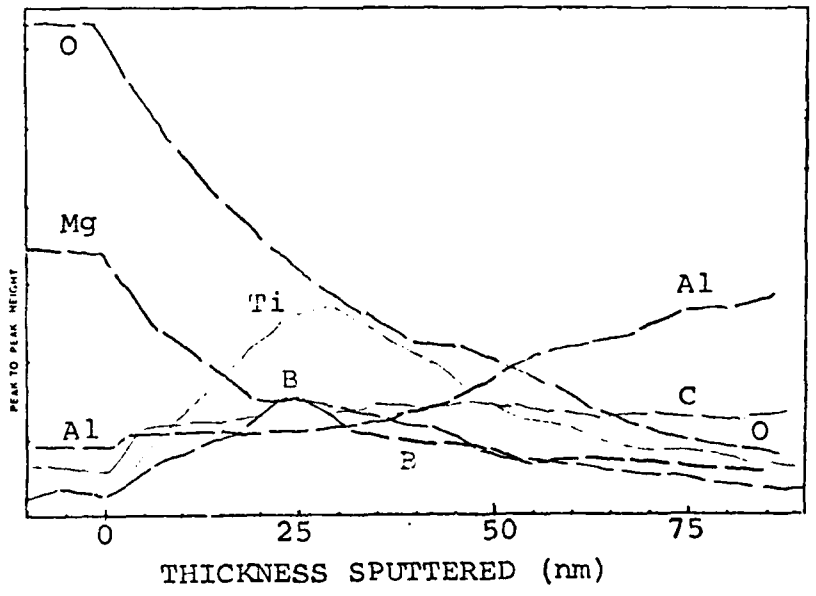

Fig. 5. High spatial resolution AES sputtering profile into matrix surface of VSB-32/oxide/6061 composite fractured in situ, which can be compared to Fig. 4.

sputtering the sample was tilted 20° with respect to the ion beam. It was found that by using 4 kv or lower accelerating ion beam voltage, the graphite fiber would be thinned faster than the Al-metal-matrix. With the voltage 4.5 kv or higher, the Al-metal-matrix would thin faster than the graphite fiber. To get fairly uniform thinning, the 4.5 kv accelerating ion beam voltage was used first and then the voltage was lowered to 4 kv until the sample was thinned down. This approach resulted in uniform thinning of the graphite and aluminum. Some results from this type of thinning procedure are discussed in the Al/discontinuous SiC composites section.

The chemical thinning techniques led to identification of the many phases at the interface. The presence of an oxide was confirmed and identified as the spinel structure of $MgAl_2O_4$ and γ-Al_2O_3. It had been reported that α-Al_2O_3 was the oxide phase at the interface[4,5]. This present study clearly demonstrated that γ-Al_2O_3 was the phase formed. This was found for both the commercial and the model systems. Similar results were observed in the Mg/Graphite metal matrix composites. In that case the $MgAl_2O_4$ was identified. The interface chemistries were determined with AES.

In general a wide range of phases were found at the interface depending on the source of the composite and the subsequent thermal treatments. In addition to γ-Al_2O_3 and $MgAl_2O_4$, TiB_2, Al_4C_3 and Al_4O_4C were also identified The details of the TEM results are given in Appendices C and D.

D. Aluminum Carbide Formation in Aluminum-Graphite Composites

The formation of a thick layer of Al_4C_3 is known to increase the transverse strength of the composite. Unfortunately the longitudinal strength is greatly reduced. To determine the kinetics of the Al_4C_3 formation a series of experiments were performed on both the composites and model systems. Details of these results are given in Appendices E and F. The most important aspects of the study were related to the surface condition of the graphite, the environment in which the heat treatment was performed and the crystallographic orientation of the graphite. When an oxide layer exists at the interface of the commercial composites between the aluminum matrix and the graphite experimental results indicate the carbon diffuses through the oxide and forms the Al_4C_3 adjacent to the alloy. This was not observed in the glassy carbon model system.

The three model systems used had graphite single crystals with the (0001) parallel to the surface, polycrystalline graphite and glassy carbon substrates. When heat treatments were performed in an inert environment no detectable carbide was formed on the single crystal. For the polycrystalline case the Al_4C_3 was formed preferentially on selected grain orientations. For the glassy carbon a much more isotropic formation of the carbide was observed.

The other critical observation was that in the presence of a mechanical pump vacuum where a large amount of hydrocarbons were present carbide formation was promoted. Hydrogen is suspected to be the element that promotes the nucleation of the carbide. In a

higher oxygen bearing environment a thick interface oxide is developed. Further discussion is given in Appendices E and F.

E. Residual Stresses in Al/Gr Composites

During the development and subsequent carrying out of the research on transverse strength of the Al/Gr composites the main cause of the weakness was expected to be the interface strength. A secondary possibility was that the residual stresses arising from the large mismatch in thermal expansion coefficients between the graphite fibers and the aluminum matrix would add to the applied stress and cause failure. To determine if the presence of residual stress could explain the extremely low transverse strength when compared to the rule of mixtures the residual stress was measured using x-ray techniques. The original effort was in a joint effort with J.B. Cohen at Northwestern and the subsequent experiments were performed in our laboratory. The experimental techniques and results are presented in Appendix G. The results show high average tensile residual stresses in the aluminum matrix for both the Rayon and PAN II fibers and intermediate stresses for the pitch base fibers. The lower residual stresses in the pitch base composites were difficult to rationalize with their higher degree of texture and modulus.

In order to determine if the transverse strength was a function of the residual stress, room temperature tensile tests were made on samples, some before a liquid nitrogen quench and some subsequent to a liquid nitrogen test. The liquid nitrogen quench and

subsequent reheating to room temperature resulted in about a 30-40% reduction in the residual stress pattern. This large change in residual stress was not reflected in the room temperature tensile tests where a very small increase was noted.

Based on the above results the conclusion is that although residual stresses even higher than the yield strength of the material exist, they do not play a major role in the transverse strength.

F. Studies of Discontinuous Fiber Silicon-Carbide/Aluminum Composites

Although six silicon carbide/Al composites were made available only the A6013Z composite was studied in any detail. The A6013Z composite was SXA 2024 + 22.45 w/o F-9 Grade Silicon Carbide in a flat as-extruded plate 1/2" x 5" x 1 7/8". The Si-Carbide/Al composite materials were tensile tested using standard Instron tensile testing equipment. Rectangular specimens with a 0.5 inch gauge length were carefully machined from composite plate. Four tabs were carefully glued onto each specimen using a high shear strength epoxy, Miller-Stephenson type 907 adhesive. A crosshead speed of 1 mm/min and 10 kN full scale were used for testing the Si-Carbide/Al composites. The tensile strength of the A6013Z composite was 66 ksi. The other six materials ranged in strength from 43 to 65 ksi. All the materials showed very limited ductility. The fracture surface consisted of small ductile dimples. Virtually no interfaces were observed under high resolution SEM.

The fibers were less than 1 μm in diameter making it almost impossible to examine any individual fibers on the fracture surface

with our AES with a resolution of the same order of magnitude. AES data averaged over the fracture surface showed virtually no presence of silicon carbide. This is shown in Fig. 6. After extensive inert ion sputtering, approximately 0.5 μm, the silicon carbide was observed as shown for one area in Fig. 7. The distribution was non-uniform across the sputtered section, but the silicon carbide was present in all the sputtered areas. The need to sputter to a great depth to get a substantial silicon carbide spectrum gives strong support for high interface strength.

The TEM of the silicon carbide/aluminum interface defined the following. Jet polishing experiments resulted in identification of β-Al_4SiC_4 at the interface as shown in Fig. 8 with the diffraction pattern in Fig. 9. More extensive studies on ion thinned samples (4.5 kV - 20° incident angle for uniform sputtering) showed clean interfaces the more common condition. It must be clear that a very thin interface layer, similar to that observed in the Al/graphite would be difficult to identify under the ion etching conditions used in these experiments.

G. Related Auger Electron Spectroscopy Investigations

During the course of this research several AES studies were made on related systems to help in interpreting the main results in this report. Appendix H describes results obtained during studies of oxidation of a titanium/molybdenum alloy aimed at developing a standard for calibration of inert ion sputtering rate.

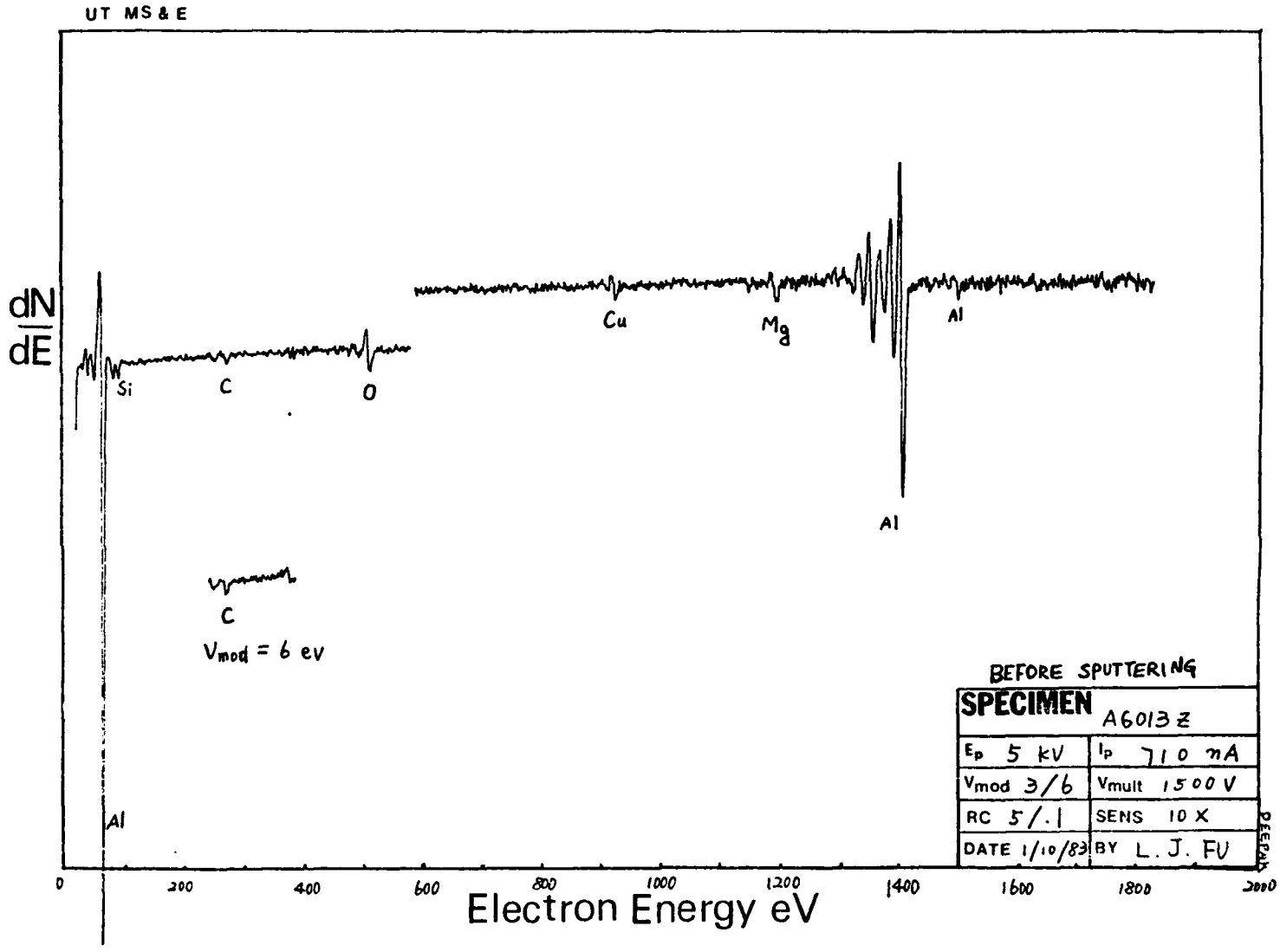

Fig. 6. Low spacial resolution AES of fractured surface of A6013Z SiC/Al MMC.

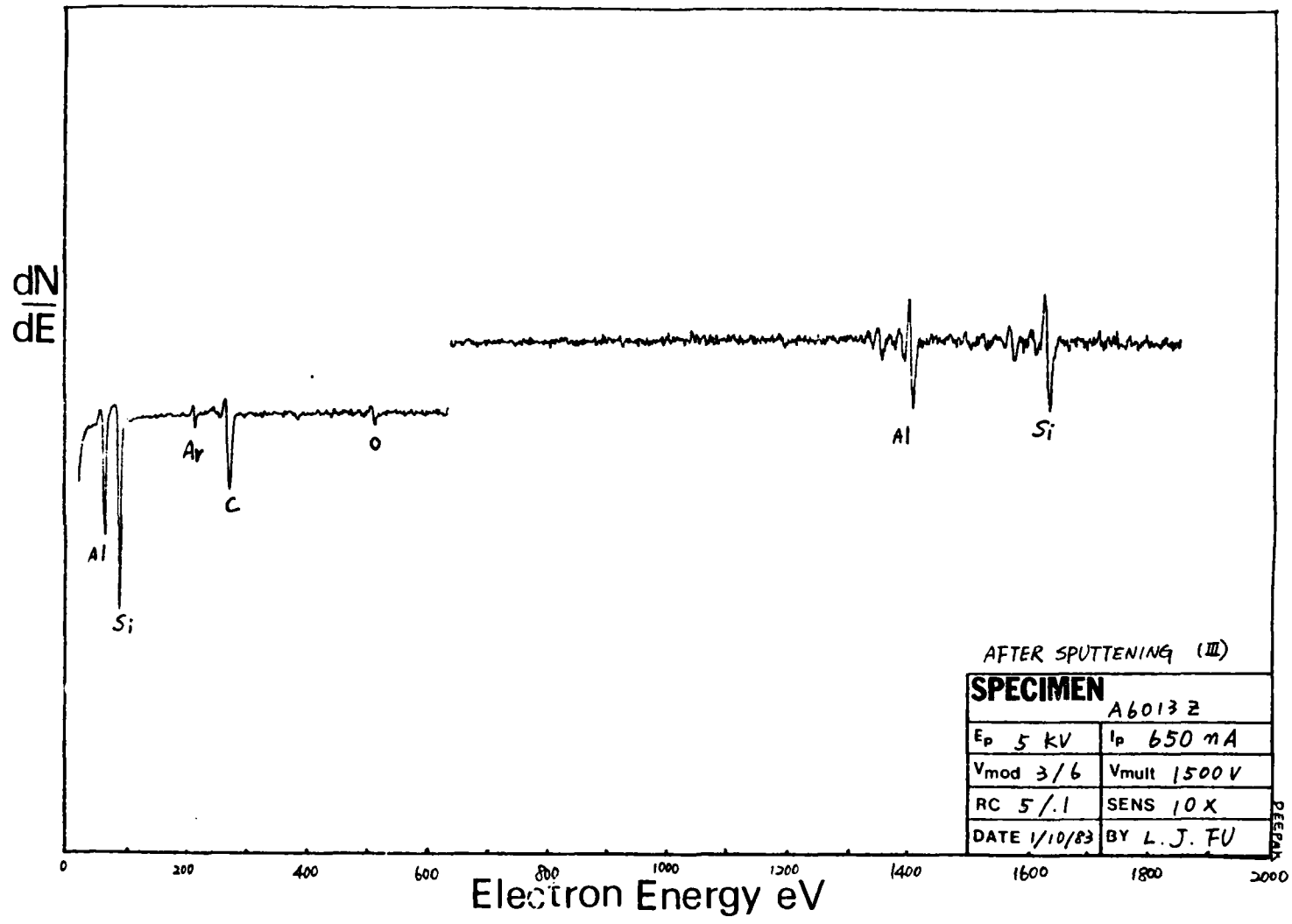

Fig. 7. Low spacial resolution AES of fracture surface of A6013Z SiC/Al MMC after inert ion sputtering approximately 0.5 μm.

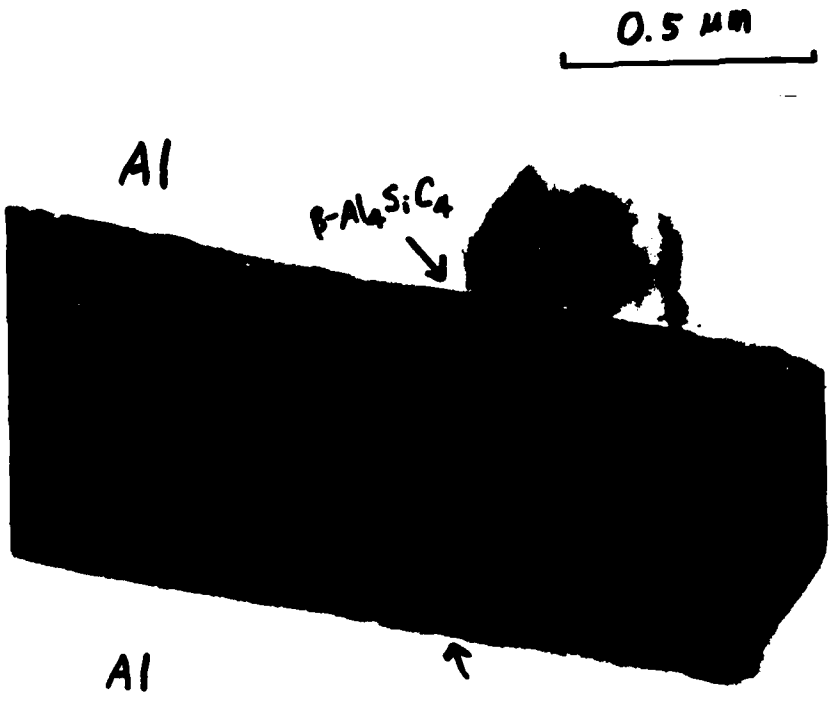

Fig. 8. TEM of A6013Z SiC/Al MMC showing β-Al_4SiC_4

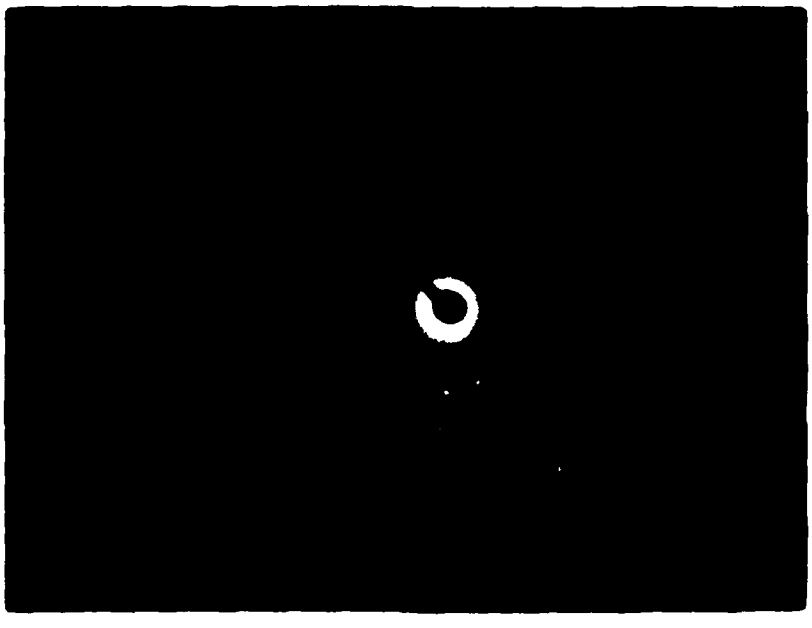

Fig. 9. TEM diffraction pattern of β-Al_4SiC_4

The results were correlated with voltammograms of pure Ti and Mo leading to an evaluation of the oxidation states in the oxide.

In Appendix I the problem of determining the interface thickness of two elements segregated to an interface was probed. The two elements, in this case S and Ni, were both at grain boundaries. Sputter profiles as normally measured indicate that S is near the fracture surface and Ni is more diffusely segregated. The results of the study clearly support the concept of preferential sputtering of the S due to its weaker bonding and that the true spacial distribution is similar in both cases.

In Appendix J a joint study with Chiang et al. on the grain boundary segregation within an oxide is described. The research tries to separate out and describe the relative importance of size effects and space charge theory on the grain boundary chemistry in oxides. In all oxides the valence of a migrating species must be accounted for before sputter profiles could be explained.

In Appendix K the general problems associated with applying AES to fracture are discussed. In addition, of particular importance to the present research, is a discussion of the interaction between the electron and ion beams and a carbon containing surface. The damage to the bonding of the carbon is explored and the dangers of attempting to interpret the AES fine structure are described. In addition other approaches to probe the surface are discussed. The details of these associated AES studies are in the above referenced Appendices.

III. Summary

The results of the research on aluminum/graphite interfaces described in this final report can be summarized in terms of the experimental approaches used to probe the metal matrix interfaces. The materials studied included the commercial Al/graphite composites; layered model systems on single crystal and polycrystalline graphite substrates as well as glassy carbon substrates; and discontinuous fiber SiC/Al composites. The I/V characterization of the interface demonstrated that the oxide within the interface plays a major role in the interface strength. If the interface was in a low conductivity state, peel test fractures occurred at the interface, weaving through the oxide. When the interface was switched into an electrically conductive state peel test fractures occurred within the single crystal graphite substrate. The interface strength was directly correlatable with its conductivity state in the Al/γ-Al_2O_3/(0001) graphite model system. The commercial material measurements were indecisive.

TEM of the commercial materials and the model laminates showed the presence of γ-Al_2O_3, $MgAl_2O_3$ and TiB_2 in the as-prepared samples. No aluminum carbide was found. The presence of the oxide seemed to be required to get some transverse strength. When samples were aged within the solid state region, Al_4C_3 and Al_4C_4O were found. Their growth was strongly dependent on the heat treat environment, the temperature, and the crystallography of the graphite relative to the interface. Basal plane orientation of the graphite prevented any carbide formation unless an external hydrocarbon containing

environment was present during the heat treatment. When carbides were formed the transverse strength increased but the longitudinal strength was dramatically reduced.

AES was used to characterize the fracture surface chemistry. Inert ion sputtering profiles confirmed the presence of the oxide adjacent to the graphite, the TiB_2 displaced toward the matrix. AES after heat treatment of the commercial composites showed the carbon diffused through the oxide to form the carbide. This was not consistently observed in the model systems.

A series of AES related experiments were performed relative to oxide formation, diffusion in an oxide, preferential sputtering and artifacts on carbide peak analysis due to electron and ion beam damage.

X-ray measurements of the residual stress of the commercial composites shows tensile stresses some of which were greater than the yield strength of the aluminum matrix. Liquid nitrogen quenching greatly reduced the stresses with minimal influence on the transverse fracture strength. The results support the conclusion that the residual stresses do not control the transverse strength.

The fracture study of discontinuous fiber SiC/aluminum composites showed indications of a strong interface. AES measurements show the fracture path was remote from the interface. TEM showed the presence of β-Al_4SiC_4 at some interfaces, but a lack of phases at other interfaces.

Additional details of the research discussed in this report can be found in the PhD dissertations of Swe-Den Tsai[6] and Duane Finello[7] and the Master's theses of James Lo[8], Li-Jiuan Fu[9] and Horacio Mendez[10].

IV. References

1. H.L. Marcus, "Interface Character of Aluminum-Graphite Metal Matrix Composites," Annual Report, ONR Contract N00014-78-C-0094, December 1979.

2. H.L. Marcus, "Interface Character of Aluminum-Graphite Metal Matrix Composites," Annual Report, ONR Contract N00014-78-C-0094, December 1980.

3. H.L. Marcus, "Interface Character of Aluminum-Graphite Metal Matrix Composites," Annual Report, ONR Contract N00014-78-C-0094, January 1982.

4. Private communication with Dr. Hugo Steinfink.

5. B.C. Lippens and J.H. deBoer, Acta Cryst. 17, 1312-1321 (1964).

6. Swe-Den Tsai, "The Characterization of the Interface in Graphite-Aluminum Composite Systems," PhD Dissertation, The University of Texas at Austin, December 1980.

7. Duane Finello, "Interfacial Behavior of Graphite-Aluminum Composites," PhD Dissertation, The University of Texas at Austin, August 1982.

8. James Lo, "The Characterization of the Interface in Metal Matrix-Graphite Fiber Composites," Master's Thesis, The University of Texas at Austin, December 1981.

9. Li-Jiuan Fu, Master's Thesis, In preparation (May 1983).

10. Horacio Mendez, Master's Thesis, In preparation (May 1983).

Appendix A

CORRELATION OF ELECTRONIC STATE AND FRACTURE PATH OF ALUMINUM-GRAPHITE INTERFACES

Horacio Mendez†, Duane Finello†, Rodger Walser* and H.L. Marcus**
†Graduate Students in Materials Science and Engineering
*Professor of Electrical Engineering/MS&E
**Harry L. Kent Professor of Mechanical Engineering/MS&E
The University of Texas, Austin, Texas 78712

(Published in Scripta Met., July 1982)

Introduction

It has been observed (1) that the thickness of the oxide layer at the interface between aluminum and graphite has an important influence on the interface bonding strength. When the oxide films are thin, the interface is more cohesive and strongly bonded to the graphite. This produces a fracture path through the graphite single crystal substrate. As the oxide thickness is increased the interface bonding strength is modified and the fracture path is through the interface. Similar behavior has been observed in commercial graphite-aluminum composite material (2).

The purpose of this paper is to report the interaction of the threshold switching characteristics of the aluminum/Al-oxide/graphite system with the mechanical strength of the oxide-graphite interface. With the aid of Auger electron spectroscopy (AES) it was determined that the fracture path through the oxide sandwiched aluminum-graphite interface can be altered from fracture within the interface to fracture in the substrate by applying a voltage above the threshold voltage.

Threshold switching has been observed in many different semiconductor systems. It is described as an abrupt change in resistivity of the specimen when subjected to sufficiently high electric fields (3,4). When the applied voltage across the junction is increased above a certain threshold voltage, the resistivity abruptly decreases and will remain in the low resistivity state for some time.

One of the characteristics of threshold switching is that the material may have a memory behavior such that once the device has been set into the low resistivity state, it may become stable and remain stable for a relatively long time after the voltage has been removed. The amount of time that the sample stays in the low resistance state depends on the specific type of system and it is strongly dependent on the temperature. As the temperature is decreased the memory time is increased.

Another important feature of switching is the requirement of a forming voltage. This forming effect consists of a dramatic reduction of the threshold voltage (to a constant value) after the first switching event has occurred. This phenomenon is generally not associated with the switching process but rather with the contact at the probes (4), it can be minimized using sufficiently clean electrode conditions.

Experimental Procedure

Natural graphite crystals dissolved from Ticonderoga marble were selected to obtain single crystalline material. These crystals naturally form a flake shape of graphite with the basal planes parallel to the surface of the crystals. The aluminum/Al-oxide/graphite samples were prepared by vacuum evaporation in a two-step process. In the first step the graphite crystals were properly cleaned and masked and a low vacuum, 3×10^{-2} Pa, aluminum oxide deposition was performed at a slow deposition rate. Following the oxide deposition a high vacuum deposition, 10^{-4} Pa, of commercially pure aluminum was done at a high deposition rate, to produce the top aluminum layer as shown in figure 1.

Argon ion sputtering combined with AES showed that the Al-oxide was 30 to 50 nm thick. The oxide was identified as γ-Al_2O_3 (5).

To determine the switching character of the composite, a voltage was applied across the interface, by placing one probe at the Al-metal dot and one probe at the graphite crystal as shown in figure 2.

The I-V curve measurements were made with a curve tracer. Characteristic high resistivity state and low resistivity state are shown in figure 3.

After one of the dots switched from high resistivity state to low resistivity state it was fractured by peeling while still in low resistivity state. The graphite substrate was held in place by a vacuum. Then by placing a quick drying glue at the tip of a probe, the center portion of the aluminum dot was peeled away from the crystal by lifting the probe. The second dot was fractured under the same loading conditions, but while still in the high resistivity state.

On a second set of samples, a voltage was applied and the samples switched to the low resistivity state, but sufficient time was allowed for the sample to return to the high resistivity state. The samples were then fractured using the same loading procedures.

All of the samples were analyzed using Auger electron spectroscopy in order to determine the fracture path associated with the different resistivity state of each sample. Both sides of the fracture surface were analyzed.

Experimental Results

The Auger spectra showed that in samples fractured in the low resistivity state, the fracture path was through the single crystal graphite substrate, as described in figure 4.

For samples fractured in the high resistivity state, the fracture path weaved through the Al-oxide layer near the graphite interface, as shown in figure 5.

The samples which were switched to the low resistivity state, but which were given sufficient time after removal of the voltage to relax back to the high resistivity state showed a fracture path weaving through the aluminum oxide near the graphite interface, similar to the unswitched samples. The corresponding Auger spectra are shown in figures 6 and 7.

Discussion and Conclusions

The results introduced in this paper make it evident that the two different resistivity states introduced by the switching mechanism present in the aluminum/aluminum oxide/graphite layered system can be directly associated with the strength of the interface. The strength of the interface of this system can be increased by applying a voltage above the threshold voltage forcing fracture to occur in the substrate graphite single crystal.

The reversal of the strength of the interface when the system relaxes back to the high resistance state is a strong indication that no permanent phase change occurred at the interface during the excitation to the high conduction state. The fracture reverted back to be within the oxide interface region.

The results clearly demonstrate that the nature of interface bonding as reflected by its conductivity can be modified by a change in conduction state resulting in a change in preferred fracture path.

A more detailed study of the I-V characteristics combined with the mechanical stability of the system is presently in progress to gain more understanding of this correlation and to extend it into other interface systems.

Acknowledgment

This research was supported by the Office of Naval Research under contract N00014-78-C-0004.

References

1. Swe-Den Tsai, PhD Dissertation, The University of Texas at Austin, 1980.
2. H.L. Marcus, D.L. Duil and M.F. Amateau, Failure Modes in Composites IV, pp. 308-318, The Metallurgical Society of AIME, New York (1979).
3. D.F. Weirauch, App. Phys. Letters 16, 72 (1970).
4. H.J. Hovel and J.J. Vegell, J. Appl. Phys. 12, no. 42 (1971).

5. James Lo, Masters Thesis, The University of Texas at Austin, 1981.

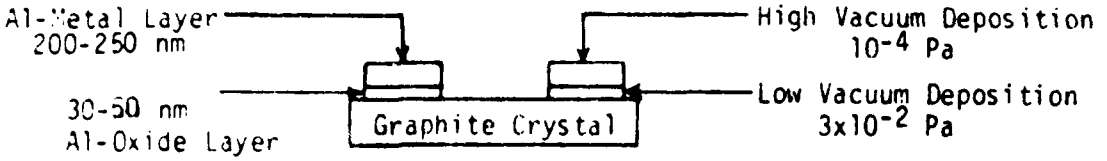

FIG. 1
Description of aluminum/aluminum oxide/graphite samples prepared by vacuum evaporation.

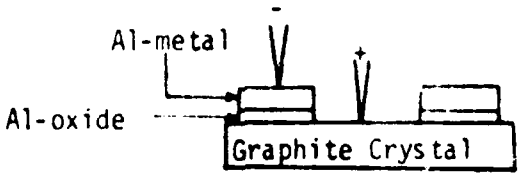

FIG. 2
Application of voltage across the interface of the aluminum/aluminum oxide/graphite system.

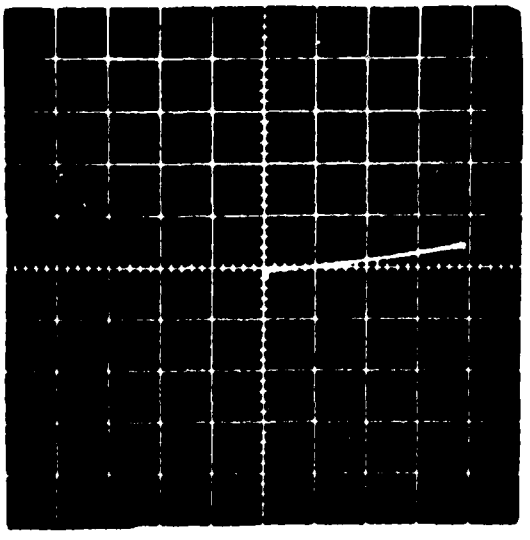

FIG. 3(a)
High resistivity state in Al/Al-oxide/graphite system
Scale: Horizontal: 0.2 volts/div
Vertical: 0.2 mA/div

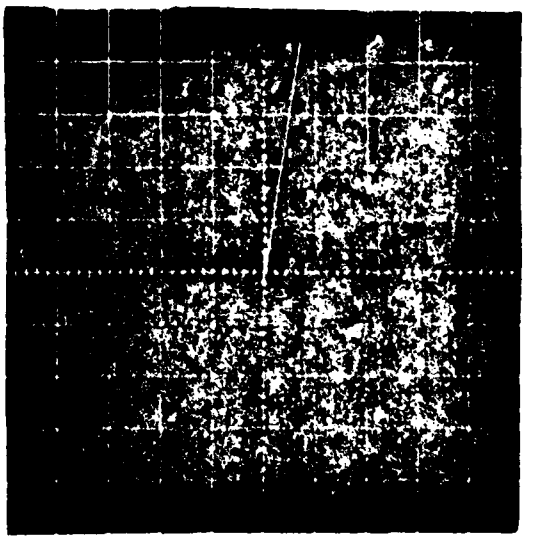

FIG. 3(b)
Low resistivity state in Al/Al-oxide/graphite system
Scale: Horizontal: 0.2 volts/div
Vertical: 0.2 mA/div

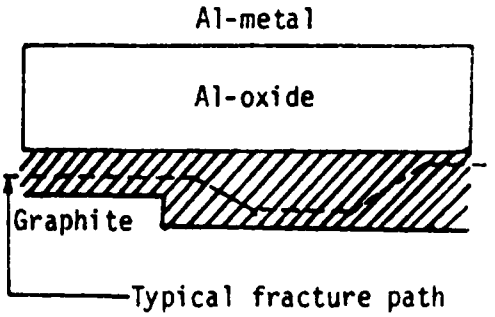

FIG. 4
Fracture path of samples fractured in the low resistivity state.

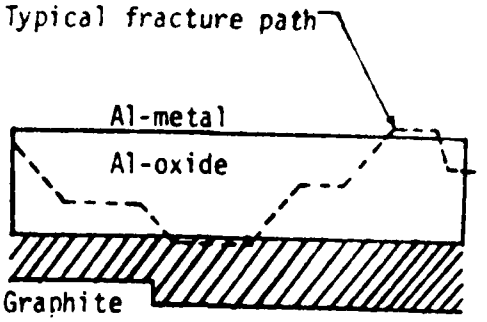

FIG. 5
Fracture path of samples fractured in high resistivity state. Similar path observed in samples allowed to relax from the low resistivity state to the high resistivity state.

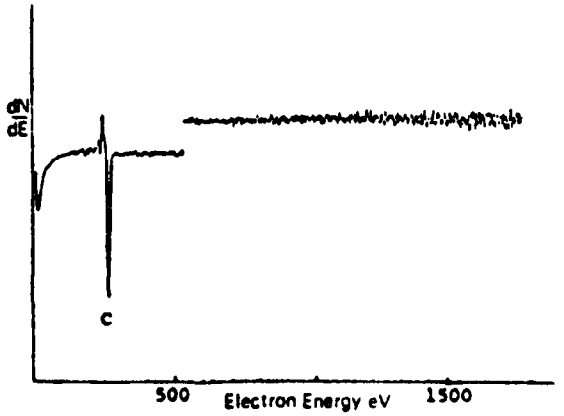

FIG. 6
Auger spectrum of samples fractured in the low resistivity state.

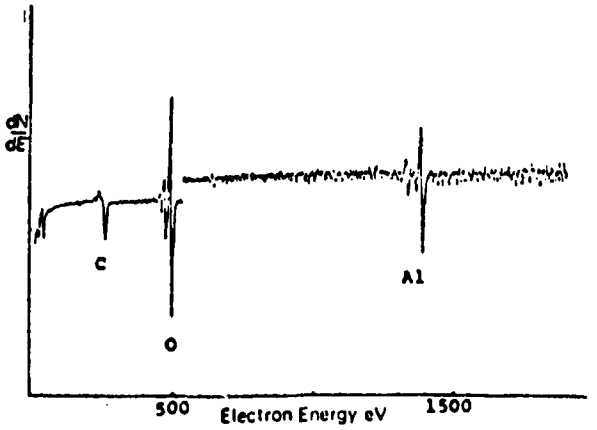

FIG. 7
Auger spectrum of samples fractured in the high resistivity state. Similar spectrum was observed in samples allowed to relax from the low resistivity state to the high resistivity state.

Appendix B

I/V TESTING OF COMMERCIAL GR/AL WIRE

The current versus voltage behavior was examined for samples of VSB-32/6061 and VSB-32/oxide/6061 Gr/Al composite wire. Sections of composite wire two centimeters in length were etched so as to expose bare graphite fibers one centimeter in length. This was done by applying lacquer to each specimen before etching to enable half its length to remain unetched during upright suspension of the specimen in 50% hydrochloric acid-50% methanol solution for a period of thirty minutes. Afterwards, a methanol rinse and a short drying period prepared the specimens for electrical lead attachment. A length of 30 gauge bare copper wire was tied to each bare row of fibers well away from the matrix and a drop of conductive silver paint was applied. The specimen configuration is illustrated in Fig. B-1. Flat-nosed miniature copper "alligator" type clips sufficed for hookup to a curve tracer for the conductivity measurements.

The results of the conductivity measurements for the commercial Gr/Al wire I/V specimens are presented in Table B-1. A switching effect similar to what was observed for pure thin layer composite model systems was not found. The likelihood of a fixed conductive state in as-received commercial composite material suggests that oxidizing the fiber/matrix interface should alter this condition. Short term air furnace heat treatments at 550°C designed to limit fiber degradation did not promote switching, although an oxide layer growth of 50 nm per hour was anticipated during thermal exposure.

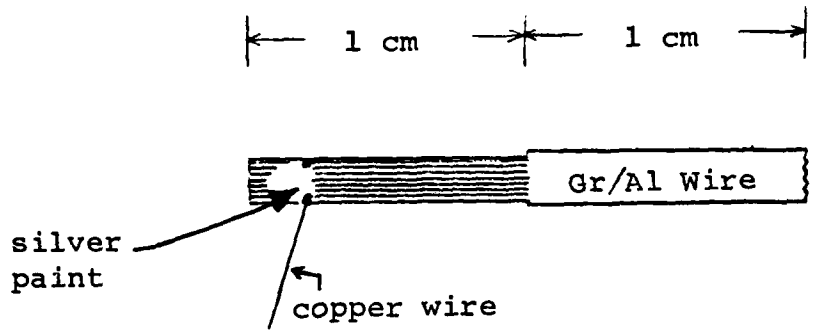

Figure B-1

Commercial Gr/Al composite I/V specimen configuration.

Table B-1

RESULTS OF I-V MEASUREMENTS FOR COMMERCIAL Gr/Al

Material	Condition*	Interfacial Oxide Thickness (nm)	Conductance (mhos)
VSB-32/6061	No Ht	5	0.6
VSB-32/oxide/ 6061	No Ht	15	0.6
	AFA - ½hr	25	0.7
	AFA - 1hr	50	1.0
	AFA - 1½hr	75	0.6

*No Ht - As received
AFA = Air furnace aged at 550°C.

(Twenty-four hour air furnace aging of commercial Gr/Al produces interfacial oxide thicknesses on the order of one micron; such interfaces are much less conductive since they present electron beam-induced charging problems during AES analysis). I/V measurements for commercial Gr/Al subjected to more thoroughly oxidizing heat treatments were not attempted since the experimental difficulties associated with fiber breakage were serious using the short term oxidizing heat treatments.

One should realize that this type of commercial Gr/Al composite I/V specimen contains thirty times the internal interfacial area that the typical simulating thin layer composite model system has. (The model system described in Appendix A has an interfacial area of approximately 0.1 cm^2, while the commercial composite I/V specimen system used here has an interfacial area of 3 cm^2). In order for the commercial specimens to be in the low conductance state, each should have a net conductance of only 30/(350Ω) or approximately 0.1 mho. However, they have conductances in excess of this value, approaching one mho. The data are in better agreement with an interface in the high conductance state, although short-circuit current patns may be the cause.

Since switching was not observed in commercial Gr/Al composites, there is a reasonable likelihood of a fixed conductive state for the fiber/matrix interface. However, further refinement of the experimental techniques may show that commercial Gr/Al materials can be switched from low to high conductance states and be used to characterize the interface strength.

Appendix C

INTERFACE STRUCTURE OF HEAT-TREATED ALUMINUM GRAPHITE FIBER COMPOSITES

James Lo, Duane Finello, Michael Schmerling and H.L. Marcus

Mechanical Engineering Department
Materials Science and Engineering
The University of Texas
Austin, Texas 78712

(To be published in Proceedings-Composites Seminar, 1982 AIME Annual Meeting)

Summary

The interface of aluminum graphite metal matrix composites was characterized with TEM. The heat treatment of the composite results in carbide formation and degradation of graphite fibers. The fracture path shifts from within the oxide layer to either the fiber interface or within the fiber itself with longer aging time. Aluminum carbide was observed at aging temperatures above 550°C with the only aluminum carbide phase observed being Al_4C_3. Very coarse grains of Al_4C_3 imply preferred orientations of carbide formation due to the anisotropicity of graphite. Al_4O_4C is the only aluminum oxycarbide phase observed at the interface of aluminum graphite fiber composites. It forms a fine grain distribution at all aging temperatures.

Introduction

Aluminum and aluminum alloy metal matrices in graphite fiber reinforced composites are promising systems for structural applications. A major problem is the poor transverse tensile strength in contrast to the high longitudinal tensile strength. Recent studies (1,2) indicate that there is a close relationship between interface composition and morphology and mechanical behavior. In this study, the transverse tensile strength of the aluminum-graphite fiber composite was improved slightly when the aging temperature was raised above 500°C. Meanwhile, longitudinal tensile strength decreased noticeably as reported elsewhere (3).

The specimens in this study include G4371 and G4411,* both of which have Al-6061 as metal matrix and VSB-32 pitch fibers. They were either encapsulated in various vacuum conditions 10^{-3} - 10^{-8} torr (10^{-1} - 10^{-6} Pa) and heated to 400°C - 640°C or heated to the same temperatures without encapsulation, then naturally aged. The heat-treated specimens show the results of changes in the interface regions. Compounds at the interface that are crystalline were analyzed by using the selected area diffraction (SAD) technique in the transmission electron microscope (TEM). Crystallographic information about the interface reaction zone was obtained by examining the diffraction patterns from sections of the interface.

Experiments

The best way to get separate fibers from aluminum-graphite fiber composites without loss of major interface compounds is by using an etching solution which is prepared by dissolving 3 grams of NaOH or KOH in 100 ml of high purity methanol (containing 0.03% water) with frequent stirring. High purity methanol is used instead of water as solvent for preparing the alkali etching solution to avoid dissolution of aluminum carbide in water (4). As a test, pure aluminum carbide powders were immersed for five hours in the etching solution without indication of dissolution. The powders were washed by high purity methanol and dried completely at about 60°C. Only the spectrum of aluminum carbide appeared when the powder was examined by x-ray diffraction. At the present time, this solution is the only one that has proved to be effective for preserving the Al_4C_3 and Al_4O_4C in the aluminum-graphite fiber composites.

A JEOL 150 kV TEM was used in the SAD studies. Interface regions still attached to separate fibers were examined with applied voltages of 100 kV and 150 kV. The camera constants are 17.8 ±0.3 mm Å and 13.7 ±0.2 mm Å, respectively.

Results and Discussion

γ-Al_2O_3 or $MgAl_2O_4$ spinel and TiB_2 were observed in the interface regions of non-heat-treated specimens (5) as well as in the aged specimens. Smaller amounts of TiB_2 phase were found when the specimens were aged above 550°C. This was partly caused by displacement of the Ti-B layer away from the fiber into the matrix (2) and partly by dissolution of TiB_2 into the metal matrix during carbide formation. The specimens aged above 550°C showed aluminum carbide (Al_4C_3) and aluminum oxycarbide (Al_4O_4C) existing

*Supplied by the Aerospace Corporation.

in the interface. Their diffraction patterns are shown in Fig. 1 and 2.

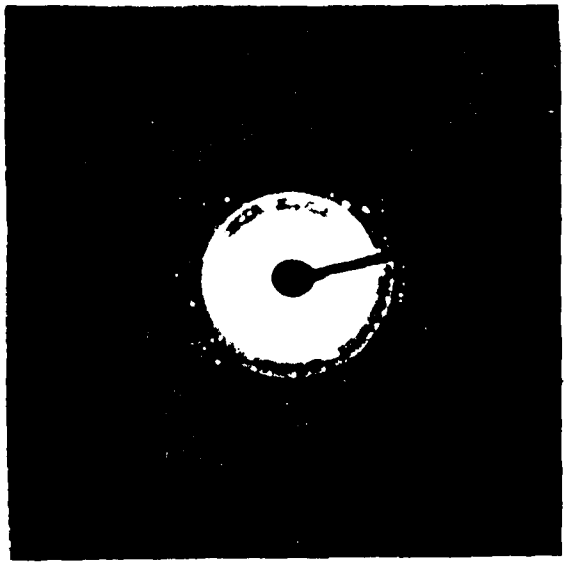

Figure 1 - Selected area diffraction pattern of Al_4C_3 from the interface of G4371 heat-treated above 550°C.

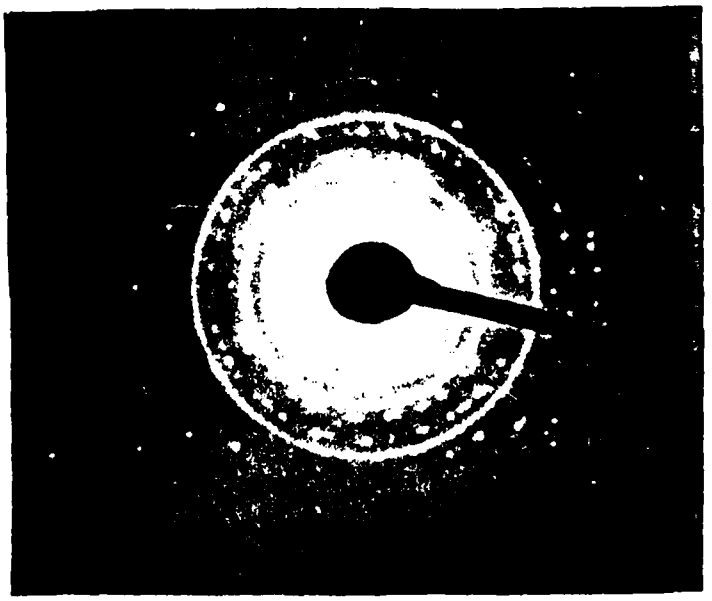

Figure 2 - Selected area diffraction pattern of Al_4O_4C from the interface of G4371 heat-treated above 550°C.

Carbide formation seems to occur preferentially on specific orientations of the basal plane of the graphite with respect to the interface. Some orientations make nucleation of the carbide difficult and restrict their growth such that coarse grains form. The spotty nature of the Al_4C_3 diffraction pattern is due to the large grains. There seems to be no restriction on the Al_4O_4C nucleation and growth since it forms fine randomly oriented grains for specimens aged as high as 640°C as indicated by the continuous diffraction pattern in Fig. 2.

The higher the aging temperature, the more severe the interface reaction, and the greater the grain growth, see Figure 3. The interface region serves as diffusion path for carbon resulting in carbide formation with fiber surface pitting evident. This pitting phenomena can cause premature longitudinal failure in the fibers due to the local stress concentration. In the aged specimen, fibers are often pulled out of the fracture surface during the tensile testing. No interface compounds were found attached to graphite fibers pulled out directly from the specimens aged at temperatures above 550°C. This lack of interface material indicates that the fracture path was within the interface or in the degraded graphite fibers.

(a)

(b)

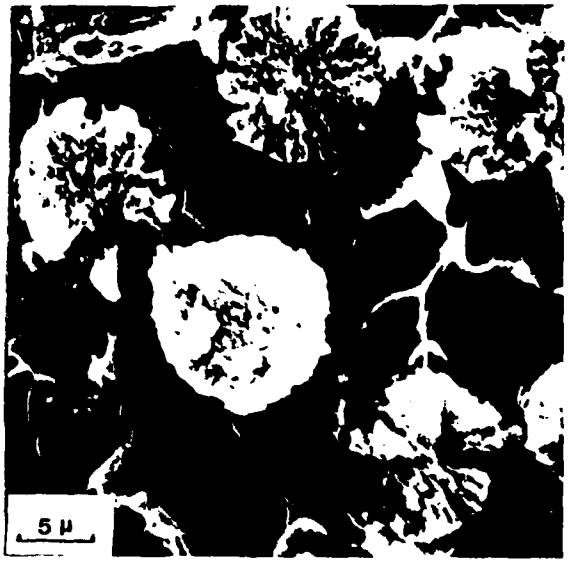

(c)

Figure 3 - Scanning electron micrographs of the interface regions of G4371 heat treated at increasing temperatures. (a) Non-heat treated. (b) 550°C at ~$5x10^{-7}$ torr for 1 day. (c) 640°C at ~$5x10^{-8}$ torr for 1 day.

Conclusions

1. Heat treatment allows carbide formation and degradation of graphite fibers to take place simultaneously.
2. The fracture path shifts from in the oxide layer to either the fiber interface or within the fiber itself with increased heat treatment.
3. Formation of aluminum carbide at aging temperatures above 550°C was observed with the only aluminum carbide phase observed being Al_4C_3. Very coarse grains of Al_4C_3 imply preferred orientations of carbide formation due to the anisotropicity of graphite.
4. Al_4O_4C is the only aluminum oxycarbide phase observed at the interface of aluminum graphite fiber composites. It forms a fine grain distribution at all aging temperatures.

Acknowledgements

The authors would like to thank Swe-Den Tsai for his discussion. This research was supported by the Office of Naval Research, contract N00014-78-C-0094.

References

1. G.L. Steckel, R.H. Flowers, and M.F. Amateau, "Transverse Strength Properties of Graphite-Aluminum Composites," Final Report for Period 1 Oct 1977 - 30 Sept. 1978 for Naval Surface Weapons Cente. TOR-0078 (3726-03) -4, Sept. 30, 1978.

2. H.L. Marcus, D.L. Dull and M.F. Amateau, "Scanning Auger Analysis of Fracture Surfaces in Graphite-Aluminum Composites," in Failure Modes

in Composites IV, J.A. Cornie and F.W. Crossman, eds.; Conference Proceedings, The Metallurgical Society of AIME (Fall 1977).

3. P.W. Jackson, Metals Engineering Quarterly, ASM 9, No. 3, pp. 22-30, 1969.

4. T.Y. Kosolapora, Carbides, translated by N.B. Vanghan, Plenum Press, New York, 1971.

5. Swe-Den Tsai, PhD Dissertation, The University of Texas at Austin, 1980.

Appendix D

Published in Ceramic Engineering and Science Proceedings, v. 2, 1981

THE INTERFACE STRUCTURE IN GRAPHITE/ ALUMINUM COMPOSITES

Swe-Den Tsai, Michael Schmerling
and H.L. Marcus
Mechanical Engineering/
Materials Science and Engineering
The University of Texas
Austin, TX 78712

Abstract

Transmission electron diffraction and Auger electron spectroscopy studies of the interfaces of selected graphite/aluminum composite systems revealed that generally titanium diboride, (TiB_2), and aluminum oxide, (γ-Al_2O_3), were present as the interfacial phases. The grain size and the crystallographic structure of these interfacial phases were studied and are discussed in terms of the transverse fracture behavior of the graphite/aluminum composites.

Introduction

The graphite fiber reinforcement/metal matrix composites are of great interest because of their high strength and potential for large-scale production and use. Aluminum alloys appear promising as matrix materials for graphite reinforced metal. In the majority of cases the fiber is pretreated followed by controlled immersion into molten aluminum to make the metal matrix composite[1]. Even as this liquid metal infiltration technology advanced, the transverse strength of graphite-aluminum composites remained poor in contrast to the high strength in the longitudinal direction. A recent study[2] indicated that the transverse behavior should be closely related to the interfacial properties. This interface could be the reaction zone between aluminum and fiber or the reaction zone between pretreatment coating and either the fiber or matrix.

Some variations in the treatment of graphite fibers have been developed[3], and the transverse strength has been improved without significant degradation of the longitudinal strength. But the basic understanding of the crystal structure of the interface phases is still lacking.

The aim of the present work was to obtain crystallographic information about the interface reaction zone using electron diffraction in a Transmission Electron Microscope

(TEM). The corresponding interface chemistry on some specimens was studied using a Scanning Auger Microscope (SAM). Various composite materials with different transverse strengths were employed in order to correlate the structure of interface phase with mechanical properties.

Titanium diboride (TiB_2) was found in the interface layer for every material processed by the standard pretreatment coating. γ-Aluminum oxide (γ-Al_2O_3) phase was also observed in most materials studied here as were other oxides and carbides.

Experimental

The graphite/aluminum composite materials examined in this study are listed in Table 1 along with fiber type, transverse strength and the interface phases observed in TEM. Except for G3842 which is plate consolidated from T133 wire, the materials are all unconsolidated wires. The matrix material is 6061 Al. The single fiber wire in Table 1 is a single graphite fiber"prepreg" with no pretreatment coating on the interface. This composite wire is produced by the ion vapor deposition of an aluminum 4% Mg alloy on the fiber. Basically, two fiber types were examined in this study, each representing currently available commercial forms. One is a low modulus type II PAN fiber with the oriented graphite basal planes tending to be parallel to the fiber

surface just below it. The other is a high modulus pitch type fiber with basal planes roughly perpendicular to the fiber surface. All fibers have circular cross sections. See Figure 1 for the relative basal plane orientation.

To make the fiber-matrix interface accessible to observation, a selective etching method was used. The materials were dipped or swabbed in one of three different etchants: a concentrated HCl solution, an HCl solution diluted by 60-70% volume percent methanol, and a 7N KOH solution. The samples were then thoroughly rinsed with acetone, methanol or ultrasonically cleaned in methanol. Thus, the sample fibers were free of the aluminum matrix material and only some interface pieces still attached to the fiber surface were left. Searching along the fiber surfaces in the transmission electron microscope* revealed numerous interface pieces thin enough for transmission in the samples prepared in HCl solution diluted by methanol or in concentrated HCl solution and a few thin interface layers in the sample etched by KOH.

Both the composite wire and plate were fractured in situ in the Scanning Auger Microscope (SAM)** under 10^{-3} μPa vacuum

*A JEOL 150 KeV TEM was used in the transmission diffraction studies.

**The SAM instrument applied in these studies was the Physical Electronics model 590 system.

in order to unambiguously analyze the material in the fractured interface region between fiber and matrix. In addition, some of the samples were sputtered using 5kV argon ions and examined to identify the chemical species present. An electron beam spot size of appoximately 1μ or less was used to give good spatial resolution and high signal to noise ratio.

Results and Discussion

The most often observed phase was a TiB_2 hexagonal structure which was found in all the pretreated materials studied here. Some typical electron diffraction patterns of TiB_2 prepared in HCl plus methanol for various composite materials are shown in Figure 2. The observation of the spotty nature of the rings in the TiB_2 diffraction pattern from the T114A composite indicated that the grain size of TiB_2 in the T114A composite was larger than the grain size of TiB_2 in the other composites studied here. This grain size difference was consistently observed in many fibers and also in samples prepared by the other selective etchants: concentrated HCl and KOH. One basic difference between T114A and the rest of the composite materials is that the fiber in T114A has the graphite basal plane parallel to the fiber surface but the other composites have the pitch type fiber with basal plane perpendicular to the surface. This difference in

crystallographic orientation in the substrate may lead to a preferential growth of large grains for a TiB_2 reaction product in T114A. The grain size effect may play a role in the transverse properties of the composites.

In recent years it has been demonstrated that a high degree of preferred orientation of "fibrils" are formed in the graphite fiber of high tensile modulus and strength[4]. The "fibril" is a structural unit which is composed of "microfibrils" and pore structure[5,6]. Its dimensions have been estimated to be from 250Å to as high as 1000Å[7,8] in the transverse direction. The fibrils have indefinite length and may form a continuous or branched network. The "microfibril" is a stacking of graphite layers and the dimensions can be characterized by the stacking height (or the microfibril thickness) and the microfibril width and length.

A close investigation into the morphology of TiB_2 layer in electron micrographs for various composites showed some striated or ripple characteristics of this interface layer in pitch fiber reinforced materials (see Figure 3). These ripples are probably due to the "fibril" structure. The chemical vapor deposited TiB_2 covers the fiber surface as a surface replica. A rough estimation of the dimension across these strips gives values ranging from 200Å to 600Å which are in the range of fibril transverse dimension.

The micrographs of TiB_2 layer formed at the interface for low modulus PAN II composites are also shown in Figure 4. The comparison between pitch fiber and low modulus PAN II composites can be seen in Figure 3 and Figure 4, respectively, where the TiB_2 phase with crenulations or ripples for VSB-32 pitch type composites and without for PAN II type composites are presented. The diffraction pattern of Figure 3 (c,d) is shown in Figure 2 (b) and that of Figure 4 is shown in Figure 2(c).

An aluminum oxide (γ-Al_2O_3) phase was often observed along the fiber/matrix interface. The origin of the oxide has not been clearly established, but it is most likely the reaction product of oxygen which was contained in the fibers and then segregated to the interface during the aluminum-infiltration processing step. The exact role of this oxide layer is not known at present, but the recent SAM studies[9] indicate that it seems to promote matrix adhesion to the graphite which might be responsible for an increased transverse strength in graphite/aluminum composites. The present TEM examination of these oxide layers on the fiber surfaces indicated that the γ-Al_2O_3 phase has a relatively larger grain size on the average than that of TiB_2. The electron diffraction patterns of γ-Al_2O_3 (Fig. 5) were observed for the composites with an interface coating and the single fiber wire which had no coating on the interface.

It is also interesting to point out that titanium carbide, TiC, was observed in G3842 and G3636 composites. In both materials, the rings of diffraction pattern are continuous, however the diffraction ring is broadened to some extent in G3636 composite. This is believed to be due to the effect of very fine grain size. The diffraction pattern and micrograph for the TiC phase can be seen in Figure 7.

The Al_4C_3 phase which was determined[10] to be present at the interface in other research (Aerospace Corp.) could not be identified by the technique used here, because Al_4C_3 is decomposed in water and highly soluble in both acid and alkali solution. Recently Al_4C_3 as well as oxides other than Al_2O_3 have been observed using an electrochemical thinning technique. Further studies using this approach are now in progress.

The interface reaction zone in the composites studied in the TEM was also investigated by SAM combined with in situ fracture to help identify the interface chemistry. The fracture paths were through the oxide layer or close to either the fiber side or matrix side of the interfaces. The Auger chemical analysis versus the depth into the fracture surface was obtained using inert argon ion sputtering. Using sensitivity factors[11] estimation of the atomic concentration ratio of titanium to boron, Ti/B at selected points after

sputtering was consistently about 0.51-0.57 in the G3636 and G3842 materials (see Figures 8 and 9). A standard TiB_2 Auger spectra after sputtering of TiB_2 powder is shown in Fig. 10. The Ti/B ratio is ~.55. A lack of chemical shift in peak location and consistent peak to peak height analysis together with the assumptions that the escape depth correction, back scattering factor and surrounding chemical effect are negligible, support the TEM results that TiB_2 phase was present in the interface layer. Further studies are being conducted in the TEM and SAM to clarify and extend the results reported in this paper.

Conclusions

Results of this work can be summarized as follows:

1. TiB_2 phase is generally present for the aluminum/graphite composites processed by standard pretreatment coating technology.
2. Larger TiB_2 phase grain size was observed in PAN II fibers with the graphite basal plane perpendicular to the fiber surface. This could relate to higher transverse strength in composites with this fiber.
3. γ-Al_2O_3 phase was found in most composites and is relatively larger in grain size than the TiB_2 phase.

4. The mixture of γ-Al_2O_3 and TiB_2 was observed in some areas of interface for the composite with pitch fibers.
5. AES identified the existence of the approximately stoichiometric TiB_2 atomic concentration ratio, for many of the composites studied.

Acknowledgement

This research was sponsored by the Office of Naval Research, Contract N00014-78-C-0094 at The University of Texas at Austin.

References

1. Dull, D.L. and Amateau, M.F., "Transverse Strength Properties of Graphite-Aluminum Composites," Quarterly Progress Report No. 1, TOR-0077 (2726-03)-1, The Aerospace Corporation, El Segundo, CA (10 Jan, 1977).

2. Steckel, G.L., Flowers, R.H. and Amateau, M.F., "Transverse Strength Properties of Graphite-Aluminum Composites," Final Report for Period 1 Oct. 1977 - 30 Sept. 1978 for Naval Surface Weapons Center, TOR-0078 (3726-03)-4, Sept. 30, 1978.

3. Amateau, M.F., "Progress in the Development of Graphite-Aluminum Composites Using Liquid Infiltration Technology," Journal of Composite Materials, Vol. 10, Oct. 1976, p. 279.

4. Fourdeux, A., Herninckx, C., Perret, R. and Ruland, W., Comt. Rend. 269C, (1969), 1597.

5. Badami, D.V., Joiner, J.C. and Jones, G.A., Nature 215, (1967) 386.

6. Johnson, W. and Walt, Nature 215 (1967) 384.

7. Johnson, J.W., Rose, P.G. and Scott, G. in 3rd Conf. on Industrial Carbon and Graphite (1970), London, (pub. 1971), p. 443.

8. Bacon, R. and Silvagge, A.F., Carbon 9 (1971), 321.

9. Marcus, H.L., Dull, D.L. and Amateau, M.F., "Scanning Auger Analysis of Fracture Surfaces in Graphite-Aluminum Composites," in Failure Modes in Composites IV, J.A. Cornie and F.W. Crossman, eds. Conference Proceedings, The Metallurgical Society of AIME, Fall 1977.

10. Padlla, F., Harrigan, W.C., Jr., and Amateau, M.F., "Handbook of Test Methods for Evaluation and Qualification of Aluminum-Graphite Composite Materials," Material Sciences Laboratory, The Aerospace Corp., El Segundo, CA (21 Feb. 1975).

11. Davis, L.E., et al, Handbook of Auger Electron Spectroscopy, Published by Physical Electronics Industries, 2nd edition, 1976.

Table 1

Composite Materials	Graphite Fiber Type	*Transverse Strength MPa	**Phase(s) Observed in TEM
T114A	PAN II (Celion 6000)	76	TiB_2, γ-Al_2O_3
G3842 (made from T133)	Pitch (VSB-32)	31	TiB_2, γ-Al_2O_3, TiC
G3636 (made from T105A)	Pitch (VSB-32)	10	TiB_2, γ-Al_2O_3, TiC
T109B	Pitch (VSB-32)	not available	TiB_2
HM pitch/ 6061	HM 3000	14-80 depends on consolidation process	TiB_2
Single Fiber Wire	PAN II (Celion 12000)	not measured	γ-Al_2O_3

*Transverse Strength was tested in plate forms by Aerospace Corporation.

**Camera constant used here for d-space identification was about 1.37 Angstrom-cm.

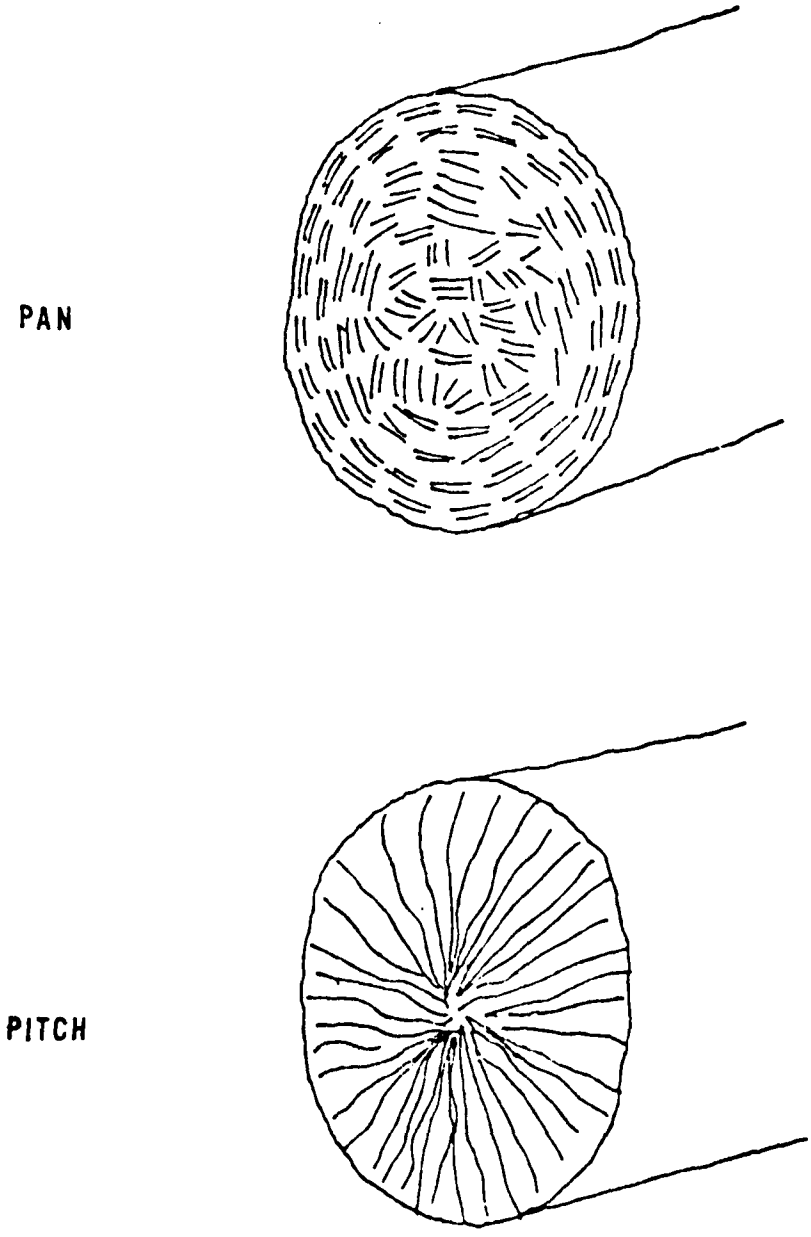

Fig. 1. Schematic diagram of oriented structure in PAN and Pitch type fibers.

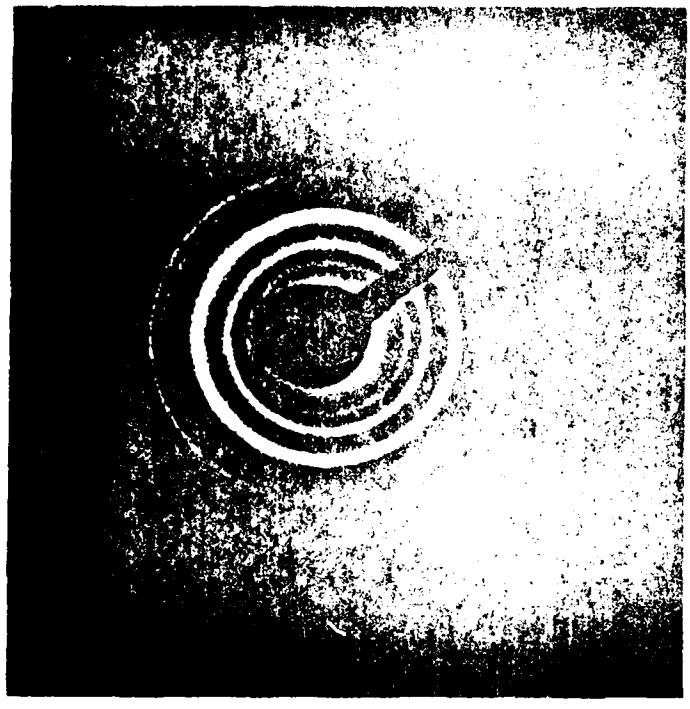

(a)

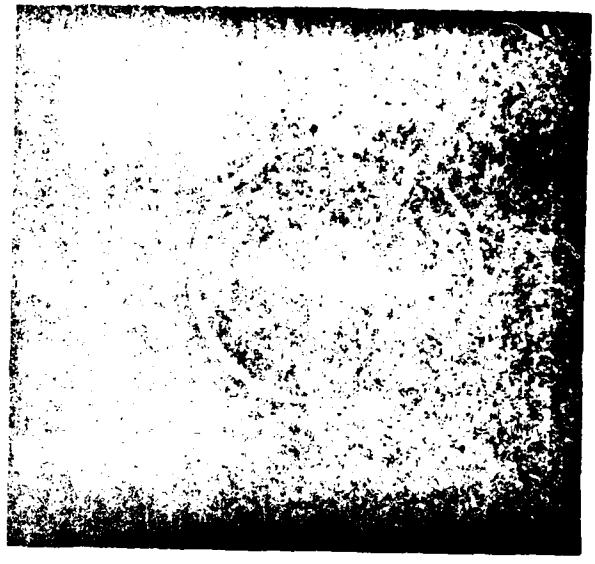

(b)

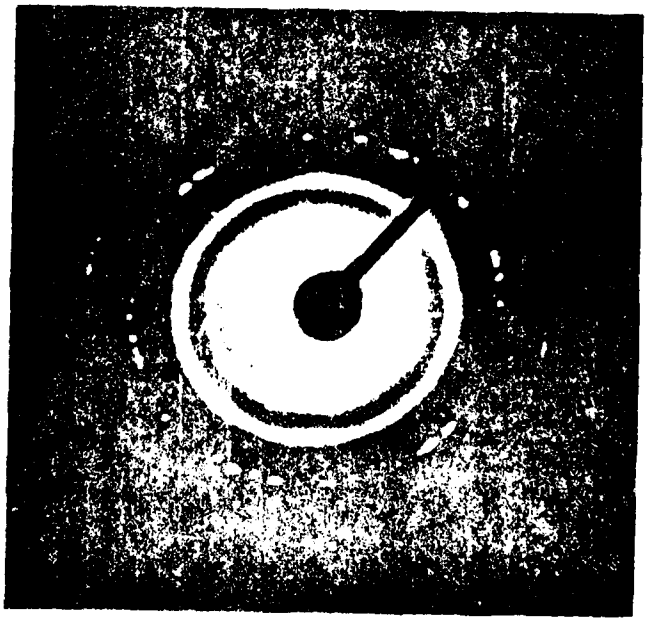

Fig. 2. Electron diffraction patterns for InAs in (a) [illegible], [illegible], and (b) TiI:V etched by HCl and [illegible].

(a)

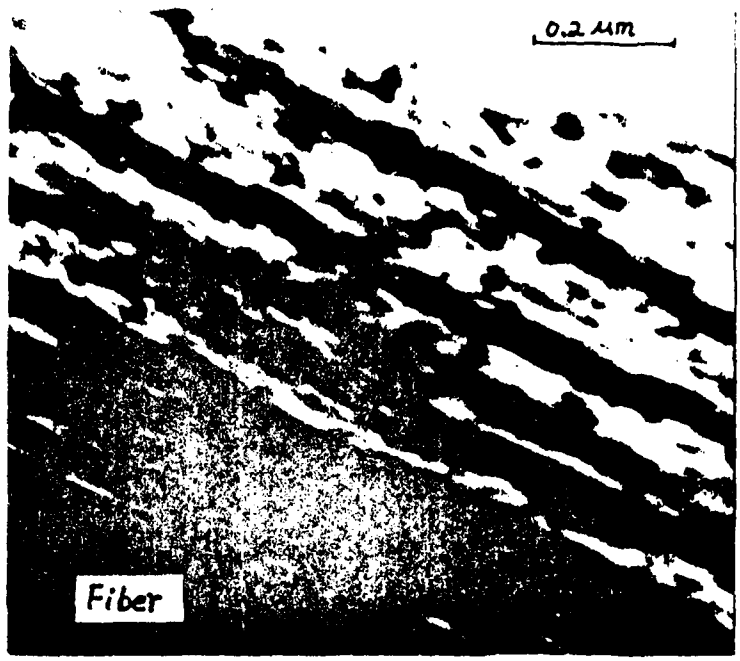

(b)

(c)

(d)

Fig. 3 Electron micrographs showing the crenulated TiB_2 layers in various pitch fiber type composites (a) T109 etched by HCl, (b) G50S, (c) and (d) G3842 etched by HCl and methanol.

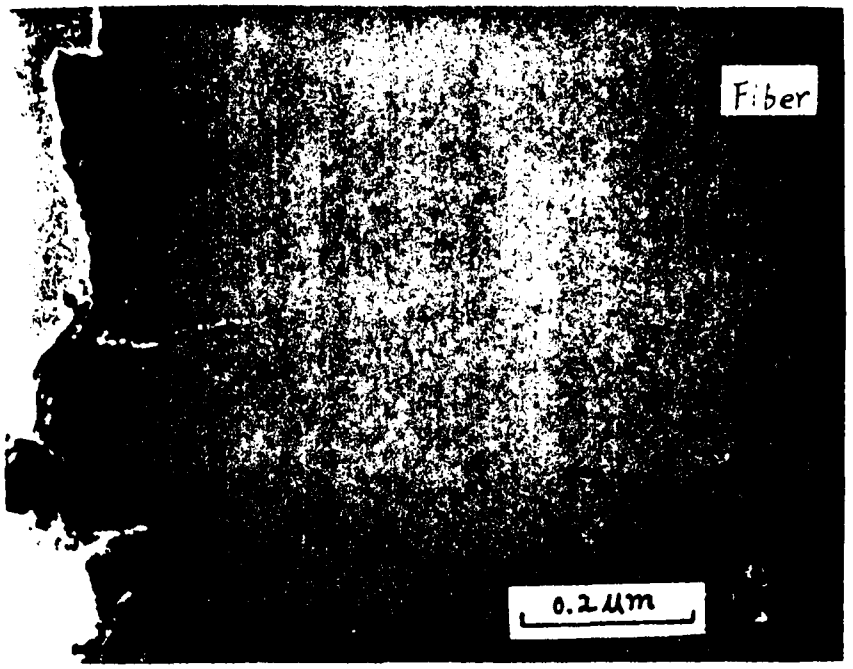

(a)

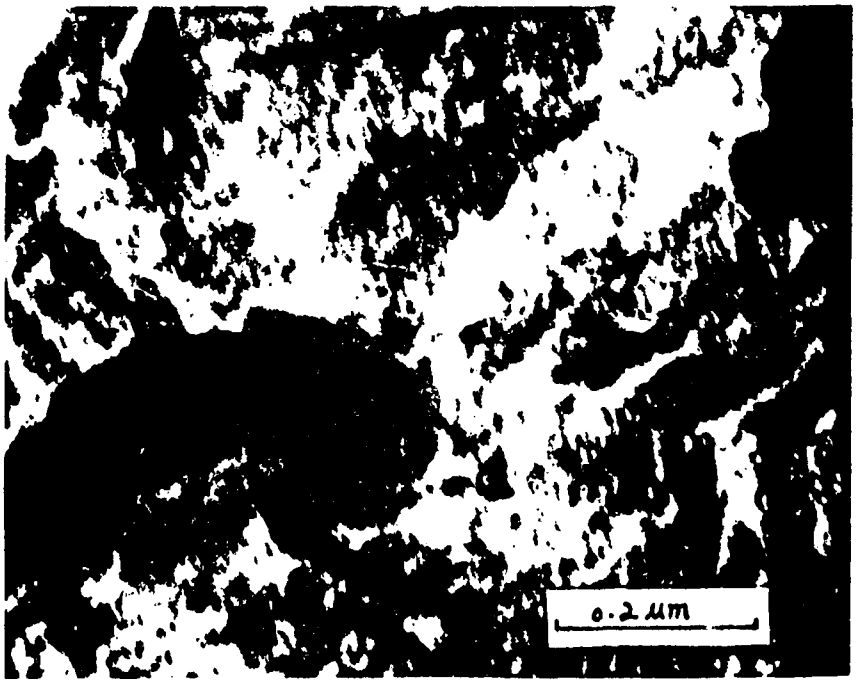

(b)

Fig. 4. Electron micrographs of larger grain size TiB_2 phase in Ti14V (a) sample etched by KOH, (b) sample etched by HCl and methanol.

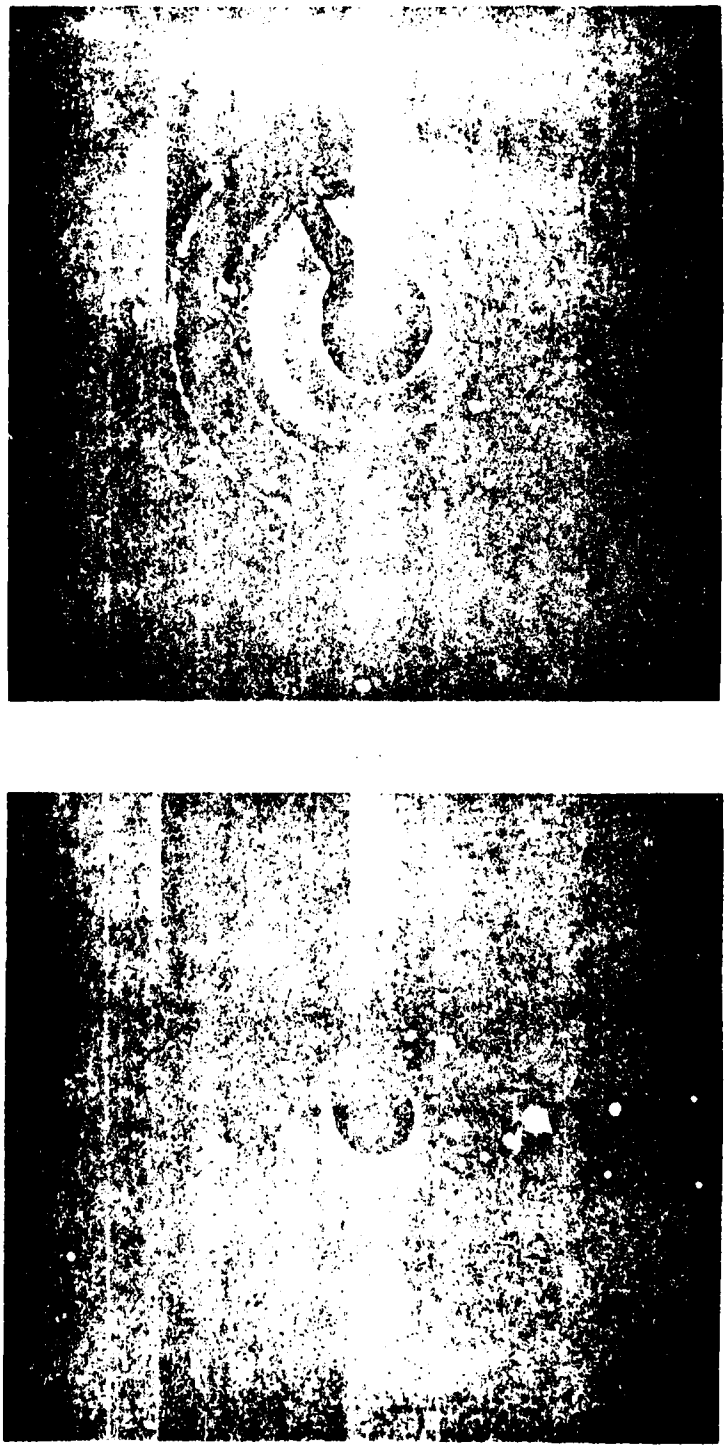

Fig. 5. Electron [illegible] Ti_3O_5 phase. (a) [illegible] etched by HCl and methanol. [illegible] and TiB_2 is also present in [illegible]

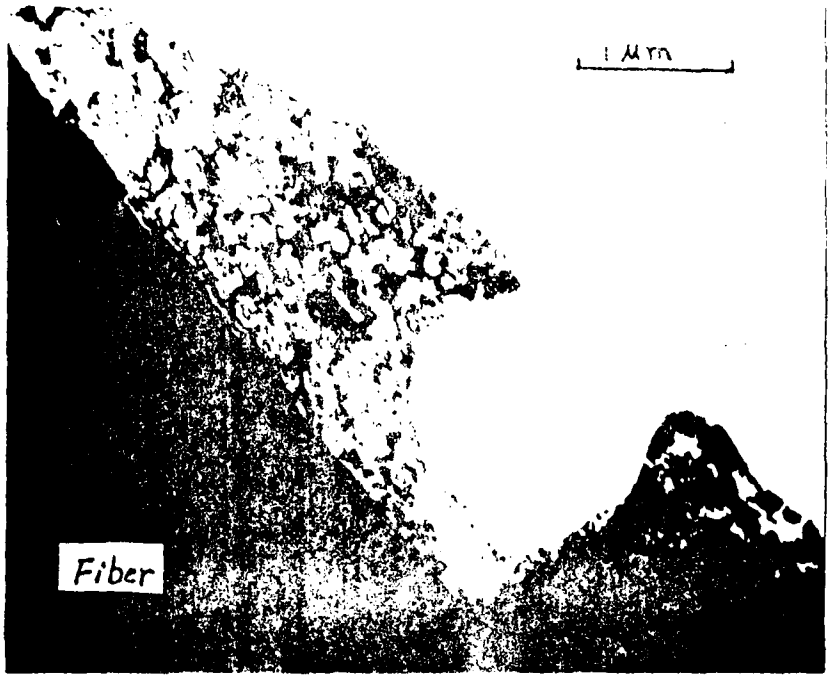

(a)

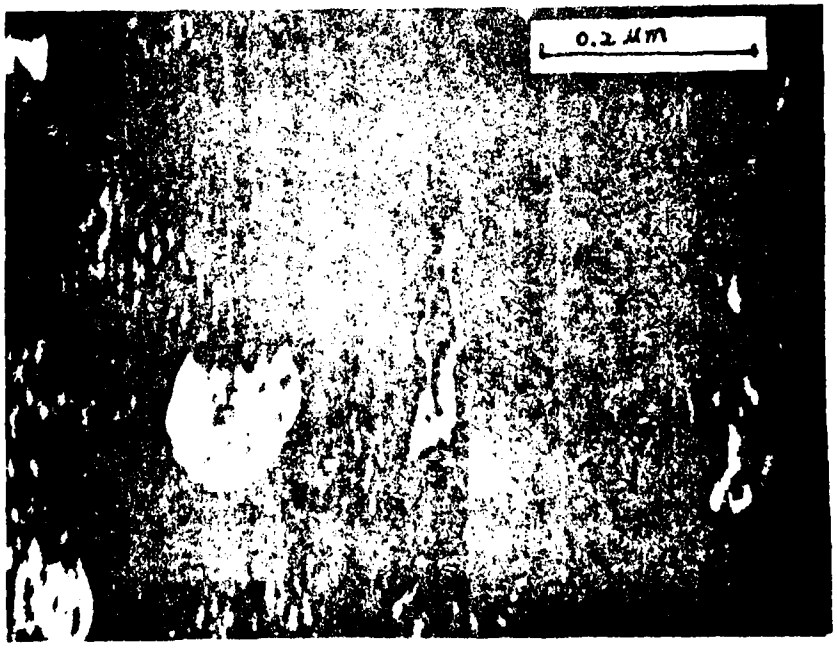

(b)

Fig. 6. Micrographs [illegible] of 1114A etched by HCl and methanol. [illegible] of whole piece, the dark part [illegible] High magnification of center area of [illegible] Note: Some larger grain [illegible] neck part of the whole piece [illegible]

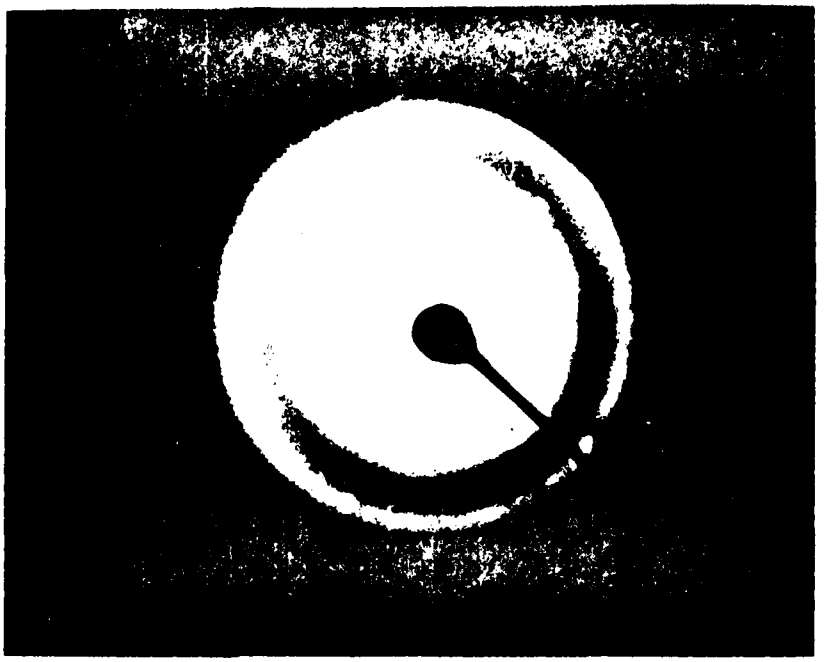

(a)

(b)

Fig. 7. The TiC phase in G5842 etched by KOH (a) a diffused electron diffraction pattern, (b) the micrograph of (a).

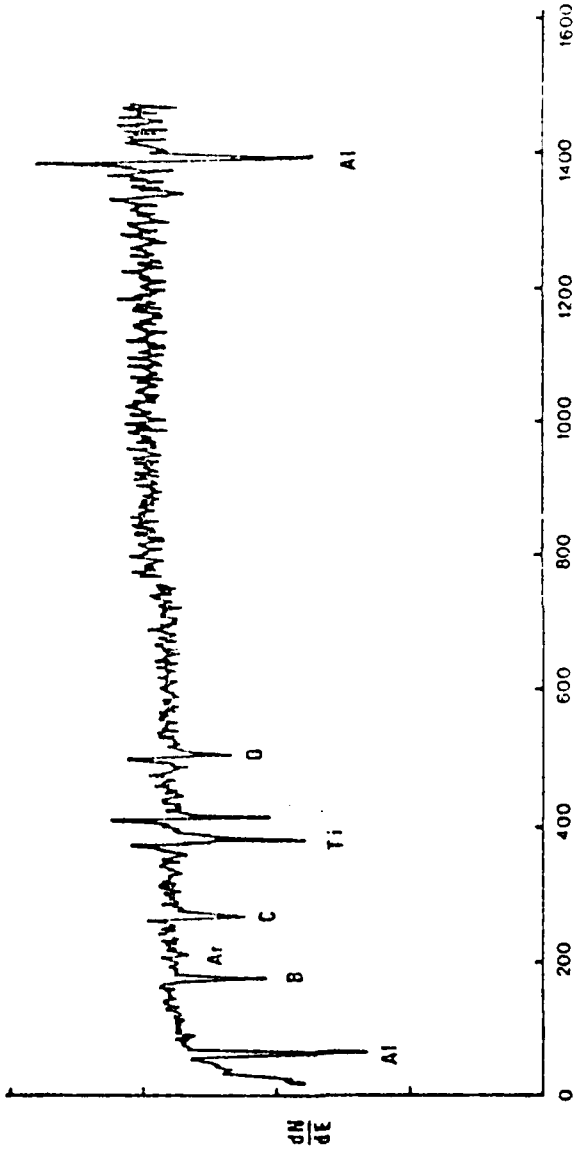

Fig. 8. AES analysis of the fractured interface after 25 minute sputtering in T105A (plate G3636 was used).

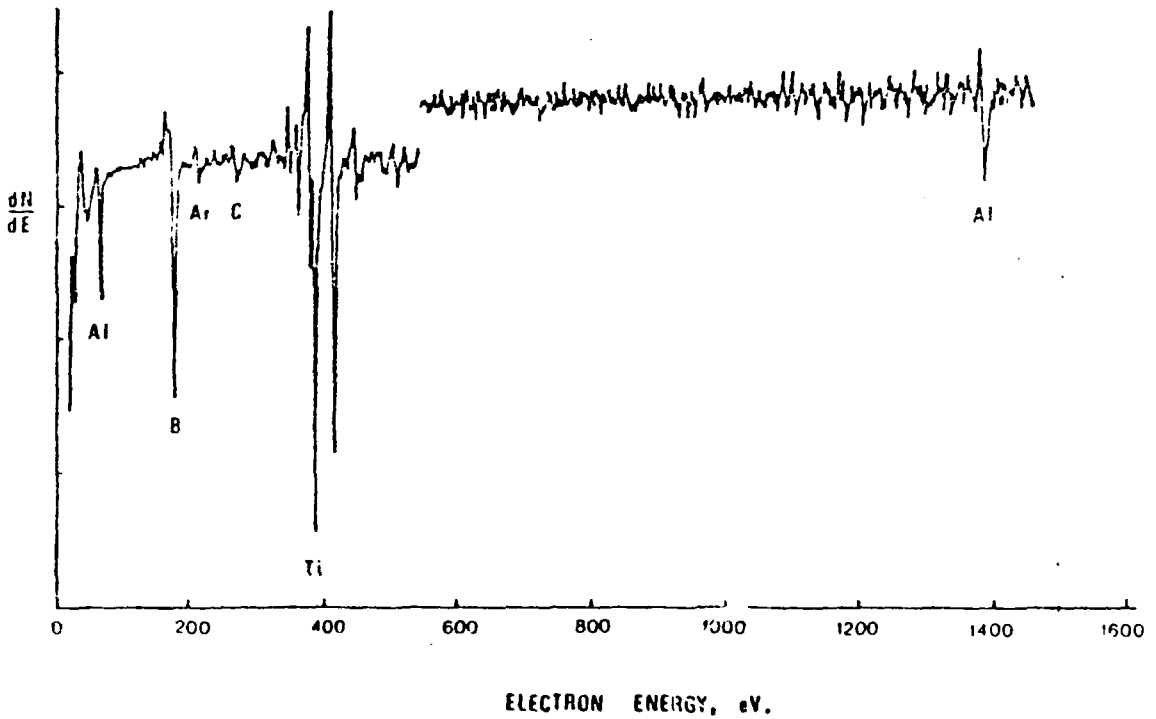

Fig. 9. AES analysis of the fractured interface after 5 minute sputtering in G3842.

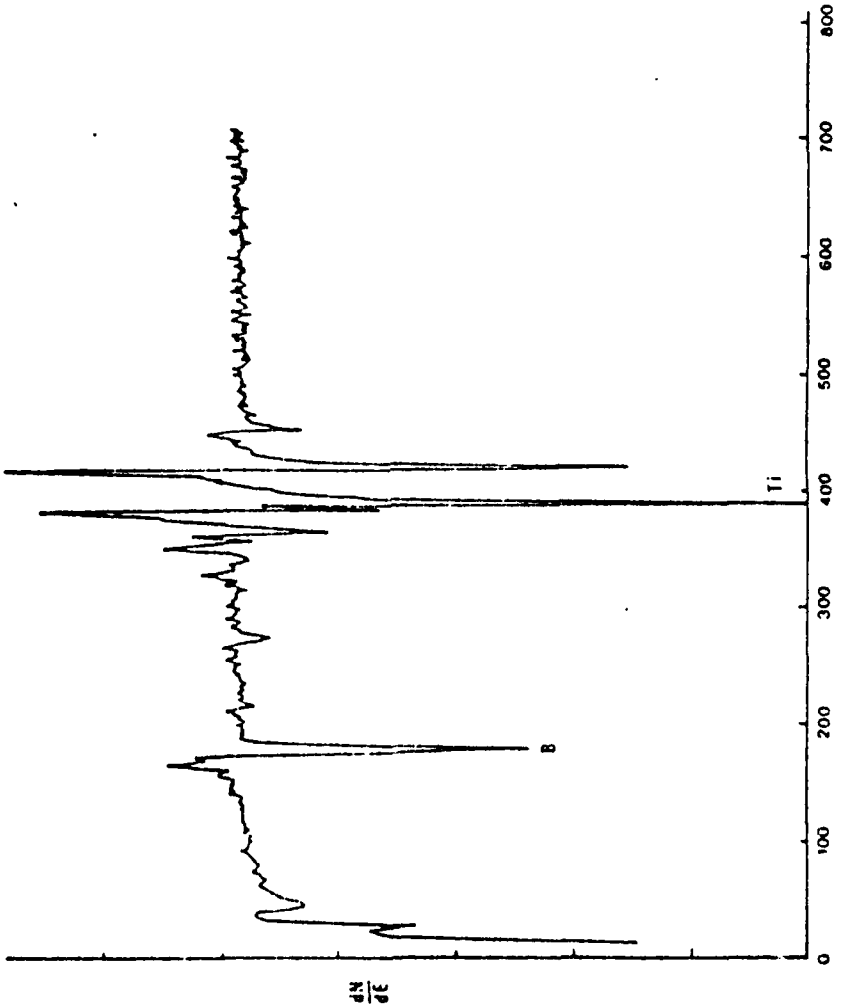

Fig. 10. Standard TiB_2 SAM spectra after sputtering.

Appendix E

THIN FILM ALUMINUM CARBIDE FORMATION

In commercial Gr/Al composites, the early stages of solid state aluminum carbide formation are believed to be interface controlled. A simple layer growth model is inappropriate for the early stages since coarsening of the fine network is such a slow process (i.e., a several day aging period is required to develop the network into a structure which can be approximated by an annular layer between the interfacial oxide and the matrix). However, the later stages associated with continued growth of Al_4C_3 are diffusion controlled with the carbon diffusing into the aluminum, in the absence of an interfacial oxide layer, forming crystalline Al_4C_3 platelets [1].

Investigation of the Al_4C_3 nucleation and growth kinetics through AES studies with large grained polycrystalline graphite substrate/adsorbate systems subjected to heat treatment has been addressed previously. Additional AES data are presented in this appendix concerning heat treatment of glassy carbon/γ-Al_2O_3/Al thin layer composites which may have implications for the early stages of Al_4C_3 formation in all Gr/Al systems.

Heat treatment of glassy carbon/γ-Al_2O_3/Al thin layer composites of approximately 25 nm interfacial oxide thickness was performed using a bell jar vacuum system. Each specimen was aged in an inverted position with the back side of the substrate in contact with the thermocouple to avoid scratching the thin film. (The metal overlayer was intentionally deposited to less than 100 nm

thickness to optimize the layer definition during depth profiling.) Aging times ranged from five to sixty minutes. Aging temperatures used were from 450°C to 640°C. The vacuum quality was held constant at $5x10^{-6}$ Torr ($6.5x10^{-4}$ Pa) during heat treatment.

Only a slight amount of Al_4C_3 was detected in the glassy carbon/γ-Al_2O_3/Al thin layer composite subjected to heat treatment at 500°C for 30 minutes. Comparison of sputtering profiles for specimens aged for 30 minutes and 60 minutes at 500°C (see Figs. 1 and 2-a) indicates that Al_4C_3 forms throughout the composite as heat treatment progresses but is most prominent adjacent to the glassy carbon (see Fig. 2-b). Broadening of the interfacial and surface oxide layers is evident following heat treatment. The oxide broadening becomes worse at higher temperatures (see Fig. 3) and it seems to be associated with the rate of Al_4C_3 formation.

Effective layer thicknesses of similar Al_4C_3 concentration were determined for specimens subjected to different heat treatments, and they are tabulated with the equilibrium reaction rates (see Table E-1). These determinations are based on differences in normalized area beneath carbon profiles from depth profiling data for aged and as prepared specimens. It is estimated that an activation energy of 200 kJ/mol (see Fig. 4) is associated with the early stages of solid state Al_4C_3 formation in the thin layer composites.

The presence of Al_4C_3 throughout the adsorbed layers of the heat treated thin layer composites and the rather typical activation energy associated with the early stages of the kinetic process indicate that transport of carbon and aluminum atoms occurred

readily throughout the thin films. The apparent decomposition of the interfacial oxide and the lack of buffering provided by the Al metal overlayer require additional investigation. Furthermore, the prominence of Al_4C_3 along the glassy carbon/oxide interface is in contrast to the result of long term heat treatment of commercial Gr/Al which produced Al_4C_3 mainly along the matrix/oxide interface.

It must be emphasized that application of ideal bulk diffusion-controlled reaction rate theory to the complex reaction layer is highly speculative. It is likely that aluminum carbide and oxycarbide protrusions form in the early stages despite the fact that the substrate material is nearly amorphous. In addition, thin layer transport through the interfacial oxide plays a major role in the initial stages, while bulk diffusion through the aluminum carbide is expected to take precedence later following relatively extensive carbide layer thickening. Nevertheless, the crude analysis does give an indication of the rates involved, and the activation energy determined compares favorably with that reported in the literature [1] concerning thick Al_4C_3 layer growth without an intermediate oxide layer.

Reference

1. I.H. Kahn, Met. Trans. 7A (1976) 1281.

Table E-1

RESULTS OF THIN FILM ALUMINUM CARBIDE FORMATION

Heat treatment	Effective reaction layer thickness(nm)	Equilibrium reaction rate ($cm/sec^{\frac{1}{2}}$)
450°C - 45min	5	
500°C - 30min	5	
500°C - 60min	25	4.7×10^{-8}
550°C - 10min	10	
550°C - 15min	20	
550°C - 20min	50	1.7×10^{-7}
600°C - 5min	50	2.9×10^{-7}
640°C - 5min	>50	

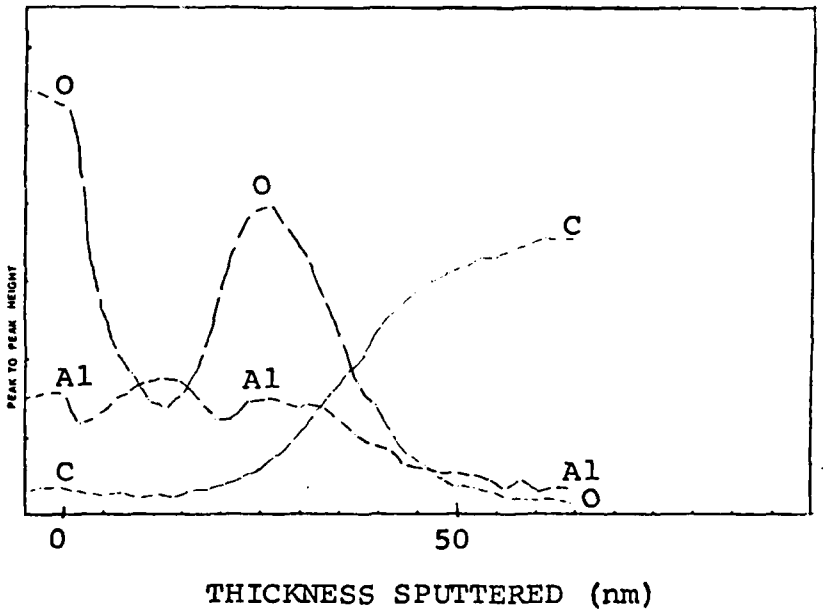

Fig. 1. AES sputtering profile for thin layer composite subjected to heat treatment at 500°C for 30 minutes.

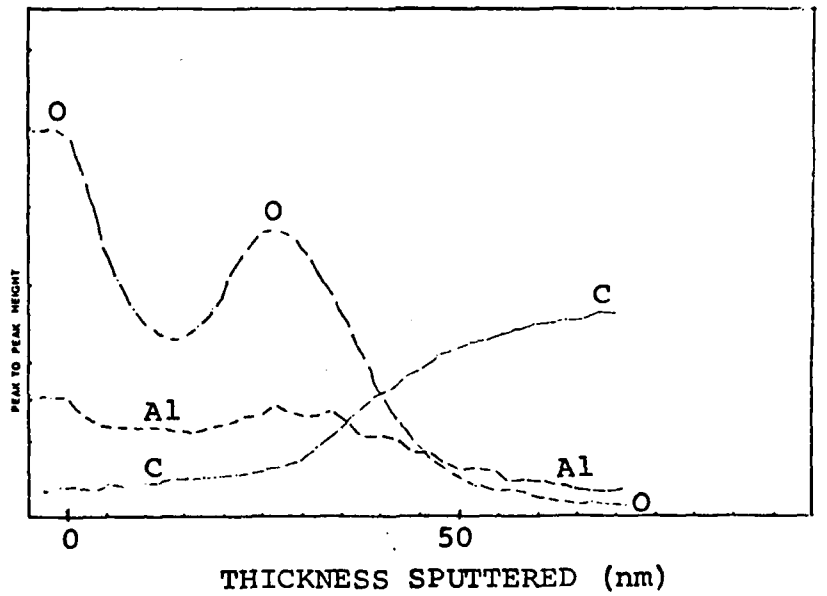

Fig. 2(a). AES sputtering profile for thin layer composite subjected to heat treatment at 500°C for 60 minutes. The carbide signal manifests itself as a slow initial rise in carbon signal followed by a steeper increase adjacent to the substrate.

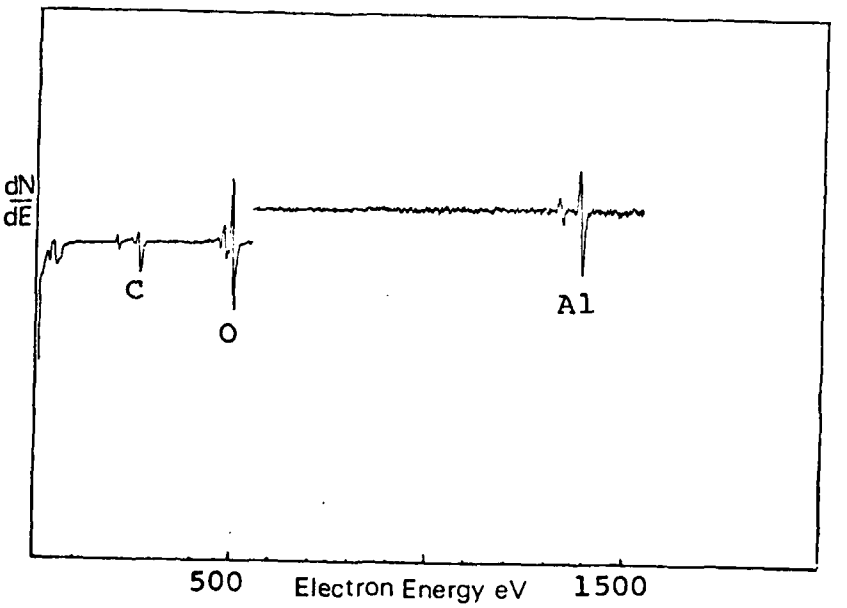

Fig. 2(b). Auger spectrum for thin layer composite heat treated at 500°C for 60 minutes, sputtered to a depth of 35 nm.

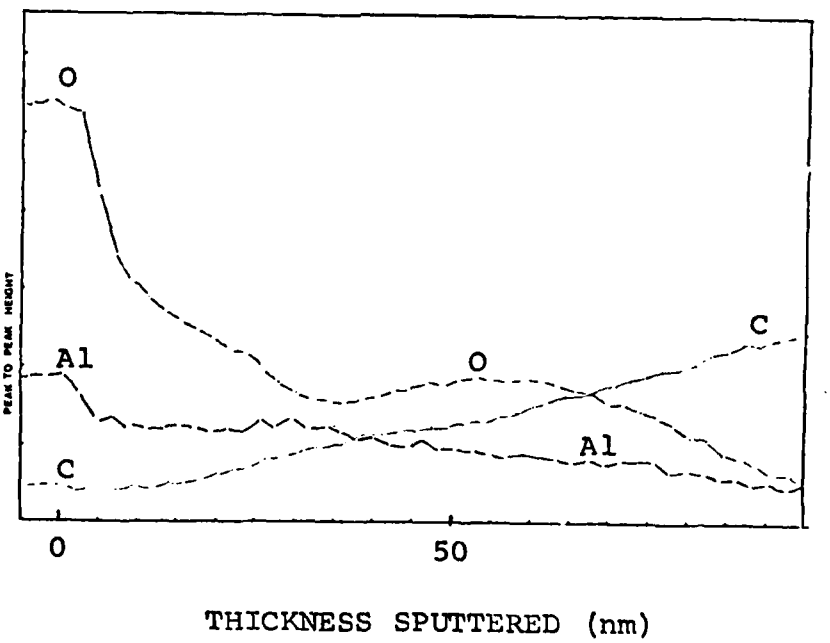

Fig. 3. AES sputtering profile for thin layer composite subjected to heat treatment at 550°C for 15 minutes.

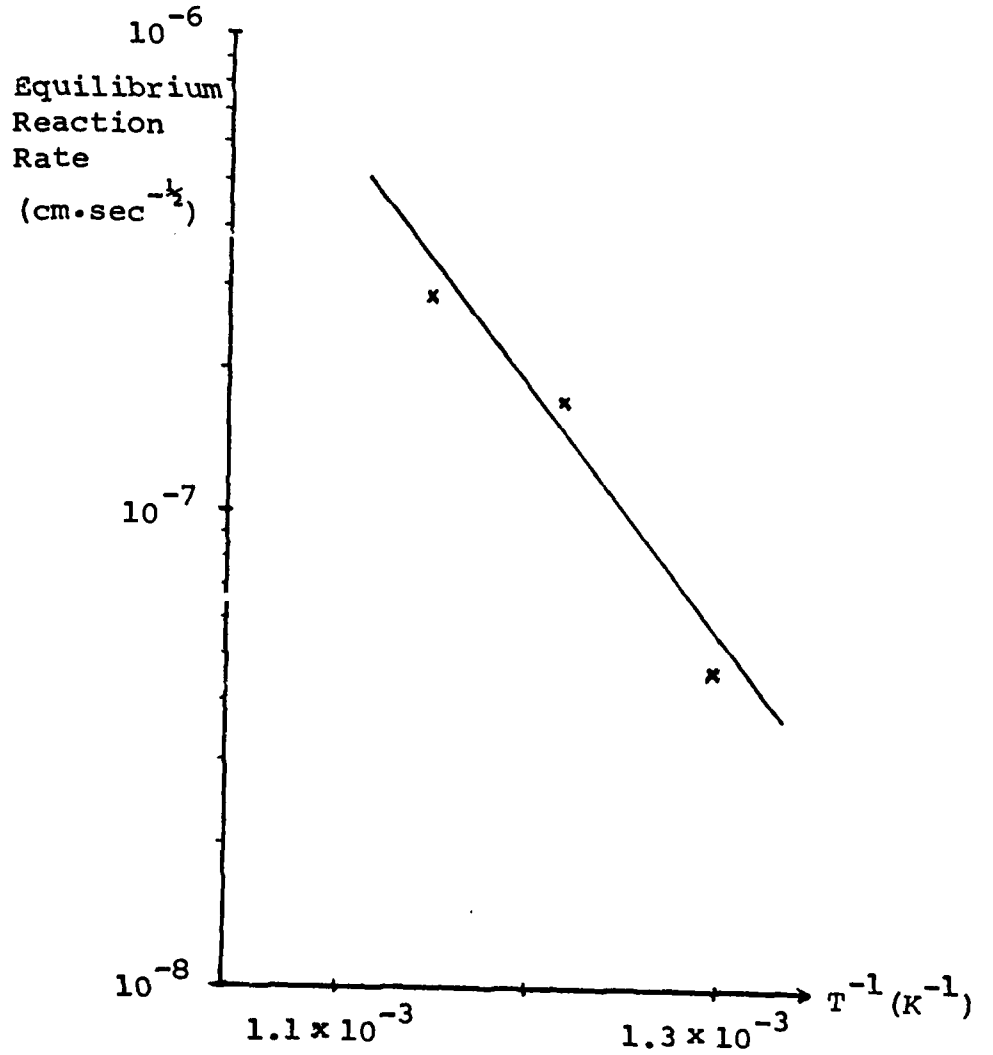

Fig. 4. Temperature dependence of the equilibrium reaction rate for aluminum carbide reaction layer formation in glassy carbon/γ-alumina/Al thin layer composites with 25 nm interfacial oxide thickness.

Appendix F

ALUMINUM CARBIDE FORMATION IN THE GR/AL SYSTEM

This appendix deals primarily with the study of solid state aluminum carbide (Al_4C_3) formation in Gr/Al composites. For temperatures above the solidus temperature of the aluminum alloy matrix, the Al_4C_3 reaction rate proceeds quickly in a manner which is severely detrimental to the graphite fibers. This is one reason why diffusion bonding parameters have a critical influence upon the maximum strength of commercial composite material [1]. Within the solid state, at elevated temperatures below the matrix solidus point, the Al_4C_3 reaction rate depends heavily upon environment of the specimen during thermal exposure, composition and thickness of the composite interface, and graphite crystal orientation.

For the model systems in this study, single crystal graphite, polycrystalline graphite, or glassy carbon serves as the substrate component of the Gr/Al system, while vacuum deposited thin films of alumina and aluminum comprise the remainder of the thin layer composite. For thermal treatment, accurate temperature control was used to avoid reaching the melting temperatures. The solidus for the 6061 Al alloy is 584°C and pure Al metal melts at 660°C.

For proper temperature regulation, thermocouples were put in direct contact with the specimens being heat treated in both the rough

vacuum environment in a mechanically rough-pumped furnace tube and in an insulated electric heater in a diffusion pumped bell jar with a vacuum of $2x10^{-6}$ Torr ($2.66x10^{-1}$ mPa). A high vacuum ion-pumped system facilitated encapsulation of some specimens in an inert environment of 10^{-7} Torr ($1.33x10^{-2}$ mPa) pressure using either vycor or quartz glass envelopes for an alternative form of heat treatment.

Commercial Gr/Al composites and thin layer composites were subjected to various kinds of heat treatment. Gas chromatography and Auger electron spectroscopy (AES) in conjunction with inert ion sputtering were used in this investigation to gain information regarding the extent of Al_4C_3 formation in the heat treated composites.

As mentioned before the external environmental influence upon Al_4C_3 formation must not be overlooked. It certainly matters whether specimens are heat treated in an inert, encapsulated environment, a vacuum oil-pumped reducing environment, or an oxidizing environment.

Al_4C_3 production is influenced by the mixture of gases which the Gr/Al composite material is exposed to during heat treatment within the solid state. The primary cause of this effect is diffusion down the fiber/matrix interface during the heat treatment. Extensive heat treatment at 550°C in either the encapsulated "high vacuum" condition or in an air furnace results in little or no Al_4C_3 formation. This is apparently due to a lack of available hydrogen and active hydrocarbons in the encapsulated high vacuum condition, while an excess of oxygen and water vapor induces dominant alternative oxidation

reactions at the interface in the air furnace condition. However, solid state heat treatment in oil-pumped rough vacuum systems promotes Al_4C_3 formation at the interface.

AES data reveal that internal Al_4C_3 formation was induced in many polycrystalline Gr/Al thin layer composites heat treated in the solid state regime in a diffusion pumped bell jar vacuum system. For example, results shown in Fig. 1(a-e) represent a 550°C, one hour heat treatment of a polycrystalline Gr/Al thin layer composite with no interfacial oxide deposited. The presence of Al_4C_3 is clearly indicated by Fig. 1(d). Fig. 1 includes the measured depth profile (a), along with important corresponding spectra (b-e) which show details of native oxide, Al metal, Al_4C_3, and graphite substrate. However, interpretation of the data in terms of layer thickness is not straightforward since the measured profile transitions between metal, carbide, and graphite are not steplike or well-defined. This is attributed to the nonuniform metallographic polishing characteristics of polycrystalline graphite as a substrate material and the resulting need to deposit thick overlayers to prevent a large percentage of the total film surface from being converted completely to Al_4C_3 before heat treatment has been completed.

A nonuniform adsorption problem is characteristic of ordinary polycrystalline graphite. Film quality becomes intolerably poor with deposited film thicknesses within the submicron range. Practically complete conversion of a submicron Al film to Al_4C_3 resulted from a 550°C, half-hour bell jar type vacuum heat treatment of a

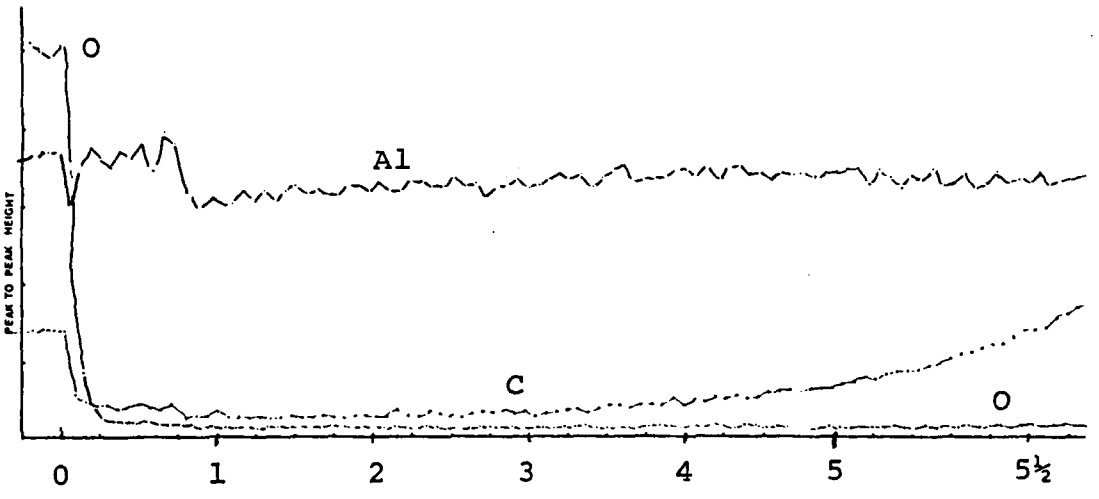

THICKNESS SPUTTERED (MICRONS)

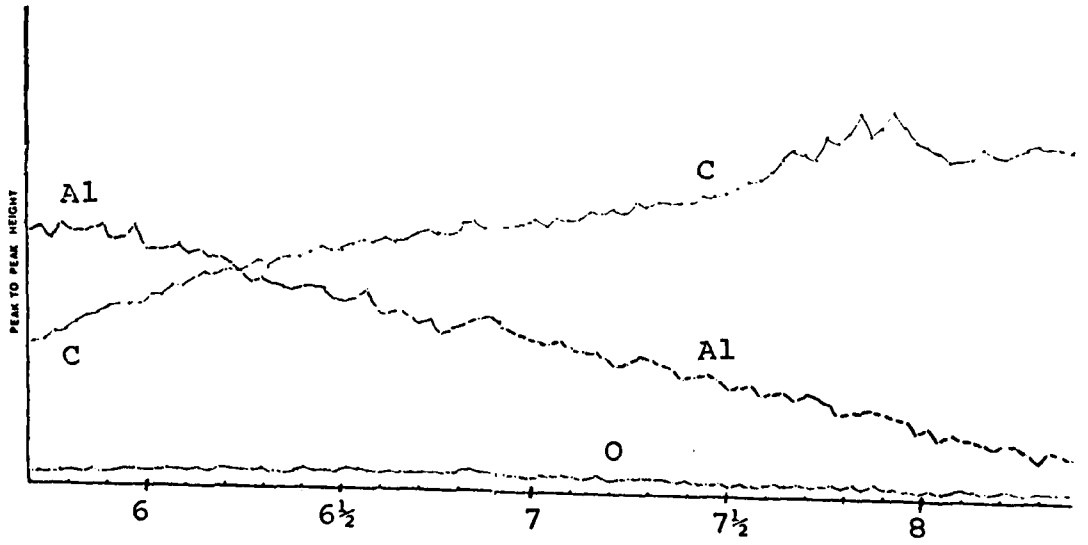

THICKNESS SPUTTERED (MICRONS)
(continued)

FIGURE 1a

Sputtering profile of polycrystalline graphite/aluminum thin layer composite aged 1 hr at 550°C.

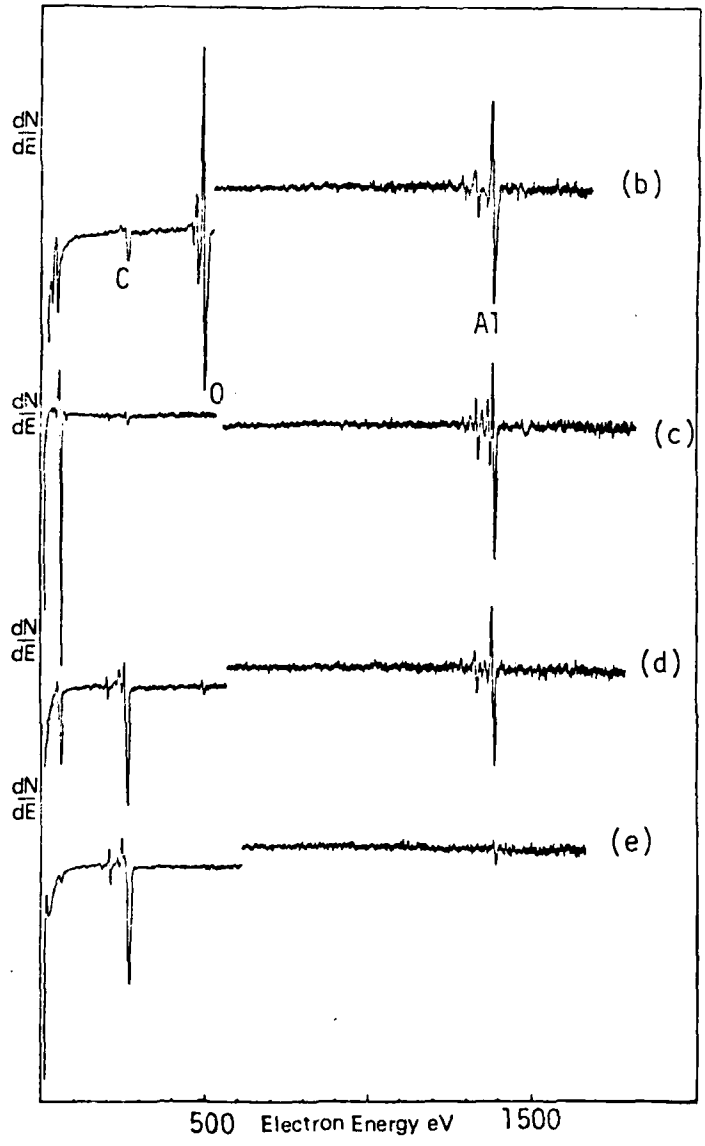

FIGURE 1(b-e)

Corresponding Auger spectra for aged polycrystalline Gr/Al at four stages of sputtering, showing surface oxide (b), pure aluminum metal (c), aluminum carbide (d) and graphite substrate (e).

polycrystalline Gr/Al thin layer composite having no interfacial oxide deposited (see Fig. 2(a-d)). Notice that there is an obvious presence of the carbide along the composite surface in the initial heat treated state judging from Fig. 2(b). The composite had evidently reacted completely during thermal treatment since no Al metal overlayer remained. It would be incorrect to deduce that the Al_4C_3 reaction zone extends as a dispersion into the bulk substrate. The data actually suggest quite the contrary.

Since polycrystalline graphite was used as the substrate, it is doubtless that microscopic nucleation irregularities and nonuniform layer growth occurred during deposition. Suppose for simplicity, that sputter removal of surface atoms followed a layer-by-layer mechanism. Then depth profiling would have some subtle complications. Any microscopic defects which were once unfavorable for nucleation during deposition would be first to become exposed during sputter-etching. Therefore, one might often expect to see carbide and graphite peaks superimposed (as in Fig. 2(c)) and sluggish transitions in depth profiles, such as those apparent in Figs. 1(a) and 2(a), due to unavoidable contributions obtained simultaneously from reaction layer and polycrystalline graphite substrate.

Fig. 3(a-e) indicates that an encapsulated high vacuum heat treatment does not promote Al_4C_3 formation like a bell jar type vacuum heat treatment for the same temperature and duration. Fig. 1(d) and Fig. 3(d), spectra taken when the C/Al signal ratio was 3:2 for each of the sputtering profiles (Figs. 1(a) and 3(a)), each show carbon

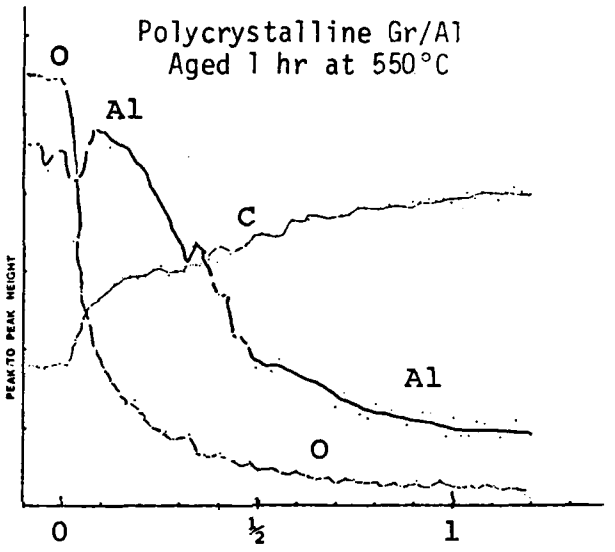

FIGURE 2(a)

Sputtering profile of polycrystalline Gr/Al thin layer composite aged 1 hr at 550°C. The heat treatment resulted in complete conversion of the submicron aluminum metal film to aluminum carbide.

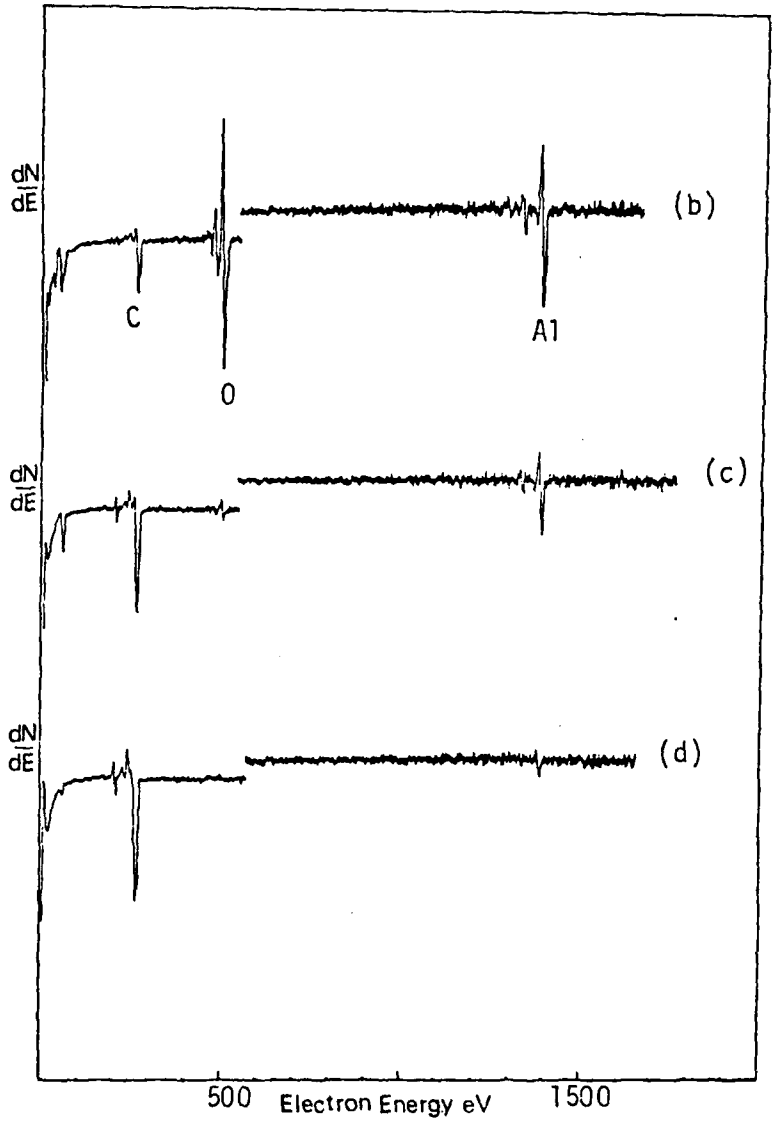

FIGURE 2(b-d)

Corresponding Auger spectra at three stages of sputtering, showing surface oxide and carbide (b), mixture of aluminum carbide and graphite (c) and graphite substrate (d).

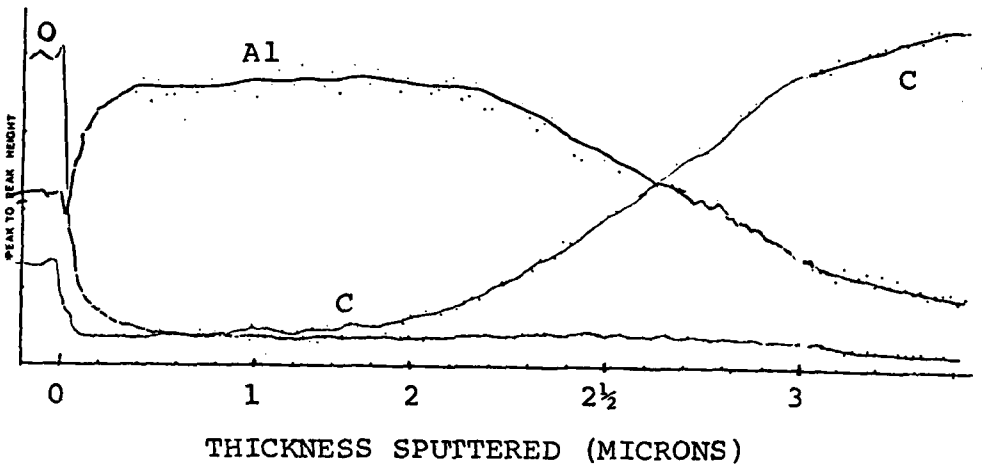

FIGURE 3(a)

Sputtering profile of polycrystalline Gr/Al thin layer composite subjected to encapsulated high vacuum aging for 1 hr at 550°C.

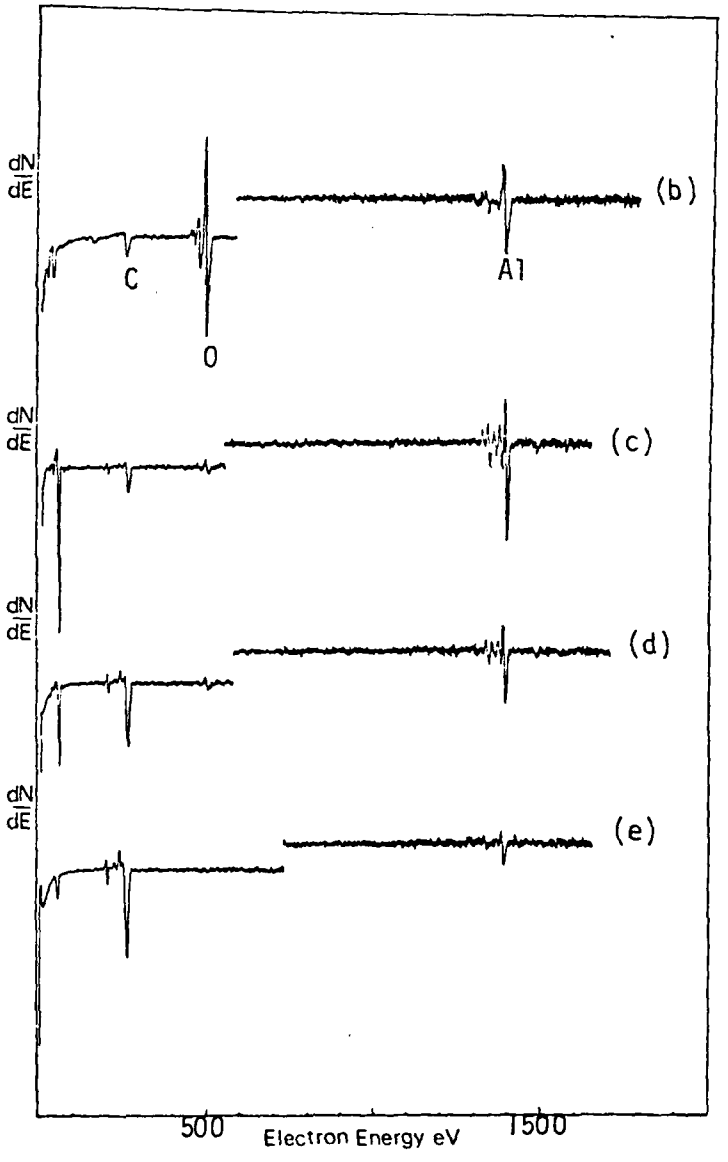

FIGURE 3(b-e)

Corresponding Auger spectra at four stages of sputtering, exhibiting the absence of aluminum carbide. Surface oxide (b), aluminum metal (c), mixture of aluminum and graphite (d), and graphite substrate (e) are illustrated.

and aluminum peaks with approximately the same peak-to-peak height. Yet the spectrum representing the encapsulated high vacuum 550°C, one hour thermal exposure (Fig. 3(d)) shows that the carbon and aluminum have not reacted extensively to form aluminum carbide. Neither composite specimen heat treated had an intermediate oxide layer present to retard the reaction rate. Both specimens had polycrystalline graphite substrates with pure aluminum overlayers. However, the extent of Al_4C_3 formation was clearly different for each, and the difference was somehow related to the diffusion pumped vacuum environment in the bell jar system.

A polycrystalline Gr/Al composite with a 100 nanometer thick interfacial aluminum oxide layer was heat treated in the bell jar vacuum system, again using 550°C temperature for a one hour period. The results (see Fig. 4(a-d)) show that Al_4C_3 still forms despite the presence of the oxide barrier, yet the complexities of the analysis prevent one from readily understanding the kinetics of this experiment. The spectra of Fig. 4 suggest that Al_4C_3 might be distributed throughout the composite, even within the oxide itself, but this is quite misleading. It is only an artificial effect introduced by use of polycrystalline graphite substrates. Heat treatments with commercial Gr/Al composites show that matrix sputtering profiles of in situ fractured material indicate that Al_4C_3 forms between the magnesium-aluminum oxide layer and the 6061 Al alloy matrix (see Fig. 5).

Use of carbon substrate material of better quality than ordinary polycrystalline graphite would facilitate a simplified kinetic

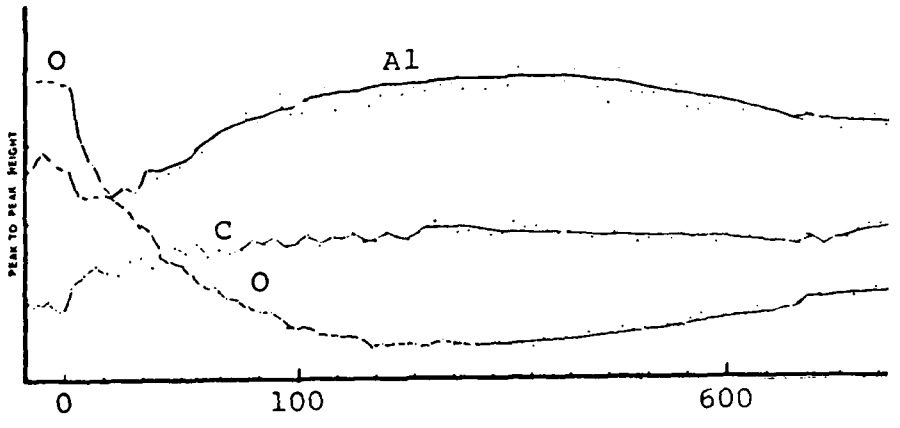

THICKNESS SPUTTERED (nm)

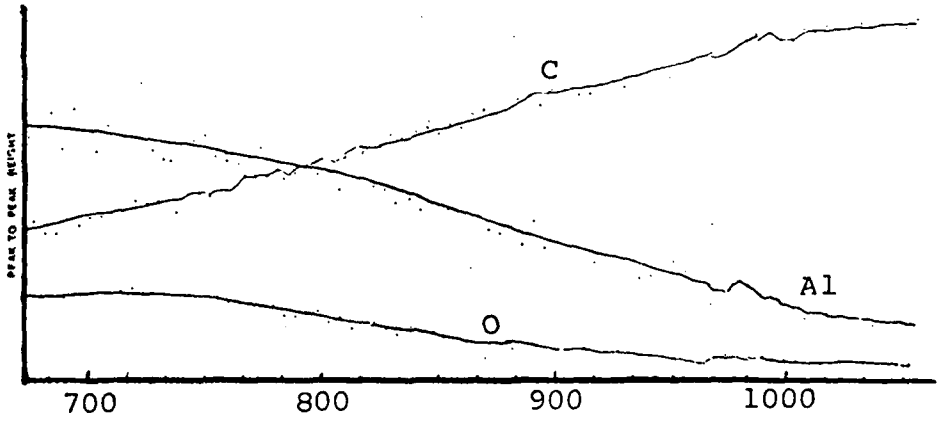

THICKNESS SPUTTERED (nm)
(continued)

FIGURE 4(a)

Sputtering profile of aged polycrystalline Gr/Al thin layer composite with intermediate oxide. Heat treatment was at 550°C for 1 hr.

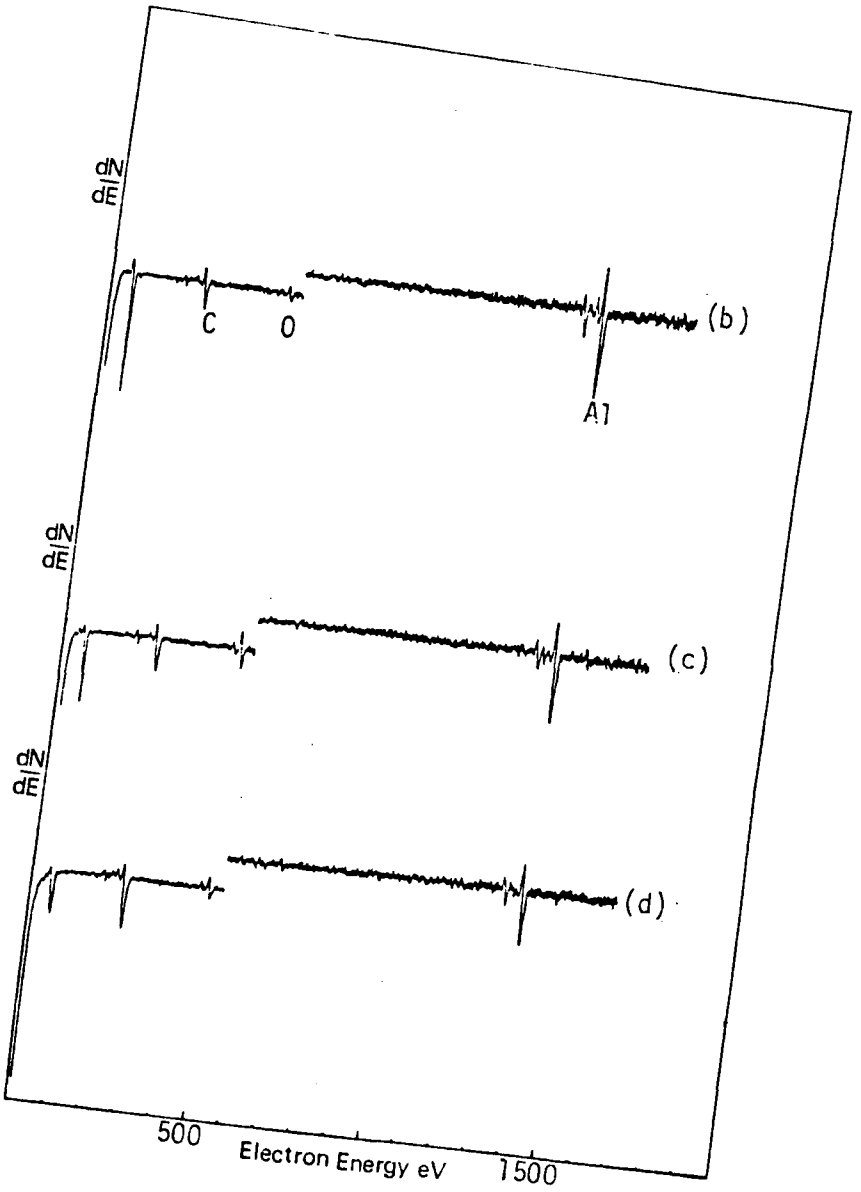

FIGURE 4(b-d)

Corresponding Auger spectra at three stages of sputtering, with aluminum carbide signal contributing to the total signal before (b), during (c), and after (d) the intermediate oxide layer signal has reached its maximum.

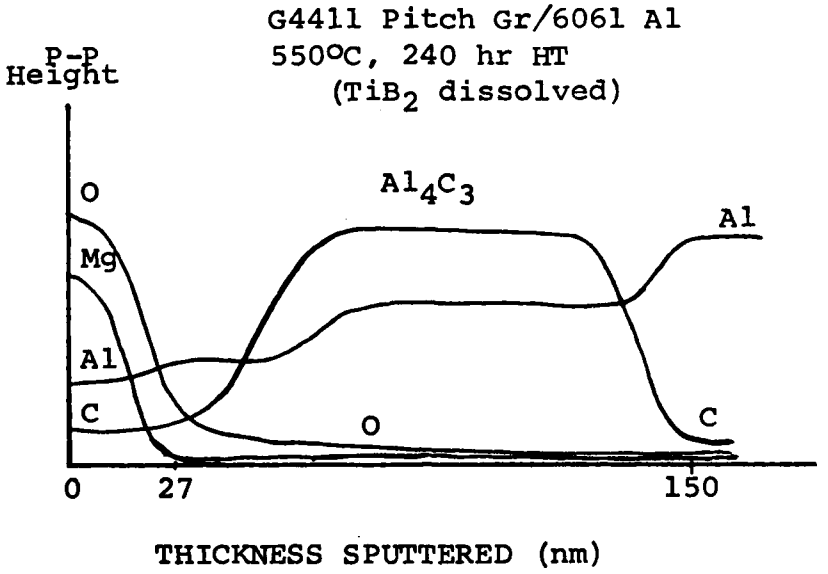

Fig. 5 High spatial resolution AES sputtering profile of aged commercial Gr/Al composite material fractured in situ and sputtered into the matrix. Aluminum carbide was found between the interfacial oxide and the bulk matrix, which suggests that carbon atoms diffuse from the graphite fiber through the oxide layer in order to react with aluminum atoms and form Al_4C_3.

experimental analysis. Natural single crystal graphite basal plane surfaces are of high quality. But graphite basal plane surface reactivity with aluminum appears to be very low. After the standard 550°C, one hour heat treatment in the bell jar vacuum system, any amount of Al_4C_3 formed in a single crystal Gr/Al thin layer composite was undetectable (see Fig. 6(a-f)).

Glassy carbon is by far the most suitable substrate material for Gr/Al kinetic analysis. Glassy carbon can be polished uniformly and it has the ability to react with aluminum in the solid state at a convenient rate. Experiments for kinetic analysis hinge upon optimization of the multilayer configuration (see Fig. 7) and application of a set of heat treatments which avoid complete conversion of the Al metal overlayer to Al_4C_3. It has been found that with an interfacial oxide thickness of 20 nanometers between a polished glassy carbon substrate and a 50 nanometer thick Al overlayer, only about twenty minutes elapsed before 550°C heat treatment in the bell jar vacuum system resulted in complete Al_4C_3 reaction of the Al film. Further experiments over a variety of temperatures with glassy carbon/aluminum composites having a variety of interfacial oxide thicknesses should lead to a better knowledge of the kinetics of the Gr/Al system. Results from several such experiments are presented in Appendix E.

In summary, Al_4C_3 formation in the Gr/Al composite system in the solid state is greatly influenced by the gaseous environment during heat treatment and by graphite crystalline orientation. Use of glassy carbon substrates is required to gain more knowledge concerning the effects of temperature and interfacial oxide thickness upon Al_4C_3 reaction

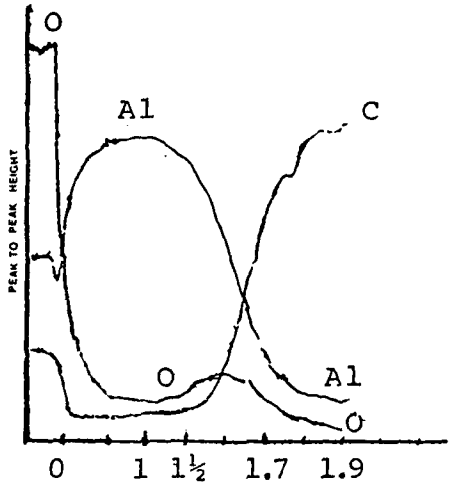

FIGURE 6(a)

Sputtering profile of single crystal Gr/Al thin layer composite with intermediate oxide. Heat treatment was at 550°C for 1 hr.

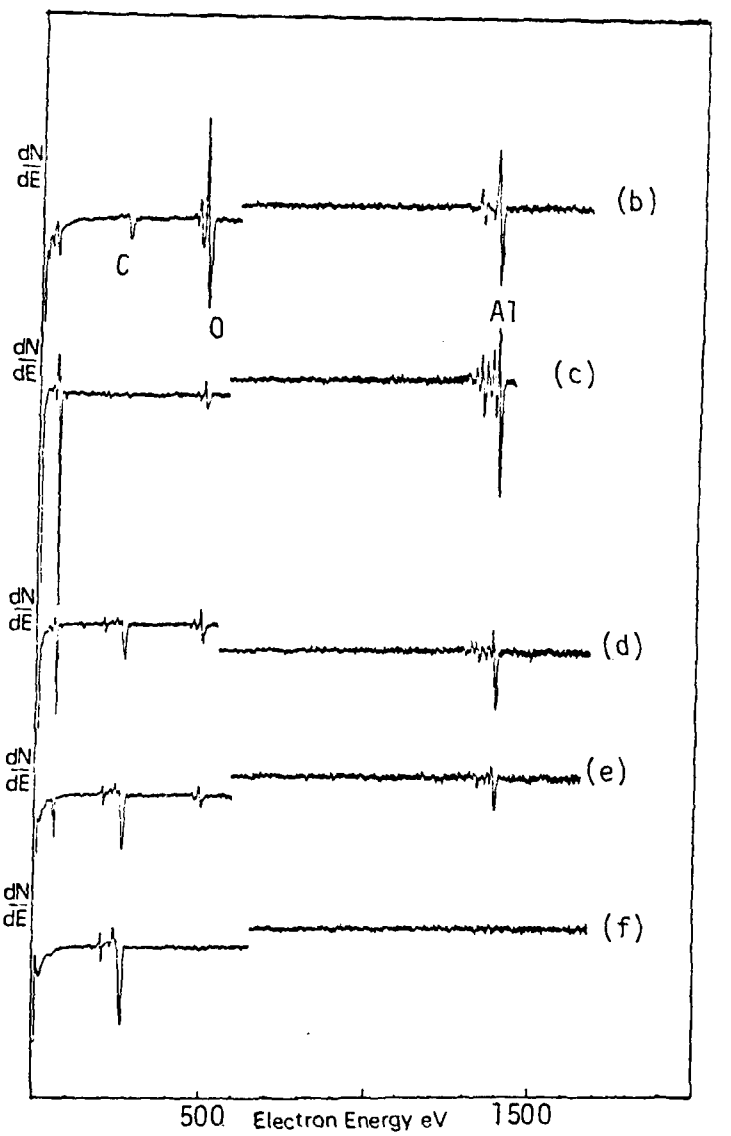

FIGURE 6(b-f)

Corresponding Auger spectra at various stages of sputtering, showing surface oxide (b), aluminum metal (c), intermediate oxide (d) and (e), and graphite substrate (f). In all cases, the carbon peak is predominantly graphitic in character, so little or no carbide has formed.

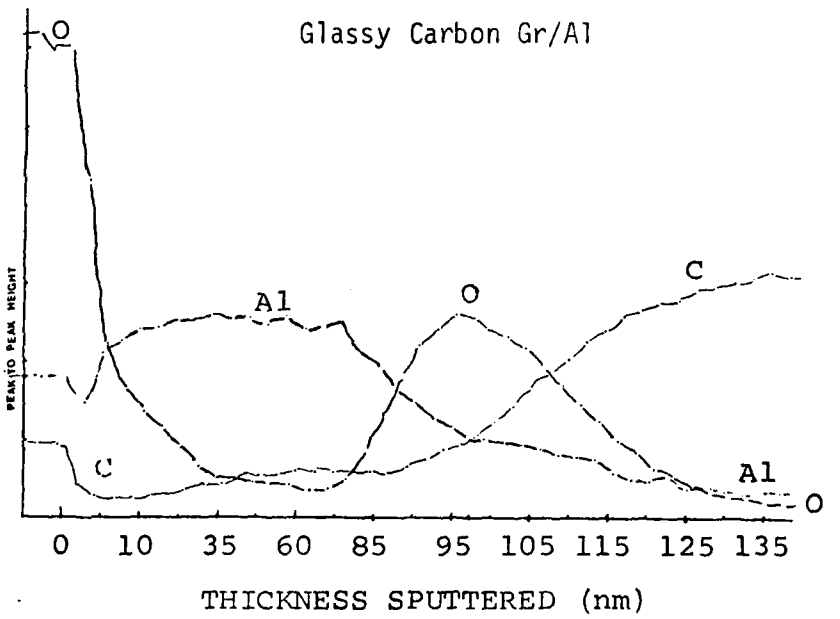

FIGURE 7

Sputtering profile of glassy carbon Gr/Al thin layer composite with 30 nm thin intermediate oxide layer. Layer definition is excellent with this type of substrate.

rate, as well as to provide additional confirmation for the belief that carbon atoms migrate through the interfacial oxide to combine with aluminum atoms and form Al_4C_3 which does not become dispersed into the bulk of the aluminum.

Reference

1 W.C. Harrigan and D.M. Goddard, Journal of Metals 27 (5) (1975) 20.

(Published in the Proceedings of the 28th Sagamore Army Materials Conference, July 1981.

Appendix G

RESIDUAL STRESS MEASUREMENT IN METAL MATRIX COMPOSITES

Swe-Den Tsai, M. Schmerling and H.L. Marcus

Department of Mechanical Engineering/Materials Science and Engineering, The University of Texas Austin, Texas 78712

INTRODUCTION

Due to the large difference in the coefficients of thermal expansion of the continuous fibers and the metal matrix in metal matrix composites, a large residual stress pattern could be expected when the composite is cooled from the fabrication temperature to room temperature. This paper will first briefly describe the x-ray techniques used to measure the residual stresses and then present and discuss the residual stress results obtained. Experiments were done on aluminum, magnesium and titanium matrix composites. This paper will concentrate on the measurements in the aluminum graphite system. It should be noted that the reported residual stresses are only from the matrix phase due to the difficulty introduced by the large texture in the graphite fibers.

EXPERIMENTAL AND ANALYTICAL PROCEDURES

The fundamentals of determining stress with x-ray diffraction have been defined in detail elsewhere in this symposium. In this section, simple principles and methods related to the x-ray techniques as applied to the measurement of residual stress in the metal matrix continuous fiber composites are presented.

The residual stresses of Graphite-Aluminum composites were measured utilizing the diffractometer technique to quantitatively record the intensity profiles. Two kinds of diffractometers with different geometrical configuration and optics were applied: the classical Bragg-Brentano diffractometer, also called ω-diffractometer, and ψ-diffractometer, which is similar to the Schulz method

for pole figure determination. The classical ω-diffractometer was the most common instrumental arrangement for many years. While still in heavy use in the United States, it is being superceded by the "ψ-diffractometer" in Europe and Japan.

In the ω-diffractometer, the ψ tilt angle is obtained by rotating the specimen on the goniometer axis independently of the counter, or say, parallel to the 2θ axis. As seen in Fig. 1, this would produce a new focal point. In order to achieve the best possible focusing during the ψ inclination, the receiving slit and the detector must be moved to a new point C in Fig. 1b. The motion of the receiving slit must be truly radial or an error will occur.[1]

The stress measurements were also made on a "ψ-diffractometer," where the specimen is rotated around an axis lying parallel to the diffractometer plane, i.e., normal to the goniometer axis, as in Fig. 2. The principle characteristics and application have been summarized by Macherauch and Wolfstieg.[2] This diffractometer, often referred to as the "side-inclining procedure", has its unique advantages lying in the fact that the incident and diffracted rays are equal path lengths and independent of θ,ψ and vertical divergence. During rotation of the specimen around the ψ axis, the x-ray tube, specimen surface and the counter all remain on the focusing circle eliminating the relocation of the receiving slit to obtain optimum focusing. As the path length for incident and scattered beams inside the specimen is the same, we do not need the absorption correction after a ψ-tilt as we do for the ω-diffractometer.

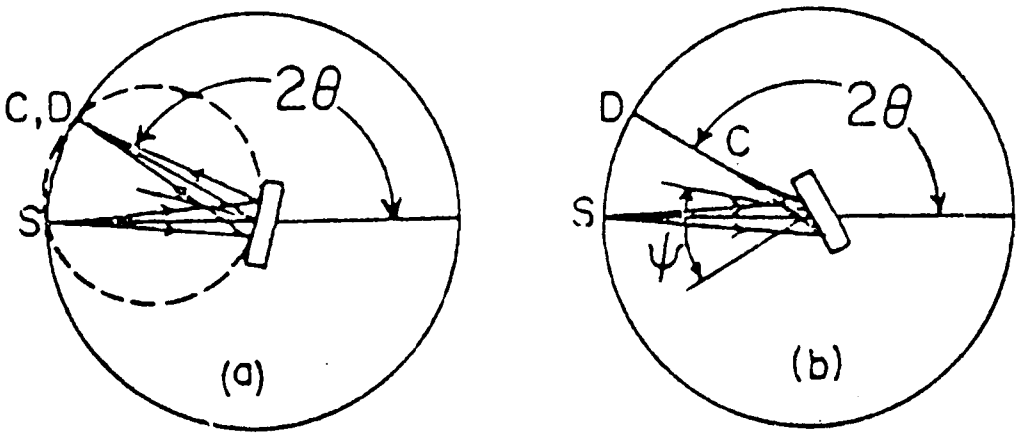

Fig. 1. ω-diffractometer. The ψ angle is tilted around the axis perpendicular to the drawing.
(a) specimen is on the focusing circle when ψ=0.
(b) the focus moves when the specimen is tilted ψ.

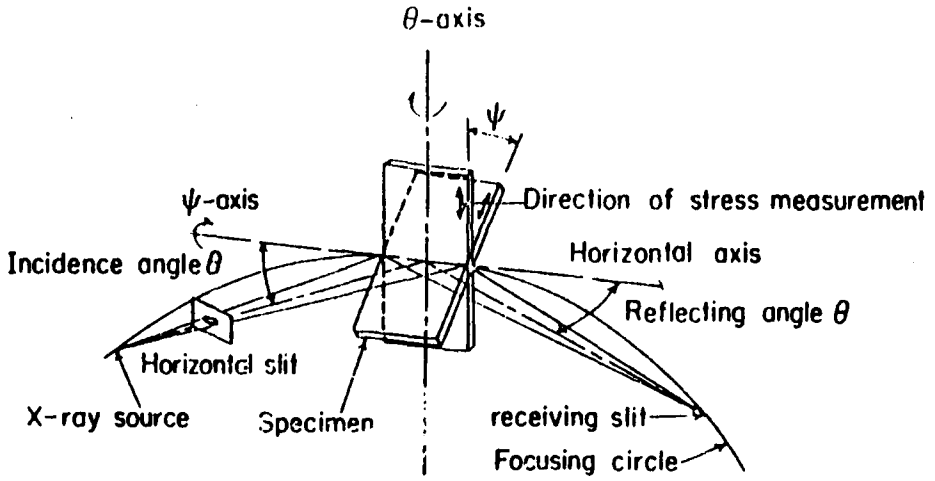

Fig. 2. ψ-diffractometer. The ψ angle is tilted around an axis in the plane defined by the incident and diffracted beams.

Except for many of the unpredictable sources of error which depend on either alignment, sample position or electronic stability, there are some predictable factors influencing the bias in the precision control. The following will be concerned with their effects and significance to our experiment:

(a) Lorentz-Polarization Factor

This term combines two 2θ dependent intensity corrections, the Lorentz factor and Polarization factor which are important in both ω and ψ diffractometer. The conventional correction factor for filtered radiation designated L_p, is:[3]

$$L_p = \frac{1+\cos^2 2\theta}{\sin^2\theta}$$

(b) Absorption Factor

This is significant in ω-diffractometer. For a flat sample the measured intensity is corrected by dividing by:[4]

$$ABS = 1-\tan\psi \cot\theta$$

(c) Atomic Scattering Factor and Temperature Factor

For alloys these two terms are often complex and usually

neglected. The Debye temperature factor is a very small correction relative to the others. Since we are measuring the stress of aluminum matrix in the composite, the atomic scattering factor for aluminum metal was incorporated in the correction. The temperature factor was not considered.

After the intensity distributions have been corrected by these factors, the angle of the diffraction peak for various ψ tilts could be determined from a consistent feature of line profile. In residual stress measurements using x-ray diffraction, the profile has been traditionally defined in the U.S. by the apex of a parabola fit to the top region of intensity curve. The data points were selected following the rule of using only approximately the top 15%, then fitting the points to a parabola by least squares fit.

Eleven data points were selected to accumulate the counts instead of regular three or five points parabola for both types of diffractometers. The use of these multiple data points (rather than three) and a least-squares parabolic fit have been demonstrated to improve the reproducibility significantly in a computer automated data collection system.[5] The eleven data point profile is not necessary for manual collection systems. The reason for using the eleven point parabolas in both types of diffractometers was to keep the analysis consistent.

The ω-diffractometer measurements were made at Northwestern University on a computer controlled Picker-diffractometer following the parafocusing geometry and the results were reported elsewhere.[6] The hardware, software and its capability have been described.[5] $Sin^2\psi$ angle tilts taken in equal increments were employed. In order to counteract grain size effect, 2θ-oscillations of 2 degrees were employed when necessary. The matrix grain size here is approximately a few tenths of a millimeter. The cobalt x-ray source of 0.15 cm^2 aperture size was employed. About 90 percent of intensity came from a depth of 5.4×10^{-3} cm of sample surface. Because of the ease of doing repetitive peak determination and the method of collecting counts on the selected data points in this automated system, only the data with a correlation factor of 0.95 or above in the linear least-squares fit for d versus $\sin^2\theta$ were considered reliable. For the ψ diffractometer, a Siemens texture diffractometer with adjustable beam size aperture was applied, and the GE x-ray source combined with this Siemens diffractometer was also used for some of the specimens. The manual step scans of 2θ for the data accumulation were controlled carefully. Although this required a tedious and time-consuming procedure, there was flexibility in choosing peak position and breadth which varies with sample, residual stress level and ψ angle. The advantages in optics and geometry for the ψ-tilt described earlier in this section made this technique superior. A copper radiation source was used. A horizontal beam size of 0.1×0.5 cm^2 was adjusted in the beam aperture. The raw data

were then processed by a computer program. The peak locations and the stresses were thus determined. Either fix-count or fix time accumulation procedures were used to maintain good statistical errors.

The residual stress measurements were made on many of the graphite-aluminum composites. Different fiber type and processing methods were used to produce the composites studied here. The variation of fiber properties and processing procedures could modify the mechanical properties as well as the stress state on the interface area. The components of the composites studied are listed in Table 1. All the materials here, except the Pitch/6061 G4371 and G4411, were produced using the standard Ti-B CVD coating process onto the graphite fibers prior to passing the fiber tow through the aluminum melt. Pyrolytic carbon coating prior to the Ti-B processing was used in G3437 and precoating of porcelain enamel[7] was applied in PANII/6061 G3675. The precursor wire produced by these processing methods was then consolidated into plate form by diffusion bonding. Residual stress measurements were also made on the samples of Rayon/201 G3394 and PANII/201 G3437 quenched to liquid N_2 temperature and then tested at room temperature. To establish base line data composite Rayon/201 G3394 with high modulus fiber and the low modulus fiber composite G3437 which has about one half transverse strength of G3394 were selected to see the effects of the thermal

Table 1. Components and Properties of Aluminum Graphite Composites

Composites	Fiber	Base	Young's Modulus of Fiber x10^6 psi	Matrix
G3394	Thornel 50	Rayon	60	Al 201
G3437	Thornel 300	PAN II	34	Al 201
G3675	Celion 6000	PAN II	35	Al 6061
G3669	Celion 6000	PAN II	35	Al 6061
G4371	VSB-32	Pitch	55	Al 6061
G4411	VSB-32	Pitch	55	Al 6061

*The matrix of G3394 and G3437 are Al 201. Matrix for the other composites are Al 6061. Young's modulus for Al 201 and 6061 are 10.2 and 10 (Mpsi). The yield strength are 35 ksi and 37 ksi respectively.

expansion mismatches and correlation with transverse strength. The PANII/6061 G3675 and G3669 were chosen because of the high content of Al_4C_3. The G3675 is an extreme case of very high transverse strength with a degraded longitudinal strength. The composite G3471 and G4411 with high modulus fiber VSB-32 and 6061 Al alloy matrix were also analyzed here. The measurements of the change in the residual stress patterns of the liquid nitrogen quenched samples were to relate them to the transverse strengths measured before and after quenching.

Due to the relatively large divergent beam impinging on the sample surface and the penetration depth greater than a monolayer of fibers, the stress measurement obtained was a volume average over the matrix, similar to the one represented by the dotted line in Fig. 3. For such a volume average, the penetration dpeth of x-ray becomes an important parameter. Since it is the stress in the vicinity of the interface that is of interest here, it is essential to expose the interface in the specimen to the x-rays. This is a particular problem in the Ti composites where the fibers are about 150 micrometers in diameter. In other words, the penetration depth should be such that the x-rays average over the region which includes interfaces.

In the preparation of the samples, mechanical polishing was not used, since it could introduce extra residual stress. By electropolishing, enough surface material could be removed so as to expose the interface area, and to get rid of the surface layer that may have been stressed by mechanical work. The electrolyte

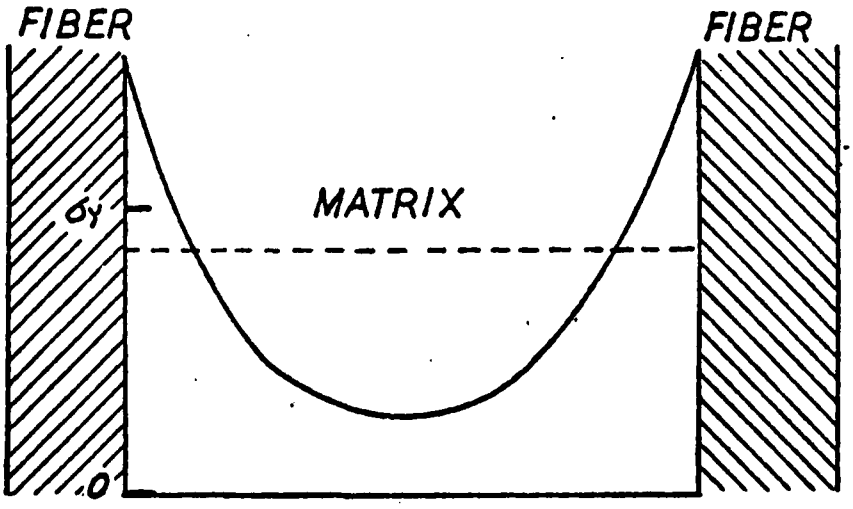

Fig. 3. A simple model to show the residual stress distribution. The dotted line is an average value. The term σ_y is the yield strength of the matrix.[6]

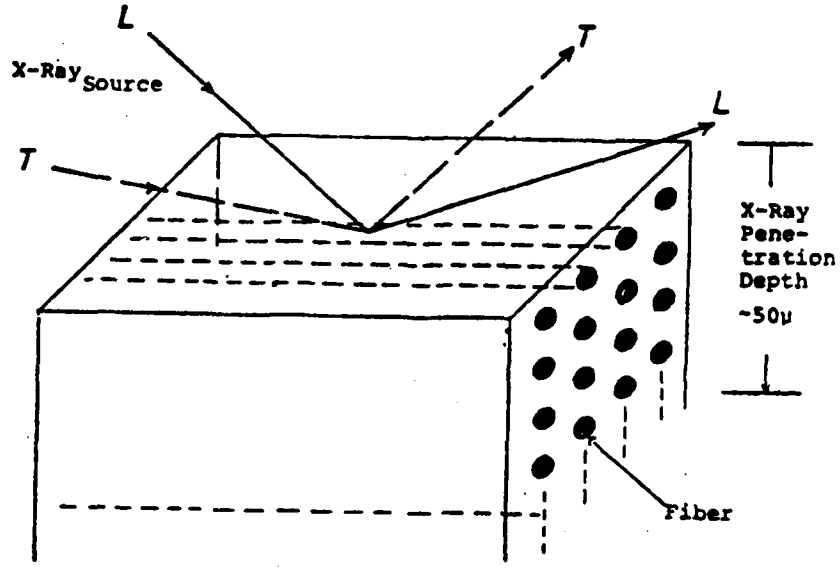

Fig. 4. Stress Measurement geometry. L=longitudinal; T=transverse.

used for the aluminum graphite was a solution of one part concentrated nitric acid in 3 parts of methanol by volume. For Rayon/201 G3394, PANII/6061 G3437, and G3669, Pitch/6061 G4371 and G4411 the sample surfaces were polished just enough to expose portions of interfaces. With PANII/6061 G3675, a sample with light electrolytic polishing was prepared. This resulted in a thin surface layer of aluminum above the fibers having thickness greater than the penetration depth of the x-rays. Thus, during volume averaging only the aluminum matrix containing no fibers would be covered. In addition, a heavier polishing was also done on the sample of Pitch/6061 G4411 composite to reach the deeper region down into the surface, after the stresses of the normally polished surface were measured. The stress levels then could be compared versus the distance from the surface of the sample. Specimens used were plates with the approximate thickness from 0.15 to 0.4 cm, and dimensions 1.9 to 2.5 for the width and length. The area of plates was large enough so that the beam divergence could stay within the center portion of the specimens. Residual stress measurements were made in both the longitudinal and transverse directions to the fiber axis, as indicated in Fig. 4.

RESULTS AND DISCUSSION

The high angle peak of aluminum (420) diffraction was used for the stress measurements to achieve high accuracy. The residual stresses determined using the ω-diffractometer system are listed in

Table 2a[6] and those measured by ψ-diffractometer arrangement are listed in Table 2b. The tables also list the transverse and longitudinal strengths of composites and the correlation factors for the least squares straight line fit for the lattice strain vs $\sin^2\psi$.

It may be noted that the longitudinal direction stress values for Rayon/201 G3394 and PANII/201 G3437 are comparable to the nominal 240 Mpa yield strength of the 201 aluminum matrix. This can be explained by the mismatch of thermal expansion coefficients between two components. Table 3 presents this difference in thermal properties. In the graphite fiber/aluminum composite Rayon/201 G3394, there is a mismatch of approximately $23\times10^{-6}/°C$ in the thermal expansion coefficients along the longitudinal direction.[8] The sample is cooled by almost 600°C after solidification, giving rise to significant amounts of residual stresses in the fiber direction. A calculation using a planar model[9] and a cylinder model with proper boundary conditions[10] show that stresses well above the yield strength of aluminum exist at the interface of the aluminum matrix-graphite fiber. Plastic flow could be expected to occur because of the high values of thermally-induced stresses. Assuming no debonding, a stress gradient is expected in the Al matrix, with above-the-yield strength stress at the interface. A schematic of the expected stress distribution was given in Fig. 3. The dotted line represents the measured average value of stress in the aluminum matrix. All of the matrix is expected to be in a state of tensile stress minimized at a point between fibers.

While there is a significant difference in thermal expansion coefficients of Al and graphite in the longitudinal direction, this difference is negligible in the transverse direction for Rayon/201 G3394 due to the anisotropy of the graphite fiber. Hence, the thermally induced residual stresses in the transverse direction are not expected to be as high as those in the longitudinal direction. These transverse residual stresses are mechanical in origin, since a tensile residual stress state[11] is introduced in the matrix after cooling the composite from elevated temperatures.[12]

In composite PANII/201 G3437, the residual stresses are large and very close to those measured in Rayon/201 G3394 in the longitudinal direction. This could be expected, since the mismatch of thermal expansion coefficients along the fiber direction in PANII/201 G3437 is similar to that in Rayon-201 G3394. As for the residual stresses in the transverse direction, PANII/201 G3437 has the stress level a little higher than those in Rayon/201 G3394; they have values of 116 Mpa and 73 Mpa respectively. This situation is due to the moderately large thermal expansion coefficient mismatch, a value of about $15\times10^{-6}/°C$.

The lower levels of stresses, however, were observed in the composites PANII/6061 G3675 and G3669 which are fabricated from a

Table 2a. Residual Stresses Measured from ω-Diffractometer

Material	Transverse Strength MPa	Longitudinal Strength	Direction of measurement	Residual Stress MPa	Correlation Coefficient
G3437	10	1120	L	199.38	0.9640
			T	166.28	0.9658
G3394	20	763	L	228.38	0.9945
G3675 (lighter polishing)	75	259	L	40.71	0.9507
			T	33.26	0.9788
G3437 (cooled to liquid N_2 temperature and measured at room temperature)	10 (before quench)	1120	L	144.11	0.9856
			T	120.20	0.9924

Table 2b. Residual Stresses Measured from ψ-Diffractometer

G3394	20	763	L	213.75	0.987
			T	72.40	0.875
G3675 (No. 1)	75	259	L	42.06	0.971
			T	40.33	0.988
G3675 (No. 2)			L	46.38	0.986
			T	26.44	0.970
G3669	28	303	L	68.03	0.956
			T	39.54	0.969
G4371	10	892	L	58.52	0.991
			T	60.44	0.988
G4411	7	565	L	55.48	0.999
			T	56.83	0.914

AD-A127 590 INTERFACE CHARACTER OF ALUMINUM-GRAPHITE METAL MATRIX COMPOSITES(U) TEXAS UNIV AT AUSTIN MATERIALS SCIENCE AND ENGINEERING H L MARCUS 27 JAN 83 UTMSE-83-1 2/2

UNCLASSIFIED N00014-78-C-0094 F/G 11/4 NL

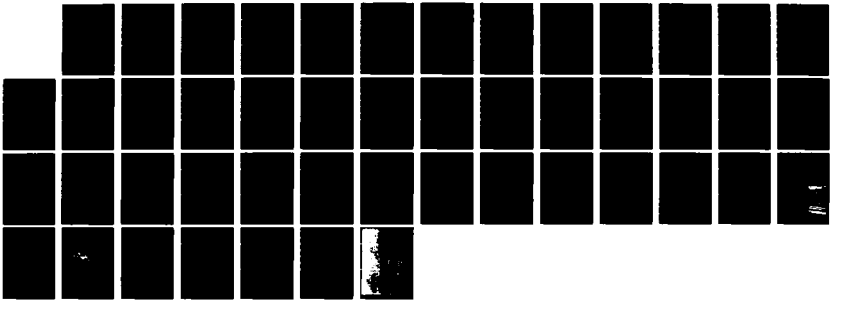

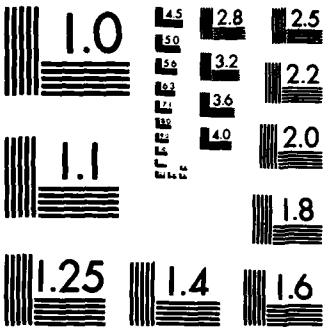

MICROCOPY RESOLUTION TEST CHART
NATIONAL BUREAU OF STANDARDS-1963-A

(Table 2b continued)

Material	Transverse Strength MPa	Longitudinal Strength	Direction of measurement	Residual Stress MPa	Correlation Coefficient
G4411 (heavier polishing)			L	55.48	0.999
			T	82.68	0.885
G3394 (quenched to liquid N_2 temperature and measured at room temperature)			L	131.94	0.900
			T	-46.00	0.983

L=Longitudinal T=Transverse Direction

Table 3. Thermal Expansion Coefficient of Component Materials[8]

Components	Thermal Expansion Coefficient $10^{-6}/°C$
Thornel 50 (Fibers in G3394)	$-0.1 \sim -0.54\alpha_{fL}$ (Axial direction) to about 300°C
	25 (Transverse direction)
Thornel 300 (Fibers in G3437)	$8.0*\alpha_{fT}$
	$-0.7*\alpha_{fL}$
Al-201 Matrix of G3394, G3437	23.22
Celion 6000	Assumed the same as Thornel 300
Al-6061 Matrix of G3675, G3669, G4371, G4411	23.58

PAN II base Celion 6000 fibers with 6061 aluminum matrix. The nominal physical properties of this fiber should be very close to those in the Thornel 300 fibers of the same PAN II base material. The thermal expansion could be expected to increase or decrease as the

fiber modulus decreases or increases in the longitudinal axial direction since both properties are closely related to the degree of crystal preferred orientation. Presumably, the mismatches between fiber and matrix could be expected to be similar to the case of PAN II/201 G3437, therefore, the similar stress levels should be measured. However, the low modulus PAN II fibers are highly reactive with molten aluminum during the infiltration process and aluminum carbide is easily formed in the interface region. This high activity is closely related to the surface characteristics of the fiber, i.e., preferred orientation in graphite crystallites. Generally speaking, the highly graphitized high modulus fibers are less reactive with Al in the infiltration process while the low modulus fibers are badly degraded.

In PANII/6061 G3675 and G3669, the Al_4C_3 content is higher than the average amount, while the content in PANII/201 G3437 is much lower than the average one. This reduction in Al_4C_3 results from the application of the oriented pyrolitic carbon layer, which limits fiber-matrix interaction. A comparison of the Al_4C_3 contents in those composite systems is given in Table 4.[13] The formation of a large amount of carbide layer at the interface effectively provides a "grading seal" that can relieve the residual stress pattern in the interphase region. This is due to a thermal expansion coefficient of Al_4C_3 at about $10 \times 10^{-6}/°C$ as estimated from the melting temperature (2750°C) relationship with thermal expansion.[14] This value is halfway between those for aluminum and the graphite fiber. Consequently, the residual stress levels are reduced to a relatively low value. Actually, the model described in Fig. 3 did not consider a finite thickness interphase. It has been observed in the TEM and Auger studies that oxides, carbides, and/or borides are present at the fiber-matrix interface. Since the mismatch between the thermal coefficients of the compounds and the aluminum matrix is lower than that of fiber and aluminum in the longitudinal direction, the maximum longitudinal residual stress at the interfaces can be expected to be lower than when a simple graphite-aluminum interface exists.

Table 4. Al_4C_3 Contents in Composites

Composites	Al_4C_3 Content ppm
G3437 PANII/201 (Pyrolitic carbon coated)	690
G3675 PANII/6061	3644
G3669 PANII/6061	9387

Relatively low stresses also were measured in the VSB-32 Pitch/6061 aluminum composites, G4371 and G4411. There was little in the residual stresses between those before heavier electrolytic polishing and after. The heavier polishing removed 100~120 μm thickness from the normally polished surface. Because of the high modulus and thus the highly preferred orientation of basal plane along the fiber axis, a low axial thermal expansion coefficient α_{fL} close to the value in T 50 fiber is expected. Correspondingly, a large expansion mismatch should exist in the longitudinal direction of the fiber. Assuming the good bond was formed at interfaces, the lower residual stresses observed could be attributed to the relaxation effect of the thin composite plate used, since only two or three plies of precursor wires were consolidated to make these plates. This can be compared to the four to six layers with aluminum wrapping for the other plates. The thicknesses are about 0.15 cm and approximately 1/3~1/2 of those in the other materials. Then, the stresses may not be fully constrained in the composite plates. This low residual stress value has not been totally rationalized.

When the high residual stress samples Rayon/201 G3394 and PANII/201 G3437 composites were quenched in liquid nitrogen and annealed at room temperature, approximately 30% reduction in residual stress was observed. The cryogenic cooling induces additional plastic flow in the matrix, establishing a new elastic condition at the cryogenic temperature. Heating the composite back to room temperature will then relieve much of the residual stresses. However, the 30% is less of a reduction than is expected. Additional work hardening at the interface occurring during cooling may explain this difference between the measured and calculated changes. In the materials used here the room temperature transverse strength of composites did not change significantly before and after being quenched in liquid nitrogen.

A sample of Rayon/201 (G3394) composite was used as a standard and the measurements were made in both ω and ψ diffractometers. The very good agreement found assured that the measurements from both types of diffractometers are consistent and comparable.

SUMMARY

X-ray diffraction can be very effectively applied to determine average residual stresses due to the mismatch in thermal expansion coefficients in the graphite-aluminum composite system. The indications are that the residual stresses averaged through the distribution in aluminum matrix are not directly related to the transverse strengths. The basic properties related to the interface strength are associated with the multiple interfaces between the various phases such as oxide, carbide, boride layers

and the complexity of the metallurgical interactions. However, the x-ray residual stress measurement described in this paper helps in the understanding of how the components and their properties influence the interfacial behavior.

ACKNOWLEDGEMENTS

This research was supported by ONR under contract N00014-78-C-0094. The authors would like to acknowledge the assistance of Dr. J.B. Cohen and Ismail C. Noyan in the ω-diffraction measurements and Norman Williams and Dr. Hugo Steinfink in the ψ-diffraction measurements.

REFERENCES

1. M.E. Hilley, J.A. Larson, C.F. Jatczak and R.E. Ricklefs, "Residual Stress Measurement by X-Ray Diffraction," SAE Information Report, J. 784a, SAE Pennsylvania (1971).
2. E. Macherauch and U. Wolfstieg, Adv. in X-Ray Analysis 20: 369-377 (1977).
3. J.B. Cohen, "Diffraction Methods in Materials Science," MacMillan Co., New York (1966) p. 225.
4. D.P. Koistinen and R.E. Marburger, Trans. ASM. 51: 537-555 (1959).
5. M.R. James and J.B. Cohen, Adv. in X-Ray Analysis 20:291-308 (1977).
6. Swe-Den Tsai, Deepak Mahulikar, H.L. Marcus, Ismail C. Nayan and J.B. Cohen, Mat. Sci. and Eng. 47:145 (1981).
7. G.L. Steckel, R.H. Flowers, and M.F. Amateau, "Transverse Strength Properties of Graphite-Aluminum Composites," in Failure Modes in Composites IV, J.A. Cornie and F.W. Crossman, eds. Conference Proceedings, The Metallurgical Society of AIME (Fall 1977).
8. T. Ishikawa and S. Kobayashi, "Thermal Expansion Coefficients of Unidirectional Fiber-Reinforced Composites," parts 1 and 2, J. Jpn. Soc. Aeronaut. Space Sci. 25:394-400, 423-429 (1977).
9. C.A. Hoffman, "Effects of Thermal Loading on Composites with Constituents of Differing Thermal Expansion Coefficients," NASA-TN-D 5926 (1970).
10. S.S. Hecker, C.H. Hamilton and L.J. Ebert, "Elastoplastic Analysis of Residual Stresses and Axial Loading in Composite Cylinders," J. of Matls. JMLSA 5, no. 4:868-900 (Dec. 1970).
11. J. Gayda and L.J. Ebert, Met. Trans 10A:349-353 (1979).
12. Masuji Vermura, Hisashi Iyama and Yoshiko Yamaguchi, J. of Thermal Stresses 2:393 (1979).
13. F. Padlla, W.C. Harrigan, Jr. and M.F. Amateau, "Handbook of Test Methods for Evaluation and Qualification of Aluminum-Graphite Composite Materials," Materials Sciences Laboratory

The Aerospace Corporation, El Segundo, CA (21 Feb. 1975).
14. C. Zwikker, "Physical Properties of Solid Materials," Pergamon Press, London (1954).

Appendix H

Auger Electron Spectroscopy Depth Profile of Thin Oxide on a Ti-Mo Alloy

Daniel Laser

Department of Chemistry, Tel-Aviv University, Ramat Aviv, Israel

Harris L. Marcus

Department of Mechanical Engineering/Material Science and Engineering, University of Texas at Austin, Austin, Texas 78712

Recently we investigated[1] the growth and properties of thin oxide films which were grown on a titanium electrode. It is the aim of this communication to describe some properties of an anodic oxide which were grown on a Ti-Mo alloy.

For the formation of a controlled oxide thickness on a bare substrate to be used as an AES sample, the previously described[1] method was employed which consists of polishing the electrode surface (3μ diamond dust embedded in a polishing cloth) while holding it at a cathodic bias (-0.95V vs SCE) and then applying to it a positive linear potential scan.

The alloy studied was the β-III, a Ti based metastable alloy (Ti, 11.5 Mo, 4.5 Sn, 6 Zr) the stress-corrosion behaviour of which was studied by Hickman et al[2] and which was used as received without any heat treatment.

The current/potential curve during the anodic potential scan of the alloy electrode in slightly acidic solution is shown in fig. 1, where it is compared to the voltammogram of pure Ti and pure Mo under the same conditions.

As in the case of pure Ti, the voltammogram is distinguished by an extended potential interval (∿ 2V) in which the anodic current which is attributed to oxide formation remains constant. Such a mode of oxide growth results in the formation of a homogeneous film the thickness of which varies linearly with the applied potential at full current efficiency.[1] However, the "dissolution peak" which is observed at pure Ti (∿ -0.65V) is missing. This is in agreement with the finding of Tomashov et al[3] who find a suppression in the dissolution rate of Ti at the prepassive state when alloyed with Mo in the β phase and will be discussed later.

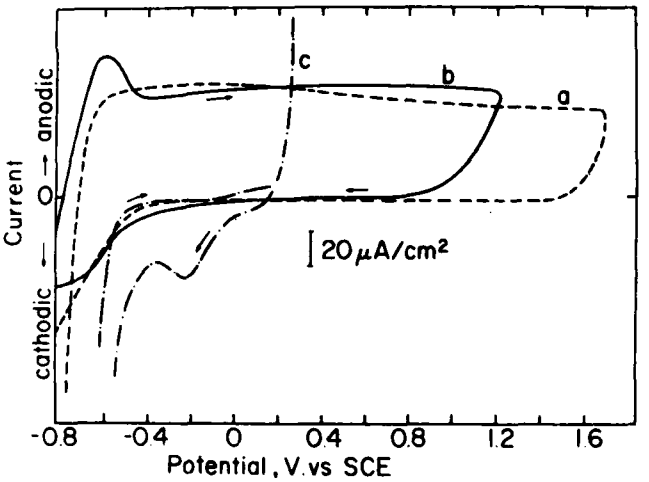

Fig. 1. Current voltage curve for a - β III alloy, b - Ti and c - Mo in 1N Na_2SO_4, PH 2.3.

Little is known about the composition of anodic oxides of alloyed Ti. Recently Paleolog et al[4] assumed that the anodic oxide of a Ti-Ni alloy consists mainly of TiO_2 with Ni doping at the metal/oxide interface.

We adopt a similar picture with regard to the distribution of Mo within the oxide of the β-III and in order to probe it the oxides were subjected to Auger Electron Spectroscopy (AES)

Key Words: Alloy, Electrode, AES, sputtering

depth profiling immediately after their formation with the use of a PhI Model 590A Scanning Auger system equipped with sputtering, multiplexing and in situ fracturing facilities.

The difficulties in quantitative AES application to very thin (<100A) TiO_2 films and to Mo oxides have been described before[5,6]. However, our aim was to locate the Mo distribution within the oxide. The appearance of the Mo major peaks (186,221 ev in the $\frac{dN}{dE}$ mode) in the absence of the 27ev peak which is characteristic of metallic Ti, proves the existence of Mo within the oxide if the escape depth of the 27 and 221(186)ev Auger electrons are assumed to be about equal. The depth profile of the oxide is shown in fig. 2. The outer layer of the oxide (oxide/solution interface) consists exclusively of TiO_2 and the Mo concentration increases toward the metal oxide interface. The increase in the carbon concentration increases toward the metal oxide interface. The increase in the carbon concentration in this region is attributed to the polishing procedure prior to film formation (polishing with diamond dust). It should be noted that a similar apparent distribution of Mo can result if: (a) There is a preferential sputtering of Ti over Mo[7] which leads to the surface accumulation of Mo during the sputtering, or (b) Mo is gradually reduced by the ion beam,[6] or continuously changes its oxidation state while penetrating the film in such a way that its Auger peak shape is changed and enhanced even without any increase in its concentration.

Possibility (a) should also be manifested after the film is completely sputtered through; however the Mo signal then reaches a steady state. Also the Auger peak of Mo oxide grown at 1V did not change during the sputtering which eliminates the second possibility. We believe the chemical state of Mo within the oxide to be that of Mo ion (Mo^{+3} or Mo^{+5}), which because of its size, does not fit the TiO_2 phase and thus exhibits in it a much slower mobility than the Ti ion. It probably does not reach the solution/oxide interface except in the very early stages of film growth.

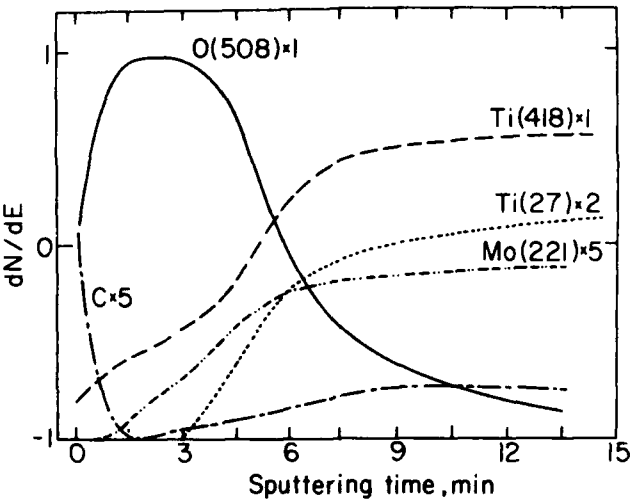

Fig. 2. AES depth profile of oxide formed at β III alloy at 2V vs SCE, solution as in fig.1. Sputtering by 3 kev Kr^+ ions.

The absence of the Ti dissolution peak (fig.1) may be relevant to the superior behaviour of this alloy in corrosive media[2,3] when the bare substrate might be exposed to solution. Two explanations, which are supported by the AES findings, can be provided for this observation. Firstly: In the AES of pure Mo or of its oxide the 221 ev Auger peak is smaller than the 186 ev peak, but the 221 ev peak of Mo in the alloy is bigger than the 186 ev one (in the $\frac{dN}{dE}$ mode, fig.3). This reflects some specific interaction between Ti and Mo in alloyed state, which may possibly stabilize the Ti atom in the solid compared to its state in pure Ti. Secondly: At -0.95V while polishing, Ti dissolves into solution[1], but

this electrode potential is too negative for the Mo dissolution[8] and it seems, therefore, feasible that the substrate surface prior to film formation is enriched with Mo which provides a barrier for the Ti dissolution. Indeed, the concentration of Mo which is found by AES after the oxide is removed by sputtering and which represents its quantity at the surface prior to anodization, is much higher than its concentration at the surface which was obtained by the in situ fracturing of the alloy (fig.4)

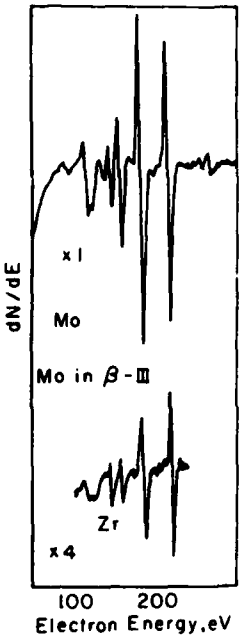

Fig. 3. AES of Mo in its pure state and in β III alloy.

References:

1. D. Laser, M. Yaniv and S. Gottesfeld, L. Electrochem. Soc., 125, 358 (1978).
2. B.S. Hickman, H.L. Marcus and Y.L. Williams, "Stress corrosion cracking of Titanium Alloys in Methanolic and Aqueous Environments". Presented at an International symposium on Stress Corrosion Mechanisms in Titonium Alloy, Atlanta, Georgia, January 1971.
3. N.D. Tomashov, G.P. Chernova, Y.S. Ruscal and G.A. Ayuyan, Electrochim. Acta, 19, 159 (1974).
4. E.N. Paleolog, A.Z. Fedotova, O.G. Derjagina and N.D. Tomashov, J. Electrochem. Soc., 125, 1410 (1978).
5. H.J. Mathieu, D.E. McClure and D. Landolt, J. Vac. Sci. Technol. 14, 1023 (1977).
6. T.T. Lin and D. Lichtman, J. Vac. Sci. Technol., 15, 1689 (1978).
7. M.L. Tarng and G.K. Wehner, J. Appl., 43, 2268 (1972).
8. A.A. Pozdeeva, E.I. Antonovskaya and A.M. Sukhotin, Corros. Sci., 6, 149 (1966).

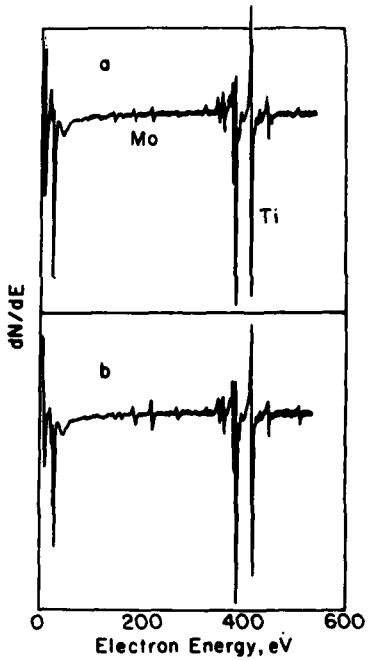

Fig. 4. AES of β alloy; a - fractured in UHV, b- after sputtering through the anodic oxide.

Acknowledgement: This work was supported by the office of Naval Research under contract number N00014-78-C-0094.

Manuscript submitted Sept. 28, 1979; revised manuscript received Dec. 21, 1979.

Scripta METALLURGICA Vol. 14, pp. 1135-1138, 1980 Pergamon Press Ltd.
Printed in the U.S.A.

ANOMALOUS SPUTTERING EFFECTS IN THE AES GRAIN BOUNDARY ANALYSIS OF REVERSIBLE TEMPER EMBRITTLED LOW ALLOY STEELS

Michael Schmerling, Duane Finello, and H.L. Marcus
Mechanical Engineering/Materials Science and Engineering
The University of Texas at Austin
Austin, Texas 78712

(Received July 28, 1980)

Introduction

The mechanism of reversible temper embrittlement in alloy steels involves the segregation of alloying elements to grain boundaries. This embrittlement consists of an increase in the ductile-to-brittle transition temperature and can be reversed by annealing for several minutes at temperatures above 600°C (1,2). The segregation of elements such as Ni with Sn, Sb, P, and other metalloids to prior austenite grain boundaries was confirmed using surface analysis by Auger electron spectroscopy (AES) in conjunction with inert ion sputtering (with incident ions from 0.5 to 5 KeV energy), which allows depth profiles of elemental concentration to be taken (3,4,5). Diffusion of these elements occurs over long periods of time in the embrittling range (~ 350 - 575°C).

Depth profiles indicate that most embrittling alloying elements are concentrated in thin layers (~ .5 to 1 nm) at the boundaries, but that Ni segregation appears in a somewhat thicker layer (1 - 3 nm)(3,5,6). Possible explanations for this effect are (1) actual difference in depth, (2) difference in sputtering rates resulting in selective sputtering. Since artifacts due to preferential sputtering are often encountered when depth profiles are made, it is necessary to check the profiles against a standard preparation. Results from this type of measurement are presented here.

Experimental Procedure

Step-cooled brittle alloys of a Ni-Cr-Sn steel (3.5 wt.% Ni, 1.7% Cr, .3% C, .06% Sn) were fractured in a scanning Auger microscope (PHI SAM 590 system) at a vacuum of 1.3×10^{-8} Pa. To reduce the likelihood of shadowing during sputtering of the rough surface, two ion guns (with an angle of 60° between them) were used. At approximately 500x magnification, grains were selected for analysis on a basis of facet orientation. A facet suitable for the analysis had to serve as a broad target for electron and ion beams as well. The electron beam position was kept stationary for the duration of each sputtering profile to maintain the spatial resolution below 5000 nm. Sputtering was performed with both ion guns at 4 KeV and 2 $\mu A/cm^2$ ion current with the chamber backfilled with argon to 4×10^{-3} Pa. All sputter profiles were continued until a steady state concentration representative of the sputtered bulk concentration was reached.

The fractured specimen was then moved from in front of the Auger analyzer to a position under a Ni filament. The filament was resistively heated in order to deposit a quantity of Ni so as to duplicate the concentration characteristic of the as-fractured surface, as evidenced by the Ni-Fe peak

0036-9748/80/101135-04$02.00/0

height ratio. The specimen was repositioned and a new sputter profile was taken at the same point as on the original profile. This was repeated for different deposition times.

As an additional test, co-deposition of Ni and Sn was undertaken. Co-deposition was performed through the use of an auxiliary Ni filament which had been wetted with Sn beforehand.

The conversion from sputter time to depth of material removed is based on sputter rates of Ta_2O_5 using the same experimental parameters for the sputter guns as in the Ni-Sn profiles. An exponential fit was used for obtaining a layer thickness from the sputtering data consistent with Ta_2O_5 sputter rates. A true exponential decay would occur only if the rate of concentration change were directly proportional to the amount on the surface in the form of a partial monolayer.

Results and Discussion

The profiles obtained showed roughly an exponential decay in the concentration of Ni and Sn. From the semilogarithmic plot of the elemental concentrations of Sn and Ni versus depth sputtered (Fig. 1), it is apparent that the rate controlling process for sputtering is different from that of Ni. One may define a time constant τ as the sputtering time required for the surface concentration of the segregated element to reach 1/e of the difference between the original surface concentration and the bulk concentration which is assumed to be the steady state surface concentration ultimately achieved during sputtering. τ is the negative reciprocal of the slope of the semilog plot line. For Ni, τ can be seen (Fig. 1) to be approximately twice that of Sn. All sputtering was continued until the bulk concentrations were seen.

For the series of Ni deposition experiments the sputter profile data had approximately the same time constant as the segregated Ni profile (Fig. 1). The sputter profile obtained from the Ni and Sn co-deposition test also indicates that the τ observed for Ni is approximately twice that of Sn. The conclusion from these experiments that Ni is less readily sputtered than Sn depends on the assumption that the coverage by deposition of Ni and Sn is primarily a surface phenomenon with interactions limited to the uppermost atomic layers alone. Implantation is deemed highly improbable since atoms leave a hot filament with relatively low ($< 1/2$ eV) energy.

The most likely morphology for Ni deposition on a facet of the grain would be a partial monolayer since the Ni-Fe signal ratio was found to be approximately a linear function of deposition time for the small quantities of Ni deposited. This would not be true for multilayered island growth. The fact that both the starting concentrations and the apparent depth profiles are the same implies that the Ni segregation results in approximately the same morphology. (If the coverage is kept to less than a monolayer, the finite escape depth of the Auger electrons and the backscattering factor do not influence the sputtering results.)

Various models have been proposed to explain the apparent long-range segregation of Ni in comparison to other segregating elements in low alloy steels (5,7,8). One involving precipitates of Ni-rich regions at carbide-ferrite boundaries or other locations would explain the depth of Ni but this account appears to be inconsistent with the present duplication of the rate of sputtering following deposition. Specimens quenched during various stages of embrittlement show Ni concentrations reaching a maximum away from the fracture surface, which is not the case after complete embrittlement (8). No attempt was made to duplicate partial embrittlement profiles in this study.

That large Sn atoms are more weakly bound to the matrix of smaller Fe atoms than are the Ni atoms, which are extremely close in size and structure to the Fe atoms, can explain the sputtering difference. The fact that Cr

(again similar to Fe and Ni) has been reported possibly to have a "longer" segregation range (8) may also be an artifact due to stronger bonding and corresponding lower sputtering rate.

Summary

The present research indicates that the morphology of the Ni segregated to grain boundaries in the low alloy steel exists over a thickness of approximately a monolayer in depth at the surface. The Ni segregation kinetics indicate a partial monolayer grain boundary morphology. Ni is strongly bonded to the grain and is therefore relatively difficult to remove with inert ion sputtering. The resulting slower sputter rate of the segregated Ni provides an explanation for the seemingly deeper concentration enrichment and degree of Ni segregation suggested by experiments involving AES in conjunction with IIS for low alloy steels.

Acknowledgements

The authors wish to thank General Electric Research and Development Laboratory for the steel alloy used. This research was sponsored by the Office of Naval Research, Contract N00014-78-C-0094.

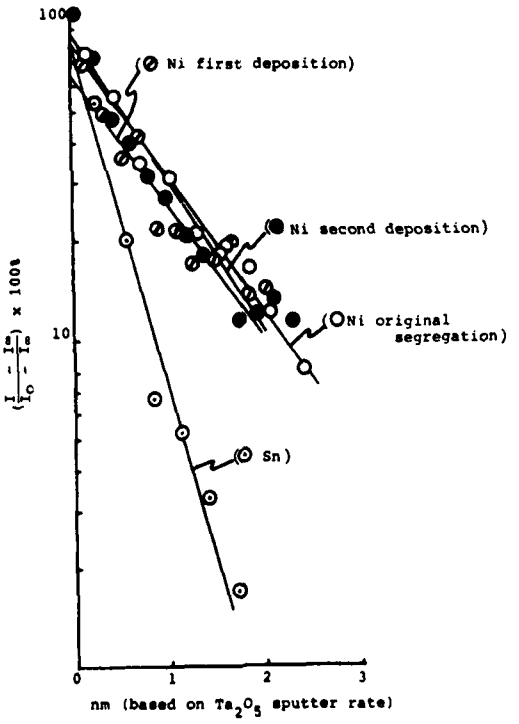

FIG. 1

Ni, Sn sputter profile
(lines through data points are least squares fit)

References

1. Low, J.R., Jr., (1969) Trans. AIME 245, 2481.
2. Guttman, M., (1980) Mat. Sci. Eng. 42, 227.
3. Marcus, H.L. and Palmberg, P.W., (1969) Trans. AIME 245, 1664.
4. Stein, D.F., Joshi, A. and LaForce, R.P., (1969) ASM Trans. Q. 62, 776.
5. Marcus, H.L., Hackett, L.H., Jr. and Palmberg, P.W., (1972) Temper Embrittlement of Alloy Steels, ASTM STP 499, 90.
6. Hondros, E.D., (1980) Phil. Trans. R. Soc. Lond. A. 295, 9-23.
7. Smith, C.L. and Low, J.R., (1974) Met. Trans. 5, 279.
8. Joshi, A. and Stein, D.F., (1972) ASTM STP 499, 59.

Appendix J

CHARACTERIZATION OF GRAIN BOUNDARY SEGREGATION IN MgO

Y.M. CHIANG, A.F. HENRIKSEN and W.D. KINGERY

Ceramics Division
Department of Materials Science and Engineering
Massachusetts Institute of Technology
Cambridge, Massachusetts 02139

D. FINELLO

Department of Mechanical Engineering
University of Texas at Austin
Austin, Texas 78712

Abstract

Using Auger electron spectroscopy, segregation of Ca and Si corresponding to the adsorption of a partial monolayer adjacent to the boundary in polycrystalline MgO has been observed. Segregation of Sc is different in nature; the distribution consists of a 3.0 nm-wide region corresponding to a positive space charge layer balancing a negative boundary charge. Various segregation models have been applied to the observed behavior.

I. Introduction

Recent investigations have indicated that segregation of solutes onto grain boundaries in oxides is more the rule than the exception. Changes in composition at and near boundaries and surfaces have been reviewed by Kingery[1,2]. Segregation at surfaces in single-crystal MgO of Fe, Cr and Sc, which were present in concentrations within the single-phase region, has been reported[3]. In a recent investigation using the dedicated scanning transmission electron microscope (STEM), Mizutani et al.[4] found increased concentrations of Sc, Ca and Si within 200Å of the boundary in MgO. Similar increases in Ca and Si concentration at the boundary had been observed by Kingery et al.[5]

In the present work we have used Auger electron spectroscopy (AES)* concurrently with inert ion sputtering to determine more precisely the concentration profile of segregants at the boundary in MgO containing 3000 cation ppm Sc and minor quantities of the impurities Ca and Si. The experimental observations are compared with the segregation expected from space charge theory for the trivalent Sc^{3+} in MgO.

II. Experimental Procedure

A polycrystalline MgO specimen doped with Sc was prepared and fractured in high vacuum for AES analysis. Initial AES spectra were taken on a grain boundary and then the site was sputter-profiled to observe changes in concentration adjacent to the boundary. This specimen

---

*The AES analysis was carried out in the Mechanical Engineering Laboratory of the University of Texas at Austin.

was prepared from powder produced by hydroxide coprecipitation using solutions of $Mg(NO_3)_2$ and $Sc(NO_3)_3$ and a continuous flow process which ensured uniform particle size and solute distribution. The Sc content was determined to be 3000 ± 300 cation ppm by atomic absorption analysis. The Ca and Si impurity levels were not analyzed; they are typically 100-200 ppm in such coprecipitated powders. The powder was isostatically pressed into a small rod (~2 mm diameter) and subsequently sintered in air at 1600°C for 6 hours followed by quenching, in order to attain a uniform solid solution. This specimen was then subjected to a second heat treatment at 1200°C for 165 hours to allow equilibrium segregation of solutes to the boundaries, following which it was rapidly cooled in air at a rate of ~10°C per second.

A Sc-doped single crystal calibration standard was prepared to evaluate the sputtering characteristics of Sc in the MgO matrix and to obtain the Auger sensitivities of these elements for quantitative interpretation of boundary segregation. The specimen was prepared by embedding a crystal (10 x 10 x 0.55 mm) of high-purity MgO* in a powder mixture made from 1 part pure MgO and 9 parts 99.9 (R.E.O.) Sc_2O_3. Isostatic pressing at 138 MPa ensured good contact between powder and crystal; ~~and~~ this assembly was then heat treated at 1760°C in air for 3 hours to diffuse in the desired quantity of Sc. The powder shell was removed and the crystal was homogenized at 1760°C in air for 215 hours. ~~In order~~ To confirm homogeneity of Sc in the standard, the crystal was subsequently

---

*Oak Ridge National Laboratory, Oak Ridge, Tennessee.

heat treated at 900°C for 165 hours to exsolve Sc_2O_3 second-phase precipitates which could be observed as a cloudiness in the crystal. The uniformity of precipitates was scrutinized with a scanning electron microscope by cleaving the crystal in a direction perpendicular to the faces and etching the cross-sections in 98% H_2SO_4 at 50°C for 2 minutes[6]. A segment (4 x 1.5 x 1 mm) of the crystal, thus carefully selected to have a uniform dispersion of Sc_2O_3 precipitates, was reheated at 1670°C in air for 13 hours in order to re-dissolve the Sc_2O_3 and used as the calibration standard. Accurate lattice parameter measurements were performed on the standard after it had been analyzed by AES, using a Debye-Scherrer technique[6], and the concentration of Sc was thereby determined to be 17,800 ± 1900 cation ppm Sc.

AES analysis was performed with standard equipment.* The specimen and the calibration standard were ultrasonically cleaned in methanol and baked in-situ in the evacuated AES chamber at ∿250°C for 6 hours prior to analysis. Both were fractured in high vacuum (less than 1.5×10^{-10} mPa) immediately prior to analysis in order to provide a clean surface, free from externally adsorbed impurities. The fracture face of the polycrystalline specimen is shown in Figure 1. The mode of fracture was [Fig. 1
approximately 50% transgranular and 50% intergranular. The grain size was in the range of 15 to 50 μm, and for AES analysis the flat, well exposed grain boundary that is indicated in Figure 1 was chosen. The AES electron beam was focused to a diameter of about 5 μm and centered

---

* Physical Electronics Industries, Inc., Model 590, Eden Prairie, Minnesota.

upon this site. The fracture face of the calibration crystal is not shown, but it was a planar (100) face. A standard pre-alignment method was used to place the AES beam coincident with the center of the much larger area (~1 mm) sputtered by the ion beam.

Data was taken both in the form of derivative spectra (dN(E)/dE) and as sputter-etch profiles showing the change in derivative peak heights, with sputtering time, of pre-selected peaks in the derivative spectrum. Atomic concentrations were evaluated from the derivative spectra through a simple analysis of relative peak heights[7]. For this analysis the relative sensitivities to AES of the elements Mg, O and Sc were obtained from spectra taken on the calibration standard in which the atomic concentrations were known. The relative sensitivities of Ca and Si were taken from published data[7].

In order to determine the sputtering rate of MgO for interpreting the depth of segregation, a polished single crystal of MgO equipped with a "knife edge" mask also of single-crystal MgO was sputtered for 30.0 hours under the same experimental conditions as the specimens. The ion beam incidence angle was the same for all sputtered surfaces, and in our results the rate is assumed to be independent of surface orientation. To obtain the rate, the step height between sputtered and masked portions was measured interferometrically.

III. Results and Discussion

Prior to sputtering, the spectra shown in Figure 2 were obtained. [Fig. 2
It is seen that the grain boundary contains Sc, Si, Ca and a small amount of C (adsorbed from the test atmosphere) in addition to the host

elements. The as-fractured calibration standard shows a small Sc signal in addition to the matrix Mg and O.

The sputter profile of the calibration standard is shown in Figure 3 as the variation in Sc/Mg peak height ratio with depth of penetration. It can be seen that the sputtering process induces little change in the relative AES signals. This indicates that at low concentrations of Sc in MgO neither preferential enrichment nor removal of Sc occurs to a substantial degree upon sputtering. Consequently, Sc concentration changes observed in the following sputter-profile may be considered real and not artifacts of the sputtering process. [Fig.

The sputter-profile of the grain boundary site is shown in Figure 4, where the change in the peak height ratios Si/Mg, Ca/Mg and Sc/Mg are monitored with depth of penetration. The Si and Ca signals decrease to background levels in less than 1.0 nm. These profiles are as expected for partial monolayer adsorption at the boundary and correspond closely to what has been observed in metals[8]. The Sc segregation profile, however, in which the width of segregation extends out to about 2.5 nm, clearly indicates a different type of behavior. [Fig. 4

Boundary segregation of solutes can result from strain effects[1,2,9]. When the solute atom differs in size from the solvent atom for which it substitutes, accommodation of the solute atom at boundaries or other lattice imperfections will result in a lowering of the expended strain energy as compared to accommodation in the bulk.

When considering aliovalent solutes in ionic solids, however, the driving force for segregation can also be the electrostatic potential present at the surfaces and grain boundaries[2]. Frenkel[10] and Lehovec[11]

showed that due to a difference in the formation energies of cation and anion vacancies, the boundaries of an ionic solid will carry an electric charge caused by the presence of excess ions of one sign. A compensating space charge of the opposite sign adjacent to the boundary would then be created. In simple ionic solids the energy needed to create a cation vacancy is generally assumed to be less than that for an anion vacancy, and thus for a completely pure material the expected boundary charge is positive and the space charge is negative. However, the presence of aliovalent solutes requires the formation of additional cation vacancies to maintain charge neutrality in the bulk, and when the number of added vacancies is sufficiently large compared to the thermally generated vacancies the respective signs of the boundary and space charge will change[1,10,11]. In MgO the energy for intrinsic vacancy formation is sufficiently large (Schottky energy about 1.12×10^{-18} J[12,13]) that even in so-called "pure" material the concentration of thermally generated vacancies is small compared to those generated by impurities, and extrinsic (i.e., solute-controlled) behavior is expected in all practical situations. Indeed, the boundary of MgO has been shown to carry a negative charge[1].

In the case of Sc^{3+} in the MgO lattice, strain effects are unlikely to be a major cause of segregation, as the ionic radius of Sc^{3+} (0.073 nm) is very close to that of Mg^{2+} (0.072 nm). We thus attribute the increased concentration of Sc adjacent to the boundary to a positive space charge balancing the negative boundary charge, where the segregating defect species is unassociated $Sc_{Mg}^{\bullet}$ with an effective +1 charge.

Integration of the observed profile of Sc (Figure 4) yields a value

of 8 x 10^{14} e cm^{-2}, where e is the electron charge, for the boundary charge necessary to balance the increased Sc'_{Mg} concentration on this side of the fracture path. As shown in Figure 5, the defect structure in the space charge region is dominated by the positive defect species, since negative defect species are repelled by the boundary and present in concentrations even less than the already low bulk values. [Fig.

Solutions of Poisson's equation for the space charge potential profile in ionic solids have been obtained by Lehovec[11] and Kliewer and Koehler[14], with equivalent results to those of Verwey and Overbeek[15] for electrolyte solutions. As detailed in Appendix A, we have calculated space charge segregation profiles of Sc consistent with the experimental value of the boundary charge. We have approximated the concentration of unassociated Sc in the bulk to be one-half the total Sc concentration, in accord with electrical conductivity data for Sc-doped single-crystal MgO[16]. Results are shown in Figure 6. Curve I is the solution known in colloid chemistry as the Gouy-Chapman approximation. A serious flaw of the theory is apparent; near-boundary concentrations of Sc are predicted that are much higher than the density of cation sites in the crystal. This results from the treatment of charge as continuous and the assumption that it is able to approach the boundary without limit, instead of considering the charge as made up of finite-size ions. Curve II shows a better approximation with the space charge region considered as two layers, a Stern layer and a Gouy layer. The Stern layer is an adsorbed layer of uniform charge concentration, across which the space charge potential decreases sufficiently for the Gouy-Chapman theory to be more applicable. In [Fig. 6

Figure 6 we have taken the Stern layer to be a partial monolayer and

have solved the Gouy layer to balance the fraction of the surface charge not compensated by the Stern layer. In addition, we have integrated the Gouy layer over successive atomic distances away from the boundary.

However, since in the experimental data the approach of ions to the boundary is apparently more constrained than is predicted by either continuum theory, it is perhaps appropriate to consider a multiple layer adsorption approach. In this analysis the free energy of adsorption can be considered to vary with the electrostatic potential. The electrostatic potential at each adsorbed layer beyond the first decreases as a function of the $Sc_{Mg}^{\cdot}$ concentration in previous layers, since they will partially compensate the boundary charge, and this situation may perhaps be likened to potential-dependent adsorption of ions at an electrode in an electrolyte solution. The result is depicted by curve III in Figure 6. As detailed in Appendix B, we have assumed Langmuir-type adsorption and have applied an expression developed by McLean[9] for adsorption at grain boundaries in metals in order to determine the Sc concentration of the adsorbed layers.

The multiple layer adsorption approach is apparently the better approximation of the observed segregation behavior, though it still represents a greatly oversimplified picture. We do not believe, however, that the data warrant a more complex analysis, as more precise spatial concentration data are necessary for comparison with theory. The optimum depth resolution of the AES analysis, limited primarily by the Auger electron escape depth, is only about 0.7 nm for the Sc peak monitored[17]. Aside from inherent limitations in the theories discussed, factors that

must be considered include the presence of other impurity cations, the equilibrium concentration of defect species, a certain migration of defects that may take place during cooling, and possible boundary orientation effects. However, despite these considerations, it seems that the segregation of Sc^{3+} to the boundary in the absence of a significant strain field is consistent with a space charge theory, and it is clearly a different type of behavior from that of partial monolayer adsorption.

Acknowledgements

This research was performed with the support of the U.S. Department of Energy under Contract No. EY-76-S-02-2390. Support for D. Finello by the Office of Naval Research under Contract N00014-78-C-0094 and support for Y.M. Chiang by the M.I.T. Undergraduate Research Opportunities Program is also acknowledged.

References

1. W.D. KINGERY, "Plausible Concepts Necessary and Sufficient for Interpretation of Ceramic Grain-Boundary Phenomena: I, Grain-Boundary Characteristics, Structure, and Electrostatic Potential," J. Am. Ceram. Soc. 57 [1] 1-8 (1974).
2. W.D. KINGERY, "Plausible Concepts Necessary and Sufficient for Interpretation of Ceramic Grain-Boundary Phenomena: II, Solute Segregation, Grain-Boundary Diffusion, and General Discussion," J. Am. Ceram. Soc. 57 [2] 74-83 (1974).
3. J.R.H. BLACK and W.D. KINGERY, "Segregation of Aliovalent Solutes Adjacent Surfaces in MgO," J. Am. Ceram. Soc. 62 [3-4] 176-178 (1979).
4. N. MIZUTANI, W.D. KINGERY and A.J. GARRETT-REED, to be published.
5. W.D. KINGERY, T. MITAMURA, J.B. VANDER SANDE and E.L. HALL, "Boundary Segregation of Ca, Fe, La and Si in MgO," J. Mat. Sci. 14, 1766-67 (1979).
6. A.F. HENRIKSEN and W.D. KINGERY, "The Solid Solubility of Sc_2O_3, Al_2O_3, Cr_2O_3, SiO_2 and ZrO_2 in MgO," Ceram. Int. 5 [1], 11-17 (1979).
7. L.E. DAVIS, N.C. MACDONALD, P.W. PALMBERG G.E. RIACH and R.E. WEBER, Handbook of Auger Electron Spectroscopy, 2nd edition. Physical Electronics Industries, Inc., Edina, Minn., 1976.
8. E.D. HONDROS and M.P. SEAH, "Segregation to Interfaces," Int. Met. Rev. 22, 262-301 (1977).
9. D. McLEAN, Grain Boundaries in Metals. Clarendon Press, Oxford, 1957.
10. J. FRENKEL, Kinetic Theory of Liquids, p. 37. Oxford University Press, New York, 1946.

11. K. LEHOVEC, "Space Charge Layer and Distribution of Lattice Defects at the Surface of Ionic Crystals," J. Chem. Phys. 21 [7] 1123-1128 (1953).

12. C.R.A. CATLOW, E.D. FAUX and M.J. NORGETT, "Shell and Breathing Shell Model Calculations for Defect Formation Energies and Volumes in Magnesium Oxide," J. Phys. C 9, 419-429 (1976).

13. W.H. GOURDIN and W.D. KINGERY, "The Defect Structure of MgO Containing Trivalent Cation Solutes: Shell Model Calculations," J. Mat. Sci. 14, 2053-2073 (1979).

14. K.L. KLIEWER and J.S. KOEHLER, "Space Charge in Ionic Crystals. I. General Approach with Application to NaCl," Phys. Rev. 140 [4A] 1226-1240 (1965).

15. E.J.W. VERWEY and J.Th.G. OVERBEEK, Theory of the Stability of Lyophobic Colloids. Elsevier Publishing Co., New York, 1948.

16. D.R. SEMPOLINSKI, W.D. KINGERY and H.L. TULLER, "Electronic Conductivity of Single Crystalline Magnesium Oxide," submitted for publication in J. Am. Ceram. Soc.

17. D.R. PENN, "Quantitative Chemical Analysis by ESCA," J. Elec. Spect. 9, 29-40 (1976).

Figure Captions

Figure 1. Fracture face of polycrystalline MgO specimen containing 3000 cation ppm Sc. The grain-boundary site of AES analysis is indicated by the arrow (450X).

Figure 2. AES spectra, taken before sputtering, of (a) the grain boundary in vacuum-fractured polycrystalline MgO containing 3000 ppm Sc and (b) the vacuum-fractured single-crystal MgO calibration standard containing 17,800 cation ppm Sc.

Figure 3. The ratio Sc/Mg in the sputter-profile of vacuum-fractured single-crystal MgO calibration standard containing 17,800 cation ppm Sc.

Figure 4. The ratios Sc/Mg, Si/Mg and Ca/Mg in sputter-profile of grain-boundary site in vacuum-fractured polycrystalline MgO containing 3000 cation ppm Sc.

Figure 5. Schematic representation of the concentration of (a) positive charged defect species and (b) negative charged defect species in the space charge region adjacent to the boundary.

Figure 6. The experimentally observed Sc segregation profile, the Sc segregation profiles calculated from the Gouy-Chapman and Stern solutions for the space charge potential, and the multiple-layer adsorption approximation, as described in the text.

Chiang, Henriksen, Kingery and Finello
Figure 1

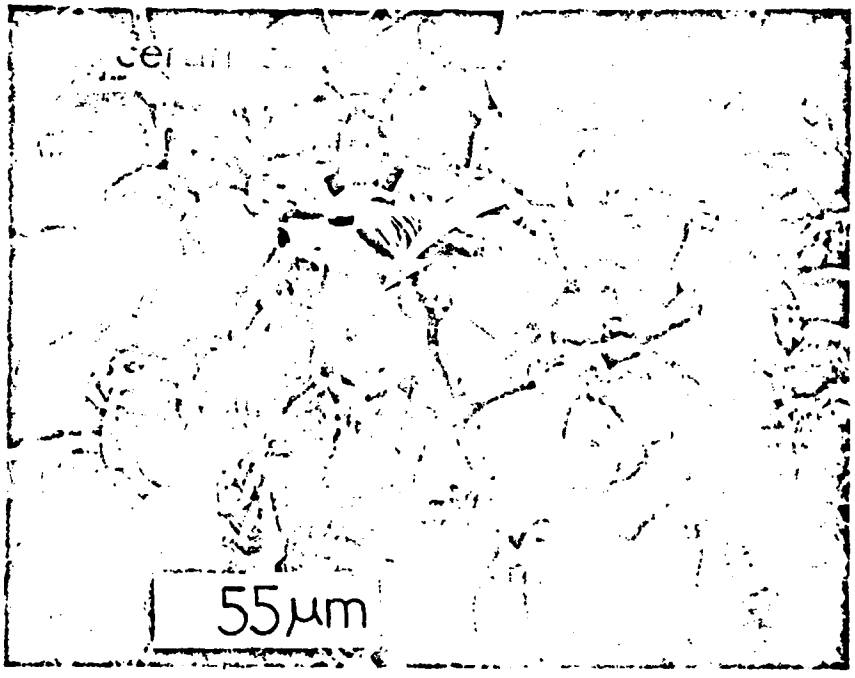

Figure 1. Fracture face of polycrystalline MgO specimen containing 3000 cation ppm Sc. The grain-boundary site of AES analysis is indicated by the arrow (450X).

Chiang, Henriksen, Kingery and Finello
Figure 2

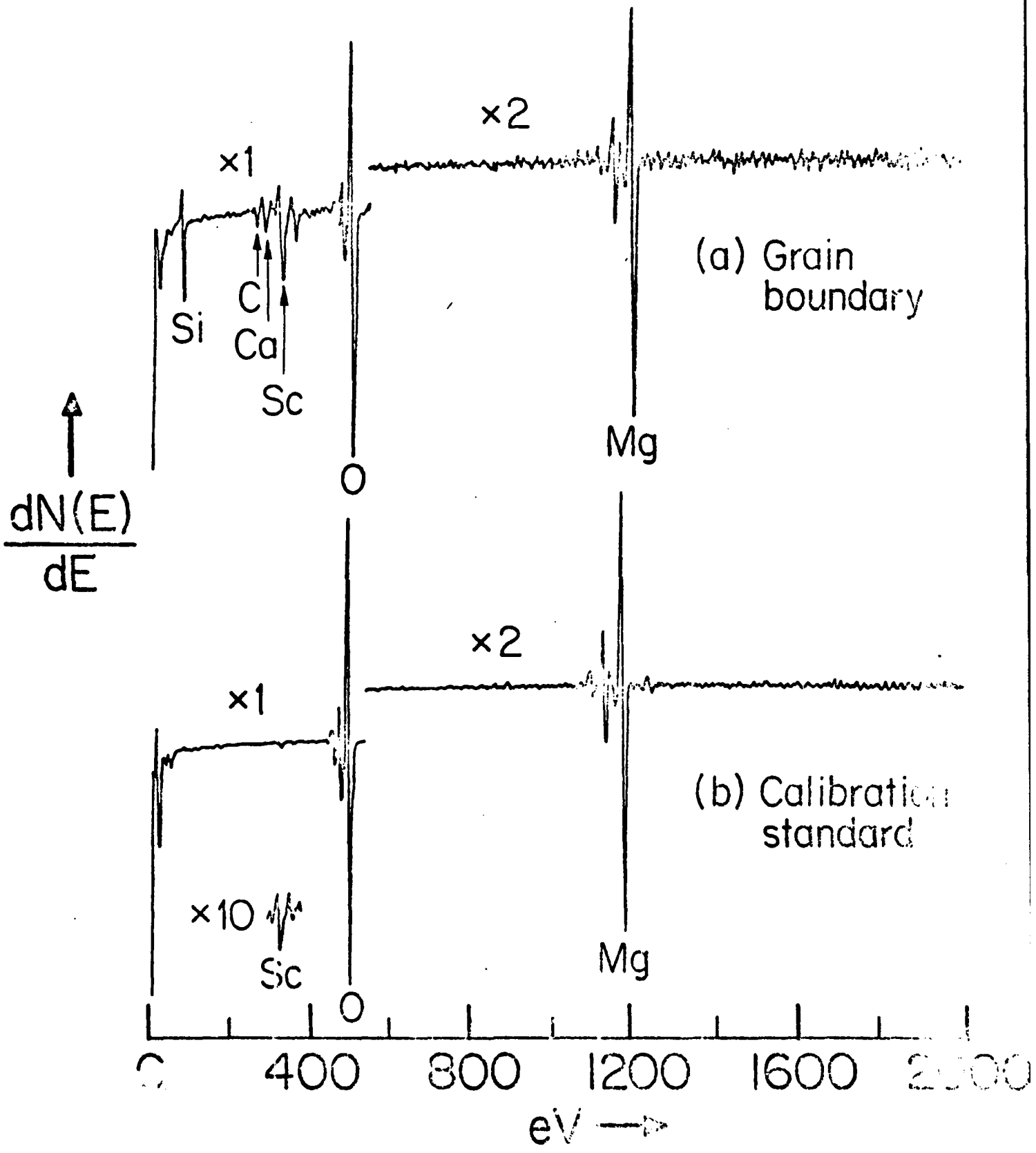

Figure 2. AES spectra, taken before sputtering, of (a) the grain boundary vacuum-fractured polycrystalline MgO containing 3000 ppm Sc and (b) the vacuum-fractured single-crystal MgO calibration standard containing 17,800 cation ppm Sc.

Chiang, Henriksen, Kingery and Finello
Figure 3

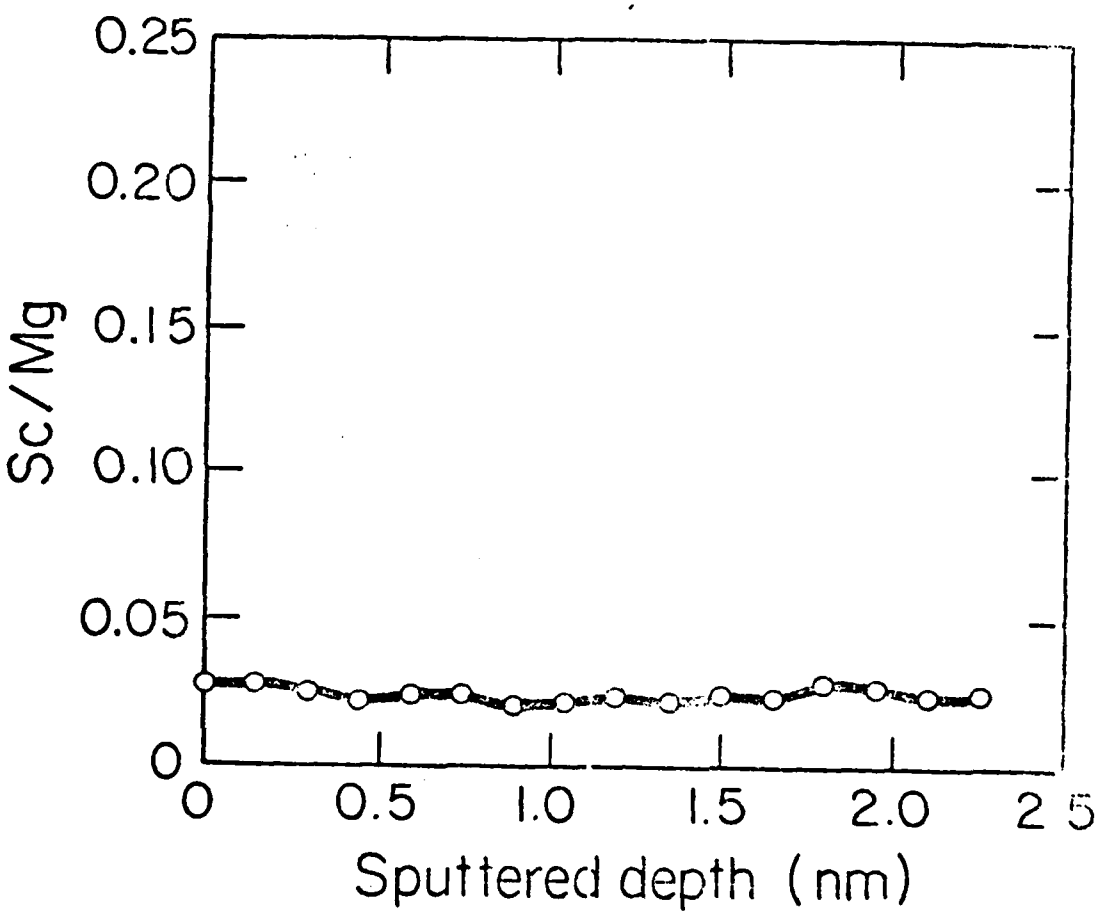

Figure 3. The ratio Sc/Mg in the sputter-profile of vacuum-fractured single-crystal MgO calibration standard containing 17,800 cat om ppm Sc.

Chiang, Henriksen, Kingery and Finello
Figure 4

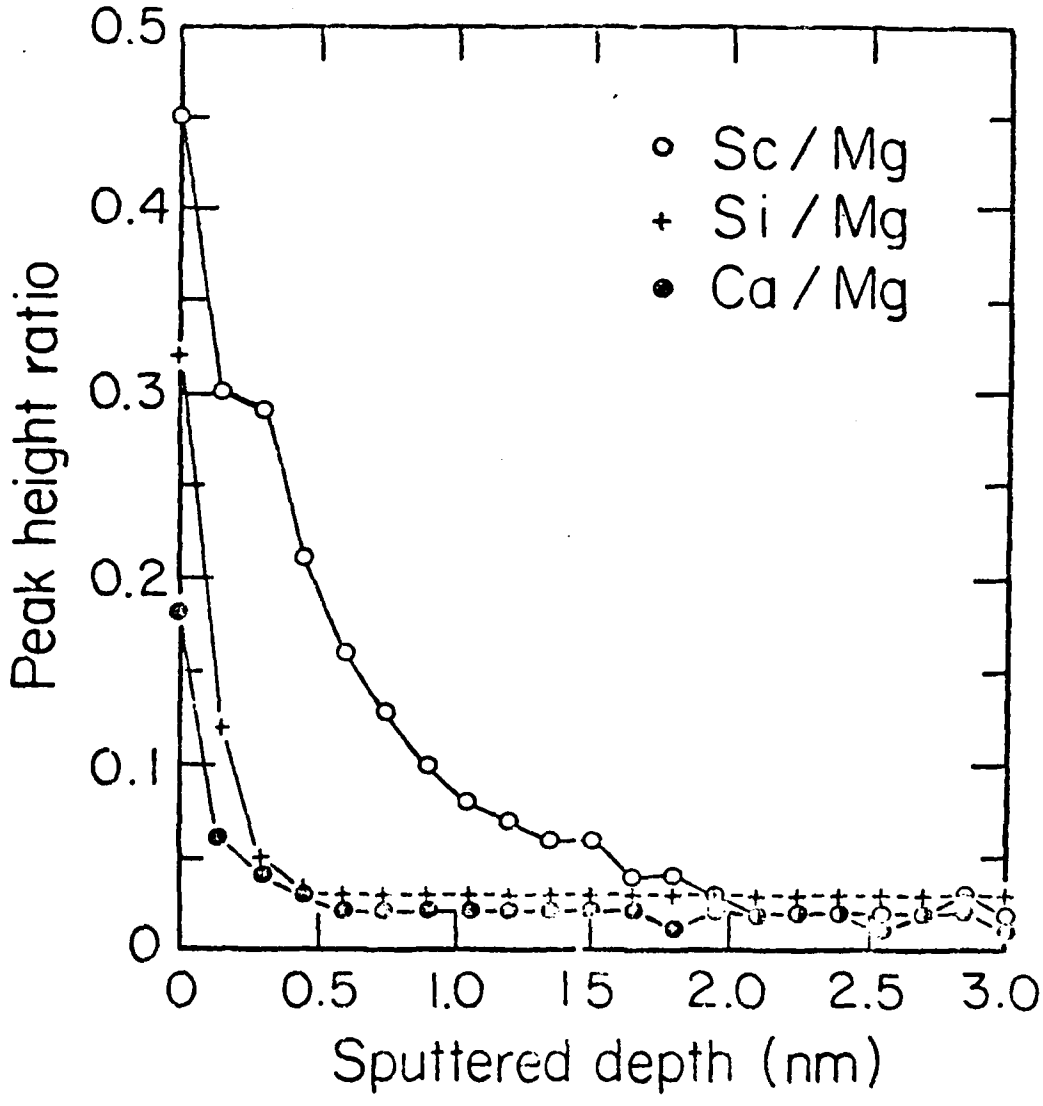

Figure 4. The ratios Sc/Mg, Si/Mg and Ca/Mg in sputter-profile of grain-boundary site in vacuum-fractured polycrystalline MgO containing 3000 cation ppm Sc.

Chiang, Henriksen, Kingery and Finello
Figure 5

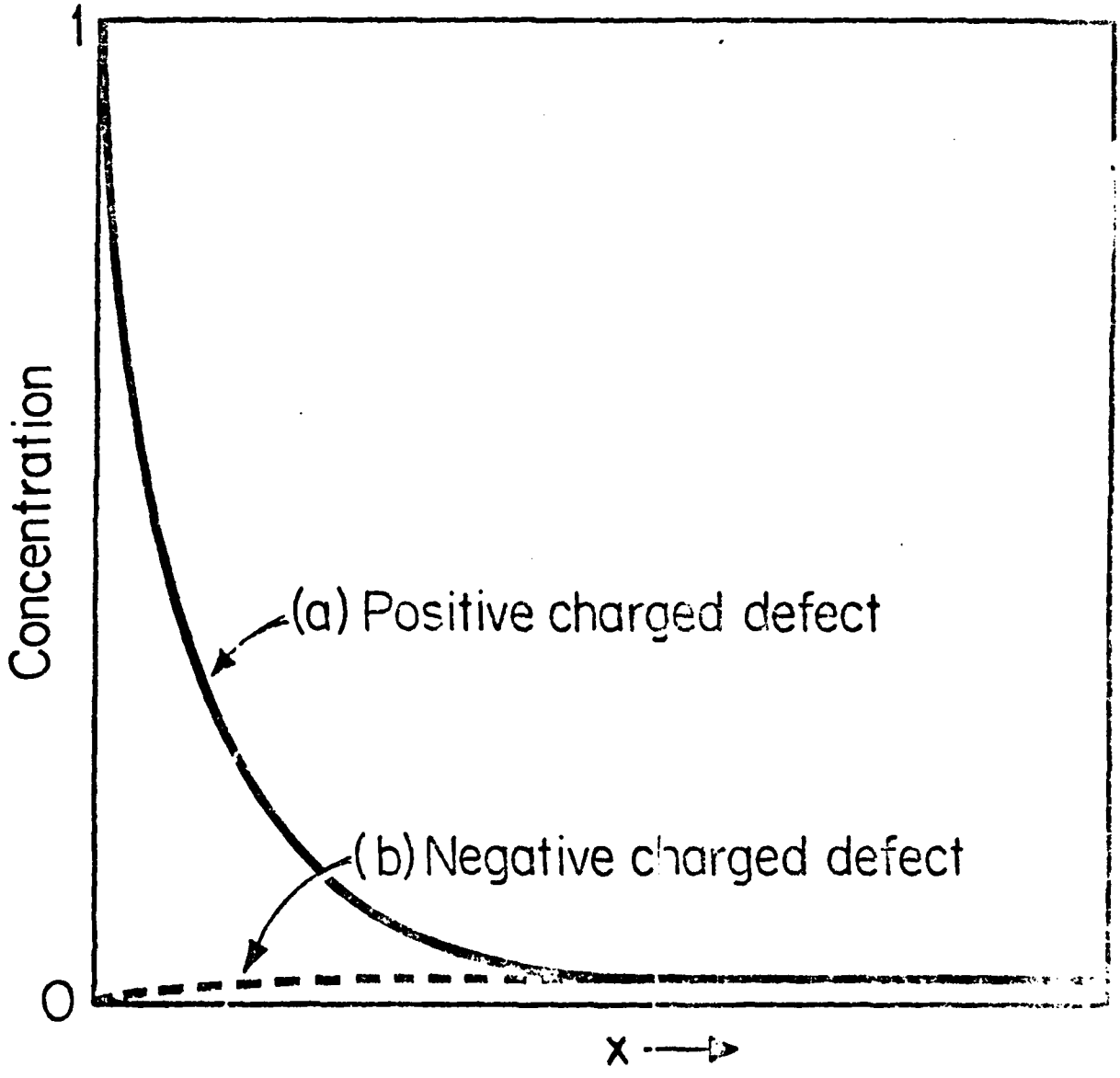

Figure 5. Schematic representation of the concentration of (a) positive charged defect species and (b) negative charged defect species in the space charge region adjacent the boundary.

Chiang, Lenriksen, Kingery and Finello
Figure 6

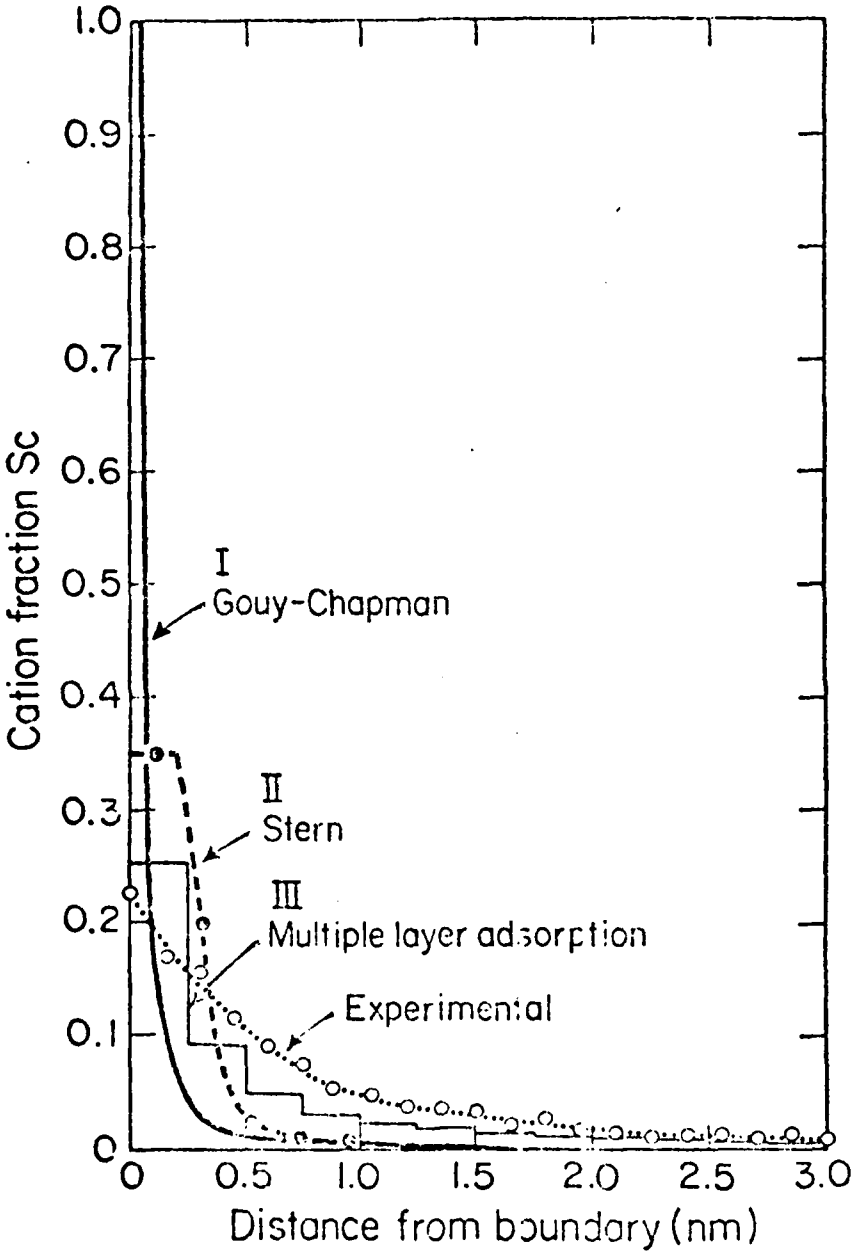

Figure 6. The experimentally observed Sc segregation profile, the Sc segregation profiles calculated from the Gouy-Chapman and Stern solutions for the space charge potential, and the multiple layer adsorption approximation, as described in the text.

Appendix A. Gouy-Chapman and Stern Solutions

The electrostatic potential ϕ is referenced as zero in the bulk of the material (i.e., at $x = \infty$). As discussed in the text, we assume that the concentration of unassociated Sc substituted for Mg, $[Sc_{Mg}^{\cdot}]$, is one-half the total bulk Sc concentration, and that the remaining defect structure is dominated by the Sc-Mg vacancy associate, $[(Sc_{Mg}-V_{Mg})']$, and we approximate the concentration of this species as the remaining one-half of the bulk Sc concentration. That is,

$$n_f^{\infty} = [Sc_{Mg}^{\cdot}]_{\infty} = n$$

$$n_d^{\infty} = [(Sc_{Mg}-V_{Mg})']_{\infty} = n$$

$$n = [Sc_{total}]_{\infty}/2 = 0.0015 \text{ cation fraction.}$$

Then, following Verwey and Overbeek[15], we first express the concentration of the defect species and the charge density $\rho(x)$ as

$$n_f(x) = n_f^{\infty} \exp[-e\phi/kT] = n \exp(-Z) \tag{1a}$$

$$n_d(x) = n_d^{\infty} \exp[+e\phi/kT] = n \exp(+Z) \tag{1b}$$

$$\rho(x) = e[n_f(x) - n_d(x)] = -2ne \sinh(Z)$$

where e is the elementary charge, k is Boltzmann's constant, T is the absolute temperature and $Z = e\phi/kT$.

From Poisson's equation in the one-dimensional case

$$\frac{d^2\phi}{dx^2} = -\frac{4\pi\rho}{\varepsilon} , \tag{2}$$

where the dielectric constant, ε, is herein assumed to be independent of position in the space charge region, we make the change of variables

$$\Lambda^2 = 8\pi ne^2/\varepsilon kT \quad \text{and} \quad s = \Lambda x ,$$

and obtain

$$\frac{d^2Z}{ds^2} = \sinh Z .$$

Integrating once, with the boundary conditions $Z = 0$ and $\frac{dZ}{ds} = 0$ at $s = \infty$, we have

$$\frac{dZ}{ds} = -2 \sinh(Z/2) . \tag{3}$$

Integrating twice, with the boundary conditions $\phi = \phi_o = \phi\big|_{x=0}$ and $Z = Z_o = e\phi_o/kT$ at $s = 0$ yields

$$e^{-Z} = \left[\frac{e^{Z_o/2} + 1 - (e^{Z_o/2} - 1)e^{-s}}{e^{Z_o/2} + 1 + (e^{Z_o/2} - 1)e^{-s}}\right]^2 . \tag{4}$$

Using the experimentally determined value of the boundary charge σ we can then solve for Z_o. Since the boundary charge balances the excess charge density in the crystal, we may express σ (using Eq. 2) as

$$\sigma = -\int_o^\infty \rho \, dx = \frac{\varepsilon}{4\pi}\int_o^\infty \frac{d^2\phi}{dx^2} \, dx$$

$$= -\frac{\varepsilon}{4\pi}\left(\frac{d\phi}{dx}\right)_{x=0} , \qquad \left(\text{since } \left(\frac{d\phi}{dx}\right)_{x=\infty} = 0\right)$$

Since $Z = e\phi/kT$, and using Eq. 3, we have

$$\left(\frac{d\phi}{dx}\right)_{x=0} = \frac{\Lambda kT}{e}\left(\frac{dZ}{ds}\right)_{x=0} = -\frac{2\Lambda kT}{e}\sinh\left(\frac{Z_o}{2}\right)$$

and

$$\sigma = \frac{\Lambda\epsilon kT}{4\pi e}\left(e^{Z_o/2} - e^{-Z_o/2}\right) \qquad (5)$$

with the result, at $\sigma = 7.76 \times 10^{14}\ cm^{-2}$ and $T = 1473°K$

$$e^{Z_o} = 1.34 \times 10^{-2}$$

$$\phi_o = -1.09\ V\ .$$

Using this result and eqs. 4 and 1, we obtain the Gouy-Chapman solution shown in figure 5.

The width of the space charge layer is approximated by

$$\Lambda^{-1} = \left(\frac{\epsilon kT}{8\pi ne^2}\right)^{1/2}\ .$$

Since the defect structure in the space charge region is dominated by the positive species, n is well approximated by the concentration of unassociated Fe_i and it is seen that the width of the segregated layer as calculated is relatively insensitive to reasonable variations in association behavior.

Appendix B. Multiple Layer Adsorption

It is assumed that the major driving force for segregation is the electrostatic potential; therefore the predominant change in free energy of segregation upon progressing from the first adsorbed layer to higher layers can be expressed as a change in the electrostatic potential energy, $e\phi$. Since the total charge concentration from all adsorbed layers must balance the boundary charge,

$$\sigma = \sigma_1 + \sigma_2 + \sigma_3 + \ldots,$$

the electrostatic potential of each layer can be obtained from the boundary charge still uncompensated at that layer, through Eq. 5 of Appendix A.

The expression for Langmuir-type adsorption at grain boundaries developed by McLean[9] for dilute solutions (or, equivalently, the "truncated" BET adsorption isotherm[8]) in which there is assumed to be a single layer, a single adsorbed species, no site-to-site interactions, and a fixed number of adsorption sites is:

$$\frac{x_b}{x_b^o - x_b} = \frac{x_c}{1 - x_c} \exp\left[\frac{E_a}{RT}\right]$$

where x_b is the concentration of occupied grain boundary sites, x_b^o is the saturation value of the same (here assumed equal to 1), x_c is the solute concentration in the bulk and E_a is the free energy of adsorption at the boundary. In this approximation we shall relax the single-layer constraint and assume no site-to-site interactions between as well as

within layer. A value for the adsorption free energy of the first layer, E_a^1, can be obtained by approximating the Sc'_{Mg} concentration of the first layer, x_b^1, from the experimental data. Then for each higher adsorbed layer i, the x_b^i value can be determined by decrementing the energy of the previous layer, E_a^{i-1}, by an amount equivalent to the drop in electrostatic potential between the two layers:

$$E_a^2 = E_a^1 - e\Delta\phi_{1,2}$$

$$E_a^3 = E_a^2 - e\Delta\phi_{2,3}$$

$$\vdots \qquad\qquad \vdots$$

$$E_a^i = E_a^{i-1} - e\Delta\phi_{i-1,i} \ .$$

The result is shown as curve III in Figure 6.

Appendix K

SCANNING ELECTRON MICROSCOPY/1981
SEM, Inc., AMF O'Hare (Chicago), IL 60666, USA

AUGER ELECTRON SPECTROSCOPY AS APPLIED TO THE STUDY OF THE FRACTURE BEHAVIOR OF MATERIALS

M. Schmerling, D. Finello and H.L. Marcus

Mechanical Engineering/Materials Science and Engineering
The University of Texas
Austin, Texas 78712

Abstract

Auger Electron Spectroscopy (AES) is used in a wide range of fracture problems. This paper describes fracture studies of iron, aluminum based alloys and metal matrix/ceramic composites. The paper also describes how AES analysis, when combined with the SEM, inert ion sputtering, SIMS, ESCA and other surface and near surface techniques, is used in determining the fracture behavior of materials previously subjected to various environments.

KEY WORDS: Auger Electron Spectroscopy, ESCA, Inert Ion Sputtering, Hydrogen Transport, SIMS, Fatigue, Embrittlement, Environmental Effects, Corrosion, Fracture.

Introduction

One of the earliest applications of Auger Electron Spectroscopy (AES) in materials research was the study of the grain boundary fracture of steels (1-4). Research in fracture still follows the basic experimental approaches defined then but the techniques have been refined. The major instrumental advance in AES has been the improved spatial resolution associated with the development of the scanning Auger microscope (4-5). The ability to get Auger data from areas less than the grain diameter in metals and ceramics allowed chemical analysis associated with the fracture process to be studied in detail. The transition from a research laboratory instrument to one used routinely in most laboratories which occurred in the last decade to the AES Microscope has allowed broadened applications to studies of fracture and failure in a wide variety of materials.

It is the purpose of this review paper to describe the recent AES research being performed to develop an understanding of the fracture behavior of structural materials. The paper will draw heavily from the research efforts of the authors during the last few years.

The results will be presented in two ways. The first will describe, in general, the usefulness of AES in clarifying fracture mechanisms. The second will indicate the experimental problems associated with interpreting the AES data. In addition data and results showing the advantage of combining AES with SIMS, SEM and ESCA will be presented.

Technic[illegible] Approaches

There are two types of fracture problems studied with AES. The first type is one in which a thin layer, several monolayers in extent, controls the fracture process. This includes a large class of problems related to grain boundary and interface segregation. In this case if the fracture surface is exposed to ambient conditions for as short a period as a few minutes (prior to being put into a hard vacuum), the oxide formed and other atmospheric contamination will complicate the gathering of meaningful AES results on the interface chemistry (1-3). For this reason the

experimental approach must include fracturing in situ in a hard vacuum or an inert gas environment. The hard vacuum is obtained by baking the system prior to fracture to reduce the residual concentration of water vapor which quickly contaminates fresh active metallic fracture surfaces such as for aluminum and iron alloys. The baking is not as essential for fracture studies of ceramics and semiconductor materials because they have relatively small sticking coefficients for oxygen.

The sample in the vacuum chamber can then be fractured under impact loading (2), torsion loading (3) or tensile loading (6). The sample can be fractured over a range of temperatures by using either a cooling or heating stage. High spatial resolution AES analysis of the surface is then performed (for a review of AES and other surface analysis techniques, see references 7 and 36). To enhance crack formation on the specific weak interface, fracture can be induced under either cyclic or sustained loading in a reactive environment such as hydrogen (8-10). This technique may allow the exposure of interfaces for AES analysis which would normally not fracture. Other techniques such as introducing embrittling elements by electrolytic charging followed by diffusion down the grain boundary have been tried with limited success. The objective is to diffuse sufficient embrittling elements such as S or As down the interface to induce interface failure. The hypothesis is that the original interface chemistry will not be modified and will be measured during the in situ fracture and AES analysis.

The second type of fracture problem is one in which the fracture is formed external to the system and AES analysis of the fracture surfaces is then obtained. In this case the important information may be hidden by an atmospheric contamination layer composed of oxides, hydroxides, and carbonaceous material. An example of the approaches used in these studies involves use of AES and ESCA to evaluate stress corrosion cracking (11). The oxide chemistry associated with the stress corrosion process gives clues to the origin of the fracture. Similar studies in progress are aimed at using AES and ESCA to distinguish between oxides such as Fe_2O_3 and Fe_3O_4 to help determine the origin of critical pre-existing flaws. In both these cases the oxides are very thick compared to the atmospheric contamination layers.

Another study of the second type involves the fracturing of a sample in an environment bearing an isotope of the element of interest. A combined AES and SIMS analysis to examine the environmental influence on fatigue crack growth using deuterium and O^{18} isotopes will be described later.

A vital aspect of the experiments is the combination of inert ion sputtering with the AES, SIMS and ESCA measurements. This allows the determination of not only the chemistry of the fracture interface but also the relative position of this interface to the rest of the structure of the material. An example of the applicability of this approach is in the interface fracture associated with metal-matrix composites. The fracture path is very sensitive to the existing layered structure associated with the composite. This will be discussed in more detail in the following section.

Fracture Studies

During the past 12 years AES has been used in many fracture studies. We will not attempt to delineate all of the studies but will focus on the recent work of the authors as being representative of some significant AES fracture studies.

AES Studies of Grain Boundary Embrittlement in Steels

Since early this century it has been observed that low alloy steels can become embrittled if they are kept in a well defined (~350 - 575°C) temperature range over extended periods of time. This "reversible temper embrittlement" consists of an increase in the ductile-to-brittle transition temperature for the steel; i.e., intergranularbrittle failures occur at temperatures where the steel is used rather than only at very cold temperatures. The effect can be reversed by short anneals above 600°C.

Typical compositions for these steels are 0.4 wt% C, 3.5% Ni, 1.7% Cr and $\leq$ 0.06% Sn, P or Sb (the balance being Fe). When embrittled alloys are fractured at room temperature, the fracture path is generally at prior austenite grain boundaries. This is also true for binary alloys of iron and some elements. Newly exposed grain boundary facets have been examined with AES after the specimens were fractured in a vacuum (2,3,7,12-19). Concentrations of the trace elements S, P, Sn, Sb, As, Te, Se, Pb at the grain boundaries, sometimes orders of magnitude higher than in the bulk, were measured at the boundaries in different alloys. Significantly higher grain boundary concentrations of Ni, Si, Cr and other alloying elements were also found in these alloy systems. In almost all cases inert ion sputtering showed the depth of the increased concentrations to be from ~.5 to 1 nm for the trace elements but apparently two to three times as great for the alloying elements such as Ni. Based on the AES and inert ion sputtering data several theories have been proposed to account for how a one or two monolayer region with high trace element concentration occurs and how one can account for microscopic fracture along it. One problem with the data is how to explain the observed differences in depth of the trace and alloying elements.

Plotting the concentration of Sn and Ni on a fractured grain (analyzing spot ~5000 nm) of an embrittled 3.5% Ni - 1.7% Cr - 0.4% C - 0.06 wt.% Sn steel versus sputter time, showed both elements having an approximately exponential decrease. The characteristic depth was two times as large for Ni as for Sn. To determine whether the observed profile represented an actual physical difference in thickness, Sn and Ni were deposited from a Sn wetted Ni filament inside the Auger system in a submonolayer film on top of a grain previously sputtered to the bulk concentration (20). Resputtering reproduced the same profiles observed on the original fractured specimen.

It thus appears that Ni is more strongly bonded to the predominantly Fe matrix than Sn, and Sn is preferentially sputtered leading to an apparent but artificial double thickness of the Ni enriched region at the grain boundary when compared to the Sn layer thickness, as illustrated in Figure 1. Preferential sputtering can lead to significant errors in modeling the diffusion and fracture process.

AES Studies of Metal Matrix Composites

Auger microscopy has become an essential tool in the study of ceramic fiber/metal-matrix composite materials. In a fiber composite the maximum mechanical properties can usually be obtained by having all the fibers aligned in a single direction in the matrix material. Unfortunately, in directions normal to this unique axis the material is often weaker than the homogeneous matrix material. This occurs because the interface region between the fiber and the matrix is generally weaker than either one and the fracture path includes the interface (21).

In studies of Ti-6Al-4V matrix with B_4C/B or SiC fibers, fiber composites in the form of consolidated wires with the fiber axis in the plane of the plate were fractured inside of the AES vacuum system. The fracture paths, Figure 2, contain a large amount of interface and followed the fiber sides of the interface through the carbides as determined from the characteristic carbon Auger derivative peaks. Careful peak shape studies can help determine which carbide, such as Ti or Si carbide in the SiC fiber composite, is prevalent. Sputtering profiles showed carbides and oxides near the SiC fibers, borides near the B_4C/B fibers, and S and Cl impurities at the interface. The brittle compounds associated with these elements and their poor bonding to the adjoining phases created a layer that resulted in the lowest energy fracture path (22).

When samples of the same Ti-6Al-4V material were thermally cycled between 550°C and 40°C in air for nine days the fracture path was partially through degraded interfaces filled with oxides. No significant amount of carbide was found in the fracture interface. This degradation of the interface reduced the longitudinal fracture strength (22).

Similar studies with aluminum matrix/graphite fiber composites have indicated oxides, carbides and TiB_2 present at the fracture interface. To identify from Auger data which compound is present in an unknown sample, the spectra from a standard sample observed under identical conditions should be compared to the unknown. Both peak-to-peak heights and peak shape must be correlated. If the unknown was sputtered, the same parameters must be used on the standard to avoid any preferential sputtering modifications. For example, a TiB_2 powder standard resulted in a direct correlation with the Auger data from the interface of the aluminum graphite composites.

An absolute check on compounds at the interface in graphite/Al fiber composites was made by correlating Auger results with TEM data. Interfaces were isolated either by dissolving the matrix (in HCl, HCl-methanol mixture, or KOH) or by electropolishing the matrix completely away

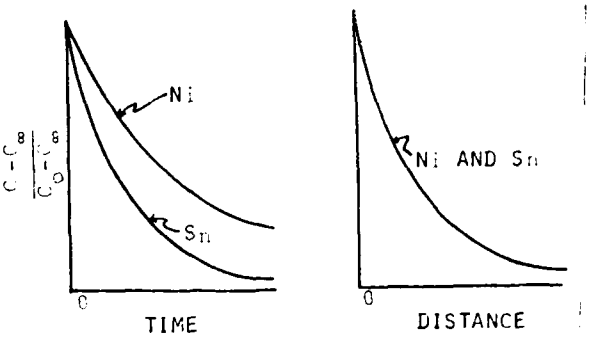

Figure 1. Schematic of normalized concentration of segregated Sn and Ni as detected by argon ion sputtering into an embrittled low alloy steel fracture surface. (a) Concentration vs. time indicating different sputter rates for Ni and Sn. (b) Concentration vs distance indicating that Ni and Sn have the same depth profile considering relative sputter rates.

Figure 2. (a) Fracture surface of Ti-6Al-4V/SiC composite showing path through interface.

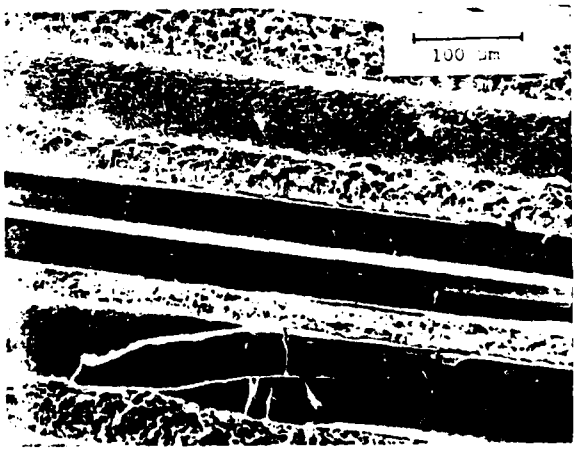

Figure 2. (b) Fracture surface of Ti-6Al-4V/B_4C/B composite.

M. Semmerling, D. Finello and H.L. Marcus

(in perchloric acid, ethanol and glacial acetic acid electrolyte). Small pieces of interface remained attached to the fibers and were observed in the TEM. Diffraction patterns confirmed the presence of TiB_2 as well as oxides of aluminum and other minor component elements of the matrix. Al_4C_3 and TiC were also detected from the diffraction patterns. The difficulty of indexing polycrystalline electron diffraction patterns was lessened considerably by having the Auger data on the thin interface material (23).

In order to examine the basic structure of the Al-graphite interface and factors that influence the interface strength, a model system was examined. Single crystal graphite flakes obtained from Ticonderoga granite were used. Since the basal plane of graphite is parallel to the plane of the flake, clean surfaces could be exposed by "peeling" off layers of graphite from the flake. In vacuums ranging from $4x10^{-7}$ torr to $2x10^{-3}$ torr aluminum was deposited on the clean flake from an Al coated hot filament. The resulting oxide layer at the graphite-aluminum interface ranged from ~3nm (determined by sputter profiling) for the high vacuum case to ~20 nm for the low vacuum. When segments of the aluminum were peeled away from the flake and both newly exposed surfaces examined with AES, it was apparent that the fracture traveled through the graphite for the thin oxides (a good interface bond) but went partly through the oxides and partly through the graphite for the thicker oxides (presumably a weaker bond). In addition to the AES peel studies, electrical I/V characteristics were measured and interpreted using the AES results. Figure 3 shows the experimental arrangement (23). The I/V curves show a high interface resistance when fracture occurs in the interface and low resistance when it occurs in the substrate as shown by AES.

AES of Fracture in Cast Iron

The morphology of the graphite particles in cast iron plays a major role in the fracture behavior of the iron (24). Ductile iron has spheroidized graphite particles. Fracture takes place along the graphite-metal interface. AES has been performed to attempt to identify why the interface was the preferred path. The chemistry of the interface was found to be the controlling factor in determining the morphology of the graphite, but the chemical composition apparently played no role in the fracture process. The fracture strength was controlled by the microstructure of the matrix (25-27). In this case the AES results did not lead to an improvement in fracture properties but were of value in determining the process by which the fracture controlling graphite morphology was determined. Figure 4 is an example of the fracture surface of ductile iron.

AES/SIMS Study of Fatigue Crack Growth in Aluminum Alloys

The influence of gaseous environments on fatigue crack growth in structural alloys has been extensively studied over the years (28-30). The AES/SIMS studies described here were aimed at looking at the transport of the embrittling species into the metal in the vicinity of the crack tip during the fatigue process. The study included gaseous H_2, D_2, D_2O, O_2, O_2^{18}, H_2O^{18}, N_2, Ar and hard vacuum as the environments for aluminum alloys fatigued in an environmental chamber. To separate the hydrogen and oxygen contamination, deuterium and oxygen-18 isotopes were used as the active environments. The samples were then examined in the AES/SIMS system with the normalized results shown in Figure 5. The O^{18} as determined with SIMS is much deeper into the surface than the unavoidable atmospheric oxygen as measured with AES and represents the oxide formed during fatigue. This oxide is thicker than one formed after fatiguing in vacuum. The deuterium is transported to a much greater depth (31-32) than the oxide. The shape of the deuterium profile can be explained as resulting from diffusion after the fatigue crack growth process is complete. This was confirmed with examination of ion implanted deuterium profiles as a function of time (32).

Electron and Ion Beam Damage Influence on AES Analysis on Fractured Carbon Composites

In an attempt to determine the local bonding in the carbon fiber-metal matrix composites, detailed AES fracture surface analyses were performed. This section will describe the problems associated with detailed Auger peak analysis using graphite as an example.

Surfaces which contain carbon in any of a variety of forms (i.e., hydrocarbons, functional oxycarbon groups and highly graphitic carbons) are highly susceptible to perturbations in physical structure under electron beam exposure. These changes in initial surface structure are directly associated with changes in the carbon Auger peak shape, as in the case of single crystal graphite (33). The changes undergone are permanent and may proceed through stages as the surface atoms approach a more disordered state. Electron-induced decomposition and selective desorption of other elemental species are likely to occur in weakly bound carbonaceous compounds, rendering surface analysis impractical via electron beam techniques.

In order to minimize surface damage caused by high energy electrons (~2-10 keV), x-ray photoelectron spectroscopy (XPS) is advantageous in surface analysis of graphite fibers, although the spatial resolution limitations of XPS make it unsuitable for many other applications in materials science (36). Likewise, ion-induced surface damage occurs upon inert ion sputtering of graphite fibers, resulting in further perturbations in the carbon Auger peak shape (see Figure 6). It is noteworthy that no electron-induced local changes in secondary electron yield are visible following argon sputtering of graphite fibers, whereas such changes are apparent prior to sputtering.

Characteristic loss spectroscopy (CLS) can be used to obtain matrix-sensitive information concerning a surface (37-40). This technique is considerably more delicate by virtue of the fact that it requires only a small fraction of the primary electron current density and voltage required with AES. The CLS process does not generate core holes; rather, it is intended to probe energy loss mechanisms experienced by backscattered electrons which have undergone

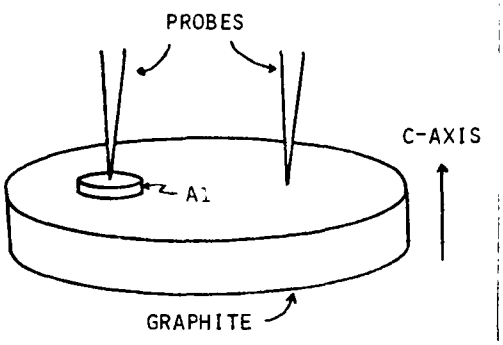

Figure 3. Geometry of Graphite/Al contacts for I/V measurements and peel tests.

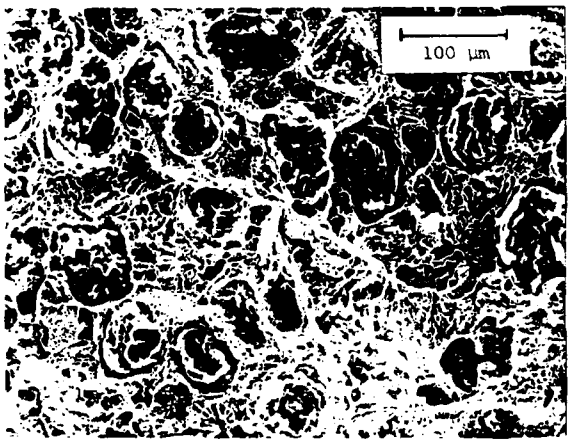

Figure 4. SEM of fracture surface of ductile iron.

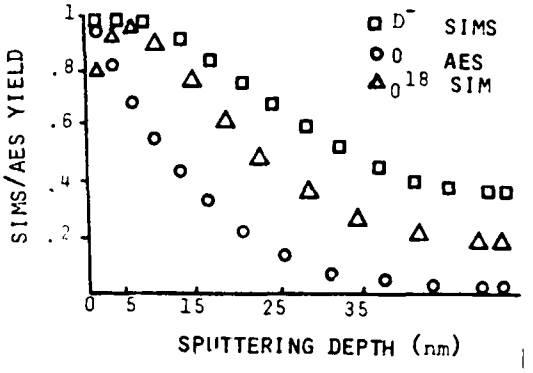

Figure 5. Sputter profile of deuterium and O^{18} as determined by SIMS and Oxygen as determined by AES.

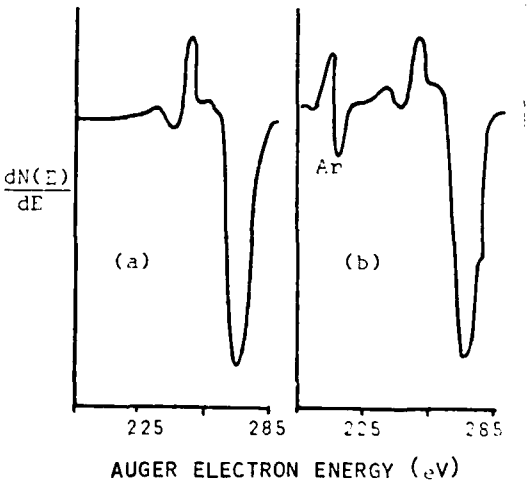

Figure 6. Carbon Auger features of highly graphitic VSO-054 fibers. (a) as received; (b) after sputtering.

interactions with the uppermost surface layers of the specimen matrix.

CLS is accomplished by using an electron energy analyzer to measure the energy distribution of electrons backscattered from a surface subjected to a monoenergetic primary beam of electrons. Typically, the primary electron beam energy is set below 2000 eV because most Auger peak energies of interest lie below this energy. Ideally, with the primary beam held at the energy of an Auger peak, the response function obtained through CLS serves as a description of the changes in energy which analyzed electrons have undergone due to kinetic events unrelated to bonding. The response function is valid over an energy range of several hundred electron volts, so a single Auger peak can theoretically be deconvoluted with the CLS spectrum of the same range of analyzed energies.

Before discussing deconvolution further, an illustration of CLS data for graphite fibers will be given. With an electron beam of only a few picoamperes rastered over an area of a few hundred thousand square microns, it is possible to delay the onset of surface damage for several minutes. (For comparison, beam currents greater by more than four orders of magnitude are required to obtain Auger data.) The CLS spectrum in the initial state is presented in Fig. 7(a), somewhat different from the final state displayed in Fig. 7(b). The difference is that the latter exhibits a small plasmon peak adjacent to the elastic backscatter peak, visible because the carbonyl and lactone oxygen surface groups (34, 35) have been decomposed by the electron beam. While performing AES on graphite fibers, the electron beam desorbs the weakly bound oxygen almost completely.

Traditionally, AES data handling has been facilitated by digital signal processing (41,42). Routine application of deconvolution techniques (43-47) would be impractical without on-line access to a high-speed computer. Raw AES data is initially taken in analog form. Accurate digitization of the signal is a necessity in order

to determine the existence of peak shifts and preserve peak shape. The digital energy increments should be discrete in terms of electron volts.

Superimposed upon the raw AES data is the large secondary electron background. It has been determined (48) that adjustment of an analytical function can simulate the background adequately over an energy range of a few hundred electron volts. Hence, the background can be synthesized and subtracted from an Auger peak. After subtracting the background from an Auger peak in derivative form, integration is performed in order to prepare the measured data for deconvolution.

Once the corresponding derivative CLS data is digitized and integrated, it is desired to deconvolute matrix and instrumental effects from the integral Auger data using the integral characteristic loss data as a response function. The iterative deconvolution scheme (49) is accurate provided that the data contains relatively little fine structure so that the algorithm leads to convergence. Figure 8 compared the original integral Auger data from pyrolytic graphite with a reconvolution of the final deconvoluted result to ensure that the two match one another. Due to electron-induced surface damage caused by the primary electron beam, the carbon Auger peak from any type of graphite will not reproducibly characterize the form of carbon as anything different from pyrolytic graphite. Even graphite single crystal basal plane surfaces do not regularly produce the sharp structural features in peak shape that have been reported (33).

Carbides, however, do not possess the graphitic resonant bond character, and will tend to retain their physical structure by resisting electron-induced surface damage somewhat. Well-resolved carbon Auger peaks for several general carbide standards which exhibit noticeable differences have been reported (33). Deconvoluted spectra of graphite and aluminum carbide are different (see Figure 9). The carbide peak has a sharper structure and this might be indicative of a more orderly surface structure.

The net result is that very little detailed information about the nature of the bonding at the fracture surface is obtainable with AES. In reality the fractured bonds have already undergone a major modification from the bonding in the original unfractured solid during the fracture process. The electron and ion beam damage makes it even more difficult to do any analysis.

It also should be noted that weakly bound elements such as Cl, Br, I etc. can easily be removed or greatly reduced in concentration by the electron beam before an AES analysis of the fracture surface is performed.

Summary

This review paper has tried to show, with a limited set of examples, how AES combined with other surface sensitive tools can be used in studies of the fracture of materials. The

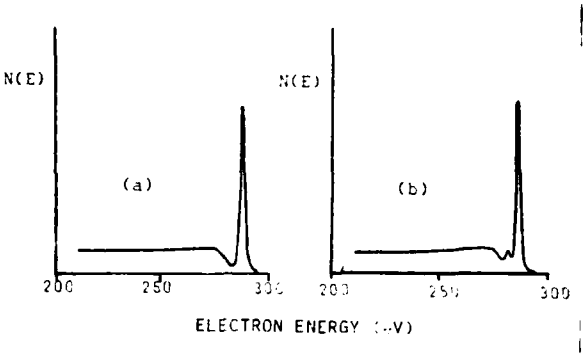

Figure 7. Integral characteristic loss spectra for high modulus pitch precursor type VSB-32 graphite fiber. (a) Prior to extensive electron beam damage to the surface. (b) After heavy damage to the surface. (Note: small plasmon peak.)

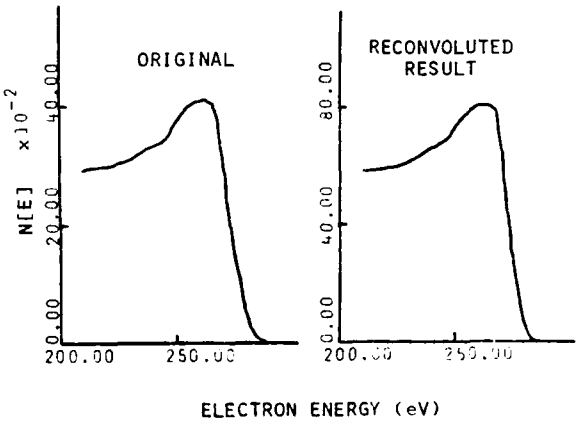

Figure 8. Original and reconvoluted Auger data from pyrolytic graphite.

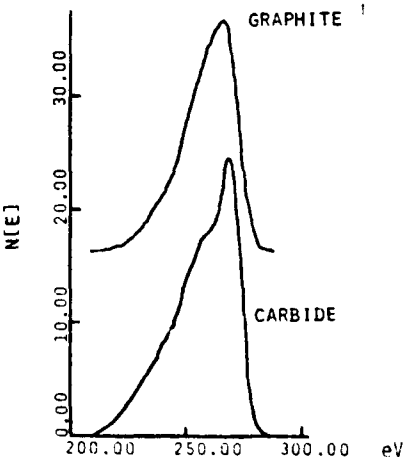

Figure 9. Deconvoluted integral Auger spectra of graphite and aluminum carbide.

applicability is widespread and routine in many laboratories. It was also pointed out that unless care is taken the observed data interpretation could have large errors. With care AES is a powerful tool for the study of fracture.

Acknowledgements

The authors acknowledge the support of this research by the Office of Naval Research, Contract N00014-78-C-0094. We appreciate the discussion with Dr. Swe-Den Tsai, Dr. Anna Zurek, Deepak Mahulikar and Young Park on their published and unpublished research.

References

1. Harris, L.A. "Analysis of Materials by Electron-Excited Auger Electrons" J.A.P. 39, (1968) p. 1419-1427.

2. Marcus, H.L. and Palmberg, P.W. "Auger Fracture Surface Analysis of a Temper Embrittled 3340 Steel" Trans AIME 245 (1969) pp. 1664-1666; "An Auger Spectroscopic Analysis of the Extent of Grain Boundary Segregation" ASM Trans Quart. 62 (1969) pp. 1016-1018.

3. Stein, D.F., Joshi, A. and LaForce, R.P. "Studies Utilizing Auger Electron Emission Spectroscopy on Temper Embrittlement in Low Alloy Steels" ASM Trans. Quart. 62 (1969) pp. 776-783.

4. MacDonald, N.C. "Auger Electron Spectroscopy for Scanning Electron Microscopy" in Scanning Electron Microscope Symp. 4th Proc., O. Johari, editor (1971) pp. 89-96.

5. MacDonald, N.C., Marcus, H.L. and Palmberg, P.W. "Microscopic Auger Electron Analysis of Fracture Surfaces" in Scanning Electron Microscope Symp. 3rd Proc., O. Johari, editor (1970) pp. 25-31.

6. Moorehead, R.D. "Mechanical Testing: in situ Fracture Device for Auger Electron Spectroscopy" Rev. Sci. Instrum. 47 (1976) pp. 455-459.

7. Marcus, H.L. "Surface Techniques for the Study of Materials: AES,ESCA, SIMS" J. Metals 29 (1977) pp. 20-24.

8. Briant, C.L. "The Effects of Sulfur and Phosphorous on the Intergranular Corrosion of 304 Stainless Steel" Corrosion 36 (1980) pp. 497-509.

9. Wei, R.P., Pao, P.S., Hart, R.G., Weir, T.W. and Simmons, G.W. "Fracture Mechanics and Surface Chemistry Studies of Fatigue Crack Growth in an Aluminum Alloy" Met. Trans. 11A (1980) pp. 151-158.

10. Wei, R.P. and Simmons, G.W. "A Technique for Determining the Elemental Composition of Fracture Surfaces Produced by Crack Growth in Hydrogen and in Water Vapor" Scripta Met. 10 (1976) pp. 153-157.

11. Joshi, A. Stress Corrosion Cracking, J. Yahalon and A. Aladjen, editors, Freund Publishing House, Tel Aviv (1978).

12. MacMahon, C.J., Jr. "Solute Segregation and Intergranular Fracture in Steels: A Status Report" Mat. Sci. & Eng. 42 (1980) pp. 215-226.

13. Lea, C., Seah, M.P. and Hondros, E. "The Intergranular Fragility Index - an Engineering Materials Parameter" Mat. Sci. & Eng. 42 (1980) pp. 233-244.

14. Dingley, D.J. and Biggin, S. "Grain Boundary Structure Intergranular Fracture and the Role of Segregants as Embrittling Agents" Phil. Trans. R. Soc. Lond. Series A 295 (1980) p. 165 (extended abstract).

15. Guttman, M. "The Role of Residuals and Alloying Elements in Temper Embrittlement" Phil. Trans. R. Soc. Lond. Series A 295 (1980) pp. 169-196.

16. Guttman, M. "Temper Embrittlement and Ternary Equilibrium Segregation" Mat. Sci. & Eng. 42 (1980) pp. 227-232.

17. Hirth, J.P. "Adsorption at Grain Boundaries and its Effect on Decohesion" Phil. Trans. R. Soc. Lond. Series A 295 (1980) pp. 139-149.

18. Jokl, M.L., Kameda, J., McMahon, C.J., Jr. and Vitek, V. "Solute Segregation and Intergranular Brittle Fracture in Steels" Met. Sci. (1980) pp. 375-384.

19. Stark, J.P. and Marcus, H.L. "The Influence of Segregation on Grain Boundary Cohesion" Met. Trans. 8A (1977) pp. 1423-1430.

20. Schmerling, M.A., Finello, D. and Marcus, H. L. "Anomalous Sputtering Effects in the AES Grain Boundary Analysis of Reversible Temper Embrittled Low Alloy Steels" Scripta Met 14 (1980) pp. 1135-1138.

21. Cornie, J.A. and Crossman, F.W. (Editors) Failure Modes in Composites, AIME-TMS, New York (1977).

22. Mahulikar, D.S., Park, Y.H. and Marcus, H.L. "Mixed Mode Crack Propagation in Continuous Fiber Metal Matrix Composites" in Proceedings of US-Greece Symposium on Mixed Mode Crack Propagation, G. Sih and P.S. Theocaris, editors (1980).

23. Tsai, S.D. "The Characterization of the Interface in Graphite-Aluminum Composite Systems" PhD Dissertation, The University of Texas, Austin December (1980).

24. Sourcebook on Ductile Iron, American Society for Metals, Metals Park, Ohio (1977).

25. Johnson, W.C. and Kovacs, B.V. "The Effect of Additives on the Eutectoid Transformation of Ductile Iron" Met. Trans 9A (1978) pp. 219-229.

26. Johnson, W.B. and Smith, H.B. "The Role of Interphase Boundary Adsorption in the Formation of Spheroidal Graphite in Cast Iron" Met. Trans. 8A (1977), pp. 553-565.

27. Smith, J., Brown, L. and Marcus, H.L. "The Influence of Microstructure on the Fracture of Ductile Iron" AFS Trans. (1980) pp. 427-436.

28. Louthan, M.R., Jr. and McNitt, R.P. (Editors) Environmental Degradation of Engineering Materials, Virginia Tech Printing, Blacksburg (1977).

29. Devereux, O.F., McEvily, A.J. and Staehle, R.W. (Editors) Corrosion Fatigue: Chemsitry, Mechanics and Microstructure, NACE-2, Houston (1972).

30. Meshii, M. (Editor) Fatigue and Microstructure, American Society for Metals, Metals Park, Ohio (1979).

31. Zurek, A.K., Marcus, H.L., Cecil, J.N. and Powers, R. "SIMS Study of Deuterium Trapping in Ion Implanted Aluminum Alloys" Met. Trans. 11A (1980), pp. 1920-1922.

32. Zurek, A.K. and Marcus, H.L. "Application of SIMS and AES to Environmental Studies of Fatigue Crack Growth in Aluminum Alloys" Proceedings of the SIMS-II Second International Conference on SIMS, San Francisco, August (1979), pp. 163-166.

33. Chang, C.C. "Analytical Auger Electron Spectroscopy" in Characterization of Solid Surfaces, P.F. Kane and G.B. Larabee, editors, Plenum Press, NY (1974) chapter 20, pp. 509-575.

34. Hopfgarten, F. "ESCA Studies of Carbon and Oxygen in Carbon Fibres" Fiber Sci. and Technol. 12 (1979), pp. 283-294.

35. Hopfgarten, F. "Surface Study of Carbon Fibres with ESCA and Auger Electron Spectroscopy" Fiber Sci. and Technol. 11 (1978) pp. 67-79.

36. Finello, D. and Marcus, H.L. "Advances in and Quantification of Auger Electron Spectroscopy" in Electron and Positron Spectroscopies in Materials Science and Engineering, O. Buck and H.L. Marcus, editors, Academic Press, NY (1979) pp. 121-181.

37. Knotek, M.L. and Houston, J.E. "Application of Auger and Characteristic Loss Spectroscopies to the Study of the Electronic Structure of Ti and TiO_2" Phys. Rev. B 15 (1977) pp. 4580-4586.

38. Rowe, J.E. "Covalent Bonding of Metal Atoms at the Schottky-barrier Interface of GaAs, Ge and Si" J. Vac. Sci. Technol. 13 (1976) pp. 798-801.

39. Sun, T.S., Chen, J.M., Viswanadham, R.K. and Green, J.A. "Plasmon-loss Satellites in Auger Spectra of Alloy Surfaces" Appl. Phys. Lett. 31 (1977) pp. 580-582.

40. Ritsko, J.J. and Rice, M.J. "Plasmon Spectra of Ferric-Chloride-Intercalated Graphite" Phys. Rev. Lett. 42 (1979) pp. 666-669.

41. Grant, J.T., Hooker, M.P. and Haas, T.W. "Use of Analog Integration in Dynamic Background Subtraction for Quantitative Auger Electron Spectroscopy Study of CO on Mo(110)" Surf. Sci. 46 (1974) pp. 672-675.

42. Grant, J.T., Hooker, M.P. and Haas, T.W. "Spectrum Subtraction Techniques in Auger Electron Spectroscopy" Surf. Sci. 51 (1975) pp. 318-322.

43. Houston, J.E. "Valence-band Structure in the Auger Spectrum of Aluminum" J. Vac. Sci. Technol. 12 (1975) pp. 255-259.

44. Smith, M.A. and Levenson, L.L. "Valence-band Information from the Auger KVV Spectrum of Graphite" Phys. Rev. B 16 (1977) pp. 2973-2977.

45. Tagle, J.A., Martinez-Saez, V., Rojo, J.M. and Salmeron, M. "Obtaining Density of States Information from Self-deconvolution of Auger Band-type Spectra" Surf. Sci. 77 (1978) pp. 77-93.

46. Powell, C.J. "Solid State and Atomic Features in the Valence-band Auger Spectra of Copper, Silver and Gold" Sol. State Comm. 26 (1978) pp. 557-562.

47. Hagstrum, H.D. and Becker, G.E. "The Interaction of Physics and Mathematics in Ion-Neutralization Spectroscopy" Phys. Rev. B 4 (1971) pp. 4187-4202.

48. Sickafus, E.N. "A Secondary Emission Analog for Improved Auger Spectroscopy with Retarding Potential Analyzers" Rev. Sci. Instrum. 42 (1971) pp. 933-941.

49. Madden, H.H. and Houston, J.E. "Correction of Distortions in Spectral Line Profiles: Applications to Electron Spectroscopies" J. Appl. Physics 47 (1976) pp. 3071-3082.

Discussion with Reviewers

G.B. Larrabee: Please comment on the role of ion scattering (ISS) and Rutherford backscattering (RBS) spectroscopy in characterizing fracture surfaces.
Authors: To the authors' knowledge, ISS and Rutherford backscattering have not been used extensively in characterizing fracture surfaces. In principal, ISS would give information about the fracture surface chemistry and Rutherford backscattering about the near surface chemistry.

G.B. Larrabee: Does surface roughness cause analytical problems in scanning Auger spectroscopy of microareas? How good is the quantitative analytical data that is generated?
Authors: It is obvious that surface roughness influences the Auger yield since the angle of incidence of the electron beam is spatially dependent. This would vary the contribution of the elements near the surface when compared to the contribution of the subsurface elements. In general that data is only semiquantitative in nature.

G.B. Larrabee: Imaging of fractured surfaces must be particularly difficult. Please comment on the best resolution and image quality that could be expected from a fractured surface of moderate roughness for SEM (secondary electrons detected), SAM (Auger electrons detected), EMP (x-rays detected) and SIMS (secondary ions detected).
Authors: The authors cannot give a limiting resolution on the fracture surfaces relative to the instrument resolution. In the case of SEM where resolution of about 5 nm is routinely obtained, this should be the resolution on a fracture plane normal to the electron optics. This will vary

geometrically for the other fracture surface orientations. Similar geometric effects can be expected in the SAM measurements, with submicron resolution readily obtained. The EMP will have the usual broadening associated with the depth of penetration and scattering of the primary electrons amplified by the orientation of the specimen. The resolution again is submicron in three dimensions. The SIMS results will depend on the beam size used, which in the newer machines is submicron. There may be an added contribution by double sputtering by the back-scattered ions and by shadowing due to the angle of incidence. This is also true for EMP and for SAM when the analyzer is not coaxial with the incident electron beam.

G.B. Larrabee: What is the role of in situ heating combined with Auger spectroscopy of a fractured surface to monitor out diffusion of species or the modification of the surface?
Authors: This approach has been tried by several investigators. There are potential differences between free surface segregation and grain boundary segregation due to the constraints at the grain boundary. For this reason direct comparison of free surface and grain boundary segregation must be carefully evaluated.

END

FILMED

6-83

DTIC